Recovery of Non-Aqueous Phase Liquids from Contaminated Soil by CO_2-Supersaturated Water Injection

by

Meichun Li

A thesis
presented to the University of Waterloo
in fulfillment of the
thesis requirement for the degree of
Master of Applied Science
in
Chemical Engineering

Waterloo, Ontario, Canada, 2009

I hereby declare that I am the sole author of this thesis. This is a true copy of the thesis, including any required final revisions, as accepted by my examiners.

I understand that my thesis may be made electronically available to the public.

Abstract

Supersaturated water injection (SWI) is a novel remediation technology which is able to remove entrapped residual NAPLs from saturated porous media by both volatilization (partitioning of volatile contaminants into the gas phase) and mobilization (displacement of isolated NAPL residuals by gas clusters). The character of gas saturation evolution in-situ in saturated porous media during SWI results in high sweep efficiency.

This work focuses on studying the recovery of entrapped residual NAPL by the mobilization mechanism during SWI, thus low-volatility NAPL residuals, kerosene and a kerosene-hexadecane mixture, are used as contaminants. A series of SWI recovery experiments are conducted to investigate the influence of grain size, low-permeability layering, and physical properties of the contaminants on the recovery behavior. For columns contaminated with kerosene, the residual saturation can be reduced to around 4% from an initial value of 16%, and over 70% of the residual kerosene is recovered by a combination of mobilization and volatilization in homogeneous sand packs. For columns contaminated with a kerosene-hexadecane mixture, the final residual saturation is 7.4% and the final NAPL recovery is lower than that in kerosene columns. Grain size has little influence on NAPL recovery, but low permeability layering has a significantly negative influence.

Experiments designed to compare SWI to sparging, and water-gas co-injection showed that water-gas co-injection was able to effectively recovery residual NAPLs albeit not as efficiently as SWI, while steady gas sparging is completely ineffective at recovering residual NAPL by mobilization. Based on these experimental observations, a conceptual model, involving double displacements and NAPL bank formation, is purposed to explain the experimental observations.

Acknowledgements

I am very much appreciative of the guidance, extensive advice, encouragement, and support from my supervisors, Dr. M. A. Ioannidis and Dr. I. Chatzis.

I am grateful for the support from the project partners, inVentures Technologies, Inc., and C3 Environmental Ltd., and from the Ontario Centres of Excellence.

I would like to thank co-op students, Robert Enouy and Taryn Adams for the help in their lab work.

I also appreciate the support from Ralph Dickhout, Ravindra Singh, Jeff Gostick, and Lesley James.

I wish to thank my friends and my colleagues in the Porous Media Laboratory for their help and encouragement.

Finally I would like to express my deep gratitude to my wife, Xin Zhang, and my son, Hanchen Li, for their support and understanding.

Table of Contents

List of Figures

List of Tables

Nomenclature

A	Sectional area of column
C_{CO_2}	Mole concentration of dissolved CO_2
C_s	Spreading coefficient
C_s^{eq}	Equilibrium spreading coefficient
g	Gravitational acceleration constant
h	Capillary rise
H	Henry's constant Hydraulic height
k	Absolute permeability
k_i	Effective permeability
k_r	Relative permeability
k_{rw}	Water relative permeability
k_{rn}	NAPL relative permeability
l	Length of NAPL cluster
L	Length of the porous medium pack
M_c	Final column weight
M_{CO_2}	Mole of CO_2
M_{ic}	Initial column weight
M_H	Mole of HCl
M_{OH}	Moles of –OH radical
N_{Bo}	Bond number
N_{Ca}	Capillary number
N_{CC}	Critical capillary number,
N_T	Total trapping number,
p_c	Capillary pressure
$p_{C,DD}$	Capillary pressure for double drainage
$p_{C,D}$	Capillary pressure for single drainage
p_g	Pressure in gas phase
p_i	Partial pressure of species i
p_i^o	Equilibrium vapor pressure of pure species i
p_n	Pressure in NAPL phase

p_w	Pressure in water phase
Q	Flow rate
Q_g	Gas flow rate
Q_w	Water flow rate
r	Radius of capillary tube
r_b	Radius of pore body
r_t	Radius of pore throat
R	Radius
S_g	Gas saturation
S_i	Saturation of i
S_{irn}	Initial residual NAPL saturation
S_n	NAPL saturation
S_{rn}	Residual NAPL saturation
S_w	Water saturation
t	Time
v	Velocity
v_w	Water velocity
$\vec{v}$	Velocity vector
V_{1dn}	Volume of NAPL displaced by 1st water flooding
V_{2dn}	Volume of NAPL displaced by 2nd water flooding
V_b	Bulk volume of porous media
V_{cn}	Cumulative volume of NAPL recovered.
V_{en}	Volume of NAPL emplaced
V_g	Volume of gas
V_{irn}	Volume of residual NAPL
V_n	Volume of NAPL
V_{np}	Volume of NAPL produced
V_p	Pore volume of porous media
V_w	Volume of water
V_{wp}	Volume of water produced
x_i	Mole fraction of i

α	Angle of the direction of flow from the horizontal plane
σ	Interfacial tension
σ_{sn}	Solid-NAPL interfacial tension
σ_{nw}	NAPL-water interfacial tension
σ_{sw}	Solid-water interfacial tension
θ	Contact angle
θ_r	Receding contact angle
θ_a	Advancing contact angle
θ_e	Equilibrium contact angle
θ_{nw}	Contact angle between solid and NAPL-water interface
θ_{ng}	Contact angle between solid and NAPL gas interface
θ_{gw}	Contact angle between solid and gas-water interface
σ_{gw}^{e}	Equilibrium interfacial tension between gas and water
σ_{nw}^{e}	Equilibrium interfacial tension between NAPL and water
σ_{gn}^{e}	Equilibrium interfacial tension between gas and NAPL
μ	Dynamic viscosity
μ_w	Dynamic viscosity of water
Φ	Porosity of porous media
ρ_g	Density of gas
ρ_n	Density of NAPL
ρ_w	Density of water
$\Delta\rho$	Density difference between the two immiscible fluids
Δp	Pressure gradient
∇p	Pressure gradient vector

Chapter 1

Introduction and Objective

1.1 Introduction

Groundwater, the largest source of fresh water reservoir available to humanity, is the water which saturates in the pores of soil, sediment, and narrow fractures in bedrock. Throughout ages, groundwater has been a major source of water supply for public, private, agricultural，and industrial uses. According to statistics for 1996, 30.3% of Canadian population, or 8.9 million people, depend on groundwater for their domestic use (Library of Parliament, 2006). In some provinces, groundwater is the primary source for their water supply system (Environment Canada website). Unfortunately, during the previous century, groundwater has been increasingly polluted by many contaminants, the physicochemical, biological, and radiological, nature of which poses a risk to human health. Among the contaminants, non-aqueous phase liquids (NAPLs) have been detected in numeral waste sites (Mercer et al, 1990) and considered as a major source of groundwater contamination. Most of the NAPLs cannot be broken down by natural processes. A lot of components are still considered toxic even at concentrations very much lower than their equilibrium concentrations, and despite the fact that their aqueous solubilities are very low (on the order of several hundred parts per million). NAPLs are considered the most persistent contamination sources to soil and groundwater due to their low solubilities. Because of the adverse effect of worldwide groundwater pollution by NAPLs on the environment and human health, it has been the focus of attention for the past several decades (Adamski et al., 2005). Remediation of sites contaminated by NAPLs has prompted extensive studies and development of technologies

aimed at addressing the scientific and engineering challenge associated with the removal of NAPL from soil. Much progress has been made; however great efforts are still needed to restore the NAPL contaminated sites quickly, effectively, and economically.

1.2 Project Objectives

Supersaturated Water Injection (SWI) is a patented technology (United States Patent 7300227) to recover NAPLs from the contamination source zone in the subsurface. In the study conducted by Li (2004), the ability of SWI to recover NAPLs by volatilization has been demonstrated in the column experiments. NAPL recovery by mobilization was unexpectedly observed and subsequently confirmed by a micro-model experiment. The main objective of present work is to study the performance and the mechanisms of residual NAPL removal by mobilization during SWI operation. Two non-volatile NAPLs, kerosene and a kerosene-hexadecane mixture, were used as contaminants in the experiments. A series of column experiments were conducted to examine the effect of low permeability layering, grain size, and type of contaminants on the recovery of NAPLs by SWI operations. Intermittent gas sparging and water-gas co-injection experiments were conducted to gain insight in the possible mechanisms of NAPL recovery by mobilization. SWI column experiments in absence of NAPLs were also conducted to understand gas saturation development and provide experimental data for the verification of simulation software.

Chapter 2

Background and Literature Review

2.1 Introduction to NAPL

2.1.1 LNAPL and DNAPL

NAPLs are typically immiscible with groundwater, and exist in subsurface as a separate phase. Based on their density, NAPLs may be classified into two categories: light non-aqueous phase liquids (LNAPLs), such as petroleum hydrocarbons, light aromatic compounds, which are lighter than water; and dense non-aqueous phase liquids (DNAPLs), for example, organic halogenated solvents, which are denser than water (Newell et al., 1995).

2.1.2 Migration and Partitioning of NAPLs in Subsurface

The contamination of soil and ground water by NAPLs is usually caused by occasional releases of NAPLs into the subsurface through spills, improper disposal, and leaking storage tanks etc. In subsurface soil matrices, the NAPLs move both vertically and laterally. Partitioning between the phases (gaseous phase, aqueous phase, liquid phase and solid phase) also takes place. These processes are very complex and affected by many factors, such as the physical and chemical properties of NAPLs (composition, density, interfacial tension, solubility, volatility, vapor density, partitioning properties and residual saturation), properties of the porous medium (permeability, wettability, pore size and structure), and content and velocity of groundwater.

Once released into environment, NAPLs enter the unsaturated zone (vadose zone), and move downwards under the combined action of gravitational and capillary forces, leaving residual globules trapped in the pores of soil and NAPL vapor in vadose zone. Lateral migration may occur because of the heterogeneity of the soil matrices. If the released volume is small, the NAPLs will be completely retained in the vadose zone. If the released amount is large enough, the NAPLs will continue to move downward until they encounter water table.

The migration of LNAPLs is schematically described in Figure 2.1(Kim et al., 2003). Because of their lower densities, the LNAPLs will pool on top of the water table as free-phase NAPL. The free-phase LNAPL will migrate laterally due to the pressure gradient caused by the hydrostatic pressure of the accumulation. Also groundwater flowing through the pooled LNAPL will cause lateral migration along the direction of groundwater flow.

Vertical movement of LNAPLs is usually caused by the fluctuation of water table. As the water table changes, the LNAPLs on the water table will accordingly move up and down, undergoing consecutive imbibition and drainage processes and forming a “smear zone” containing NAPL blobs or ganglia due to trapping by capillary forces (Reddi et al., 1998). In this “smear zone”, the residual LNAPLs will be slowly dissolved into groundwater to create a plume of contaminant, and evaporate into unsaturated soil to produce a vapor plume.

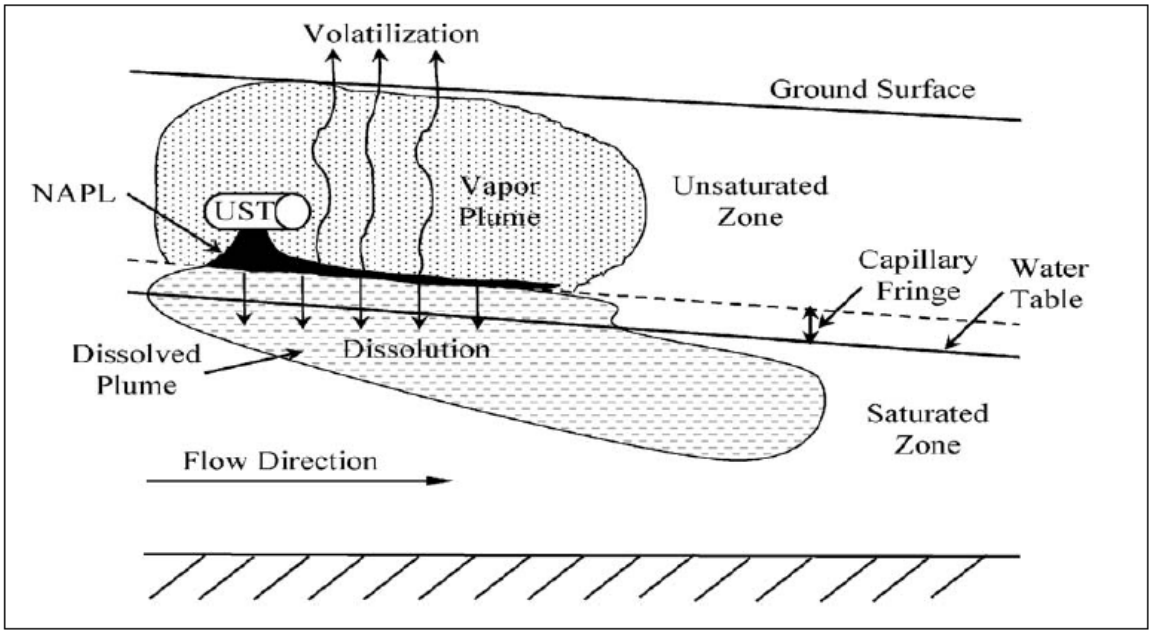

Figure 2. 1 Conceptual model of LNAPL migration in subsurface (Kim, et al., 2003)

Figure 2.2 (Kent et al, 2001) depicts the migration of DNAPLs in the saturated zone. Unlike LNAPLs pooling on top of the water table, DNAPLs will continue to travel downwards into the saturated zone due to their higher densities. In the saturated zone, the DNAPLs will move along pathways of maximum permeability until they are completely retained in the space of the porous media as discontinuous ganglia or droplets under the action of capillary forces, or accumulate on the low permeability layers or lenses, where they begin to migrate laterally, forming residual saturations and high saturation pools (Huling et al., 1991; Suchumel et al., 2006). As a result, the DNAPLs generally produce source zones that contain narrow vertical pathways connected by thin, laterally extensive horizontal layers. The DNAPLs in the saturated zone will be also slowly dissolved in water and create a plume of dissolved contaminant.

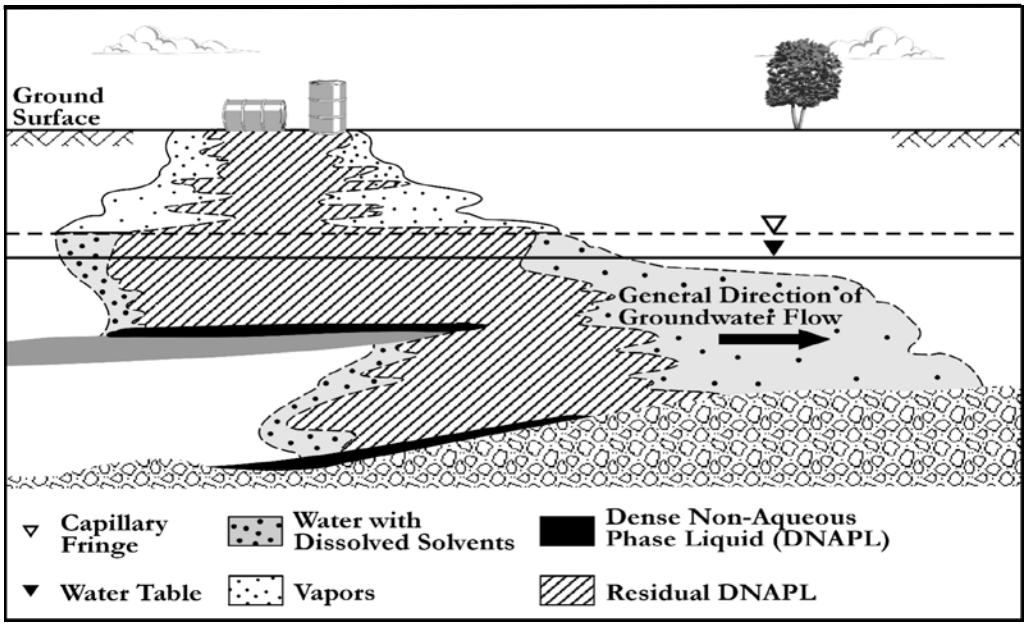

Figure 2. 2 Conceptual model of DNAPL migration in subsurface (Kent et al., 2001)

In a subsurface environment, NAPLs may exist in the following four phases (Konečný et al., 2003): air phase (vapor in soil gas), aqueous phase (NAPLs dissolved in water), immiscible oil phases (mobile NAPL), and adsorbed phase (NAPL adsorbed in the solid). Thermodynamics dictate the tendency for equilibrium partitioning of the contaminant among the different phases as shown in Figure 2.3.

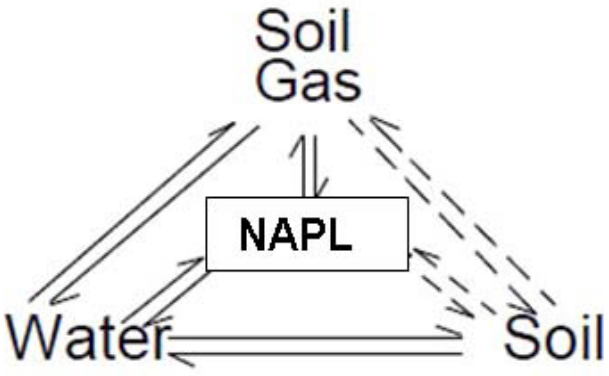

Figure 2. 3 Partitioning of NAPL among the four phases (after Newell et al., 1995)

2.2 Interfacial Phenomena in Porous Media

2.2.1 Wettability and Contact Angle

When a system contains more than one immiscible fluid, the term of wettability can be used to describe the preference of the solid surface for one of the liquids. Wettability depends on interfacial tensions, the unbalanced forces across an interface due to solid-liquid adhesion and fluid-fluid cohesion when a liquid is in contact with another substance (solid, or another immiscible liquid). The interfacial tension is defined as the amount of energy that is required to create a unit area of surface. Figure 2.4 shows a system with a solid surface (s) and two immiscible liquids (water and NAPL), where a drop of water (w) rests on a solid surface surrounded by NAPL (n).

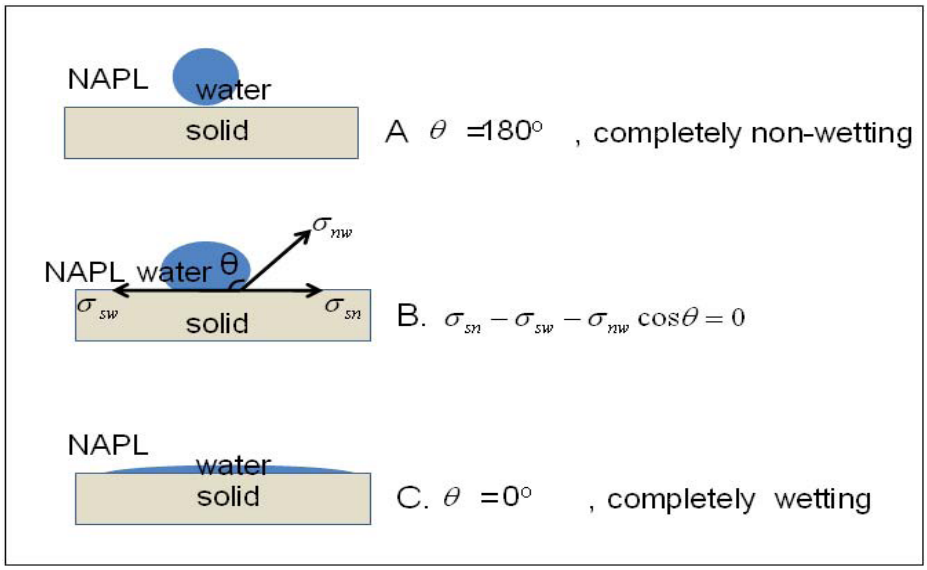

Figure 2. 4 Contact angle of a water-drop on a horizontal solid surface

At thermodynamic equilibrium, the relationship between the contact angle and the interfacial tensions at three-phase contact line can be expressed by Young's equation (Gary, 2008):

$\sigma_{sn} - \sigma_{sw} - \sigma_{nw}\cos\theta = 0$ ----------Equation 2.1

where σ_{sn}, σ_{sw}, and σ_{nw} are the interfacial tensions of solid-NAPL, solid-water, and NAPL-water, respectively, and θ is the contact angle, the angle between σ_{sw} and σ_{nw}. Contact angle can be used as a measure of wettability of the system. Theoretically the contact angles vary from 0^o to 180^o. When θ=0° or θ= 180°, the system is completely water-wet or NAPL-wet respectively. If $\theta \le 70^o$, the system is water-wet; if $\theta \ge 110^o$, it is NAPL-wet; and if θ is between 70^o and 110^o it is considered neutral wet (Mercer et al., 1990).

Two types of contact angle hysteresis occur in porous media. One is the static contact angle hysteresis in the absence of contact line motion. Figure 2.5 (Li, 2008) depicts hysteresis caused by tilting a solid surface. The other one is dynamic contact angle hysteresis associated with the movement of the contact line during immiscible displacement of two fluids, as shown in Figure 2.6. A receding contact angle θ_r is smaller than the equilibrium contact angle θ_e, and an advancing contact angle θ_a is greater than θ_e:

$\theta_a > \theta_e > \theta_r$ ----------equation 2.2

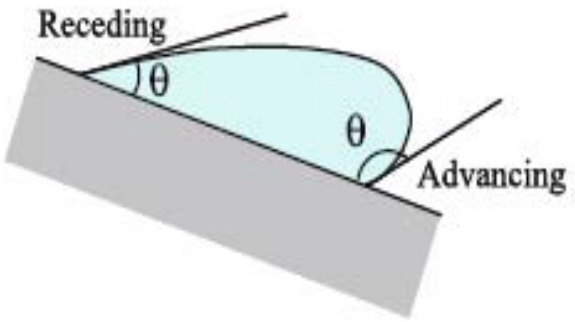

Figure 2. 5 Static contact angle hysteresis by tilting (Li, 2008)

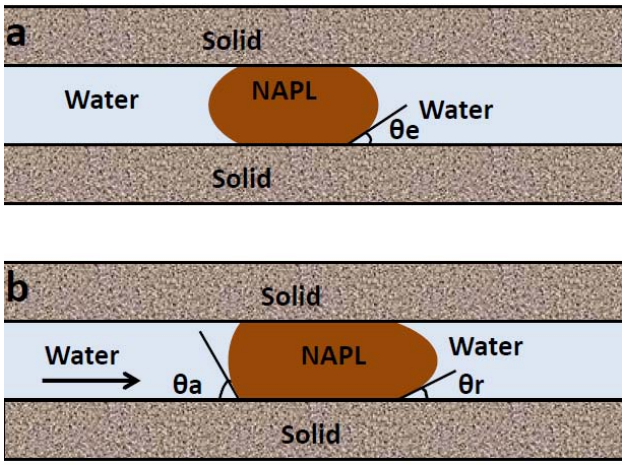

Figure 2. 6 Dynamic contact angle hysteresis in capillary tubes

Wettability is an important factor that impacts displacement mechanisms in porous media and the contaminant formation of residual NAPL (Al-Raoush, 2009, Harrold et al., 2001; Dwarakanath et al., 2002; Jackson et al., 2003). Wetting phase liquids preferentially wet the solid surface forming stable wetting films. Thus, the residual non-wetting phase always occupies the bigger pore bodies, whereas non-wetting phase occupies the smaller pore bodies and pore throats, or spreads over the solid surface in the form of films in saturated porous media. Figure 2.7 (Sahloul et al., 2002) is a schematic description of NAPL residuals in water-wet and NAPL-wet porous media.

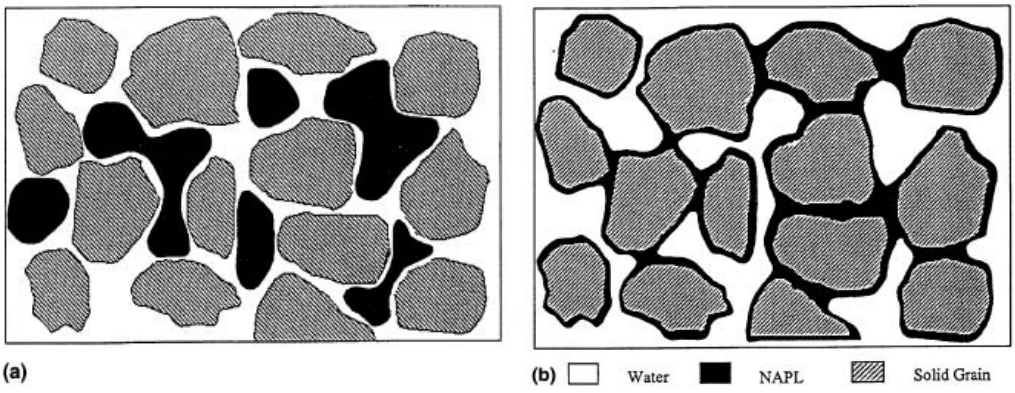

Figure 2. 7 Configurations of residual NAPL in water-wet (a) and NAPL-wet (b) porous media (Sahloul et al., 2002)

2.2.2 Spreading of NAPL in Porous Media

When LNAPL is present on a water-gas interface, the spreading tendency of the LNAPL across the gas-water interface can be measured by the spreading coefficient:

$$C_s = \sigma_{gw} - (\sigma_{nw} + \sigma_{ng}) \quad \text{----------Equation 2.3}$$

where σ_{gw}, σ_{nw} and σ_{ng} are interfacial tensions of the gas-water, NAPL-water, and NAPL-gas respectively, measured on pure fluids before they are brought into contact with each other (Zhou et al., 1996). In a water-wet medium, if the value of the spreading coefficient is non-negative ($C_s \geq 0$), the NAPL is able to spread over the water-gas interface and coat the interface with a molecular film (Keller et al., 1997), as shown in Figure 2.8 (b). In the presence of gas, the residual NAPL blobs are connected by these films, thus favoring the hydraulic continuity of the NAPL. If the system is characterized by a negative value of spreading coefficient ($C_s < 0$), the NAPL does not spread over the water-gas interface, but rests on the top of the water in the form of lenses, as shown in Figure 2.8 (a).

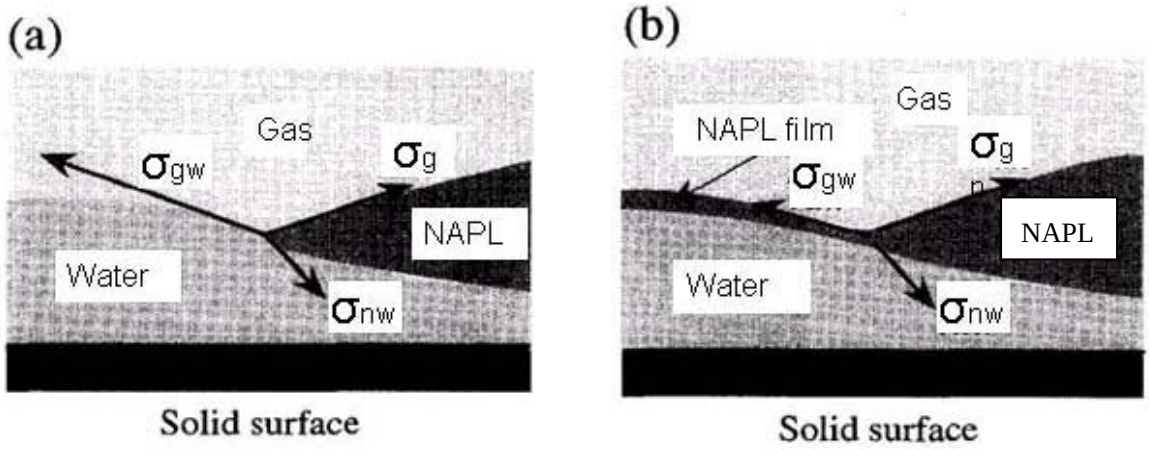

Figure 2. 8 NAPL on water- gas interface when $C_s < 0$ (a), and $C_s \geq 0$ (b) (after Zhou et al., 1996)

Usually, the interfacial tensions can change during the course of equilibrium partitioning of NAPL among the various phases present. We refer to these interfacial tensions as effective interfacial tensions. Letting σ_{gw}^{e}, σ_{nw}^{e} and σ_{gn}^{e} be the effective interfacial tensions of gas-water, NAPL-water, and NAPL-gas respectively, the equilibrium spreading coefficient can be defined as:

$$C_s^{eq} = \sigma_{gw}^{e} - (\sigma_{nw}^{e} + \sigma_{gn}^{e})$$ ----------Equation 2.4

It is believed that the value of gas-water interfacial tension decreases dramatically due to the presence of dissolved NAPL (Joos et al., 1985), thus C_s^{eq} is finally zero or negative at equilibrium (Adamson, 1997).

Depending on the wettabilities and spreading characteristics, the three-phase immiscible fluid system may exist as one of the three configurations shown in Figure 2.9 (Øren et al.,1995): in Figure 2.9 (A) no three-phase contact line exists and the intermediate phase, fluid-2, spontaneously spreads over the interface of fluid-1 and fluid-3; in Figure 2.9 (B) there is a three-phase contact line between the fluids; in Figure 2.9 (C) the fluid-2 neither spreads nor forms a contact line.

As regards the potential for recovery of the residual NAPLs, wettability and the spreading of NAPL across the gas-water interface are very important in water wet porous media (Øren et al., 1995; Vizika et al., 1998), because the residual NAPL blobs or ganglia, which initially are entrapped in the soil matrices in the saturated zone, may become mobilized due to the presence of the gas phase. The formation of films and layers caused by the spreading has been demonstrated by micro-model experiments (Dong et al., 1994; Keller et al., 1997). The

fact that low residual saturations can be achieved by drainage for both positive spreading and negative spreading systems is attributed to the presence of thin oil films and layers caused by spreading (Blunt et al., 1995; Keller et al., 1997; Mani et al., 1997; Fenwick et al., 1998).

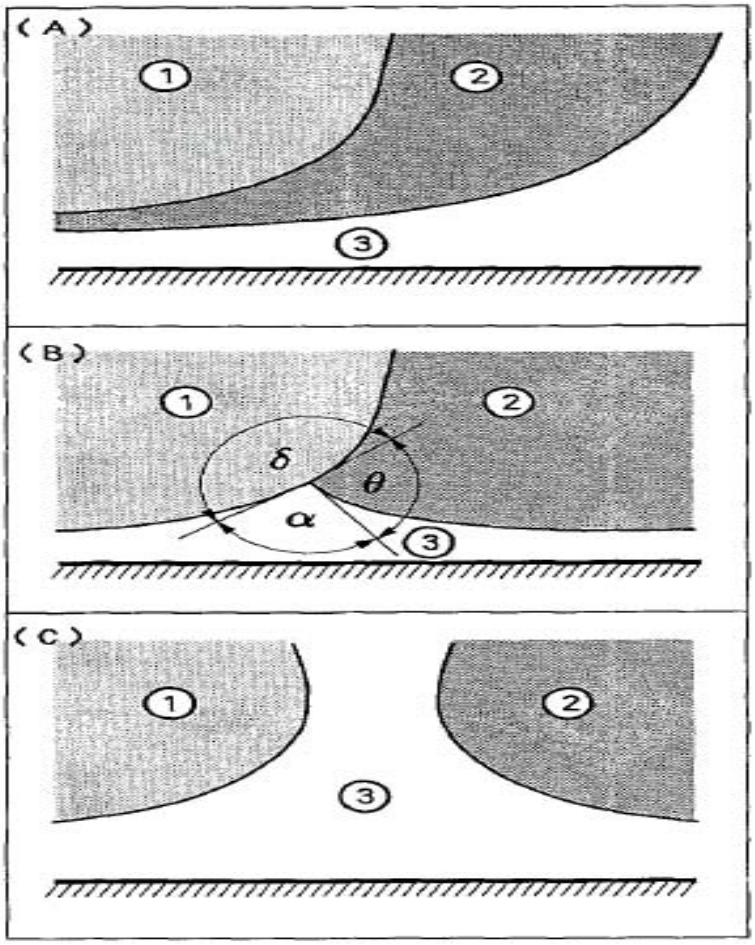

Figure 2. 9 Schematic of three-immiscible-fluid configurations in porous media (Øren et al., 1995)

2.2.3 Capillary Pressure

Capillarity describes the combined effects of interfacial tension and wettability. In porous media, there are numerous small pores connected by pore necks with very small diameters, so that capillarity is of significant importance. The interfaces between fluid phases in porous media are curved (Leverett, 1940) as a result of interfacial tension and wettability, indicating

that pressures in each phase are different. We define this pressure difference across a curved interface between two immiscible fluid phases as capillary pressure:

$$p_c = p_n - p_w$$ ----------Equation 2.5

where p_n and p_w are the pressures in the non-wetting phase and wetting phases, respectively. Generally, the curvature of a curved surface can be characterized by two radii, as shown in Figure 2.10. The fundamental equation of capillarity, Young-Laplace equation, gives the relation between the capillary pressure and the two principal radii of the curvature:

$$p_c = \sigma(\frac{1}{R_1} + \frac{1}{R_2})$$ ----------Equation 2.6

where R_1 and R_2 are the principal radii of the curvature and σ is the interfacial tension between the two immiscible fluid phases.

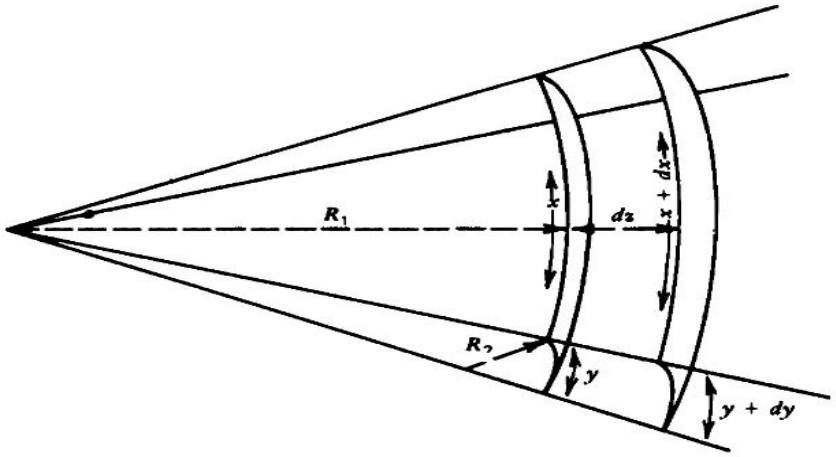

Figure 2. 10 A curved surface characterized by two radii (Adamson, 1997)

In the special case when the liquid drop or a gas bubble takes the shape of the sphere with radius r, the above equation can be simplified as:

$$p_c = \frac{2\sigma}{r}$$ ----------Equation 2.7

In porous media, displacement of fluids is often envisioned to occur in capillary tubes (see

Figure 2.11), in which case pressure can be expressed as:

$$p_c = h = \frac{2\sigma \cos\theta}{r}$$ ----------Equation 2.8

where θ is contact angle, h is capillary rise, and r is the radius of the capillary tube.

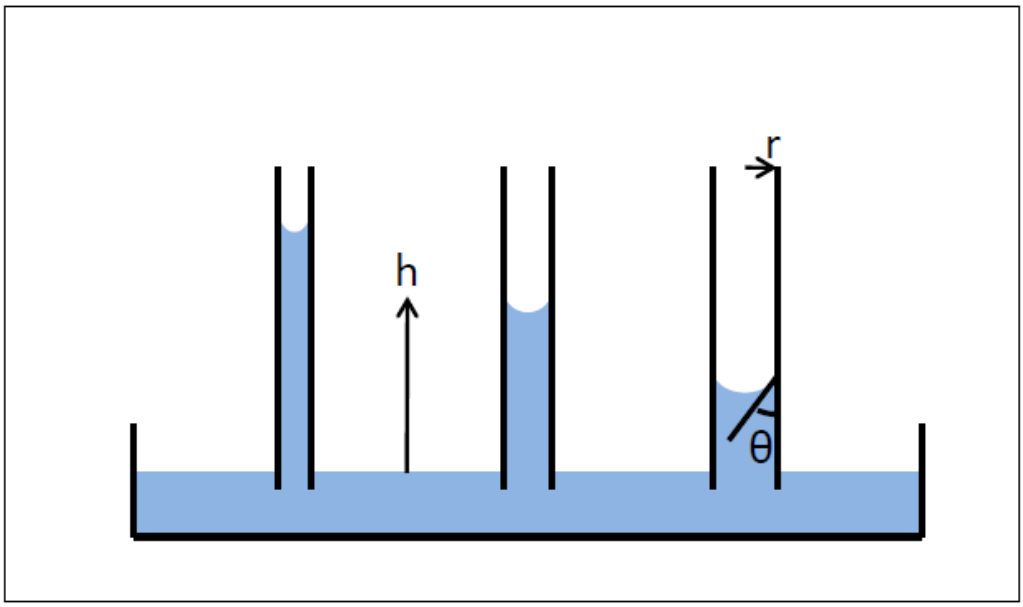

Figure 2. 11 Capillary rises in capillary tubes with different diameters

2.3 Residual Saturation

In a porous medium, assuming that water, oil (NAPL), and gas occupy volumes V_w, V_n, and V_g, respectively, the total pore volume V_p, is written as:

$$V_p = V_w + V_n + V_g$$ ----------Equation 2.9

The saturation of a particular fluid phase, S_i (subscript i represents water, NAPL or gas), is defined as the relative fraction of pore space occupied by the fluid phase (oil, water or gas) in a controlled volume of the porous medium, leading to the following relations:

$$S_i = \frac{V_i}{V_p}$$ ----------Equation 2.10

$$\sum_{i=g,n,w} S_i = 1$$ ----------Equation 2.11

In saturated porous media the NAPL is either continuous or discontinuous. When the NAPL saturation is high, the NAPL exists in the form of pools, is mobile and can be moved under the action of a hydraulic gradient. When saturation is below a certain level, the NAPL exists as ganglia or blobs; it is entrapped in the pore space due to the capillary forces. These disconnected NAPL blobs are extremely difficult to be mobilized by applying a pressure gradient. The saturation at which the NAPL is disconnected is referred to as the residual saturation, S_{rn}, and represents the minimum amount of NAPL phase necessary for NAPL to flow (Oliveira et al., 2003). The residual saturation is affected by the pore size distribution of the medium, wettability, fluid viscosity ratio, density ratio, interfacial tension, gravitational forces, and hydraulic gradients (Mercer et al., 1990).

2.4 Immiscible Displacement Mechanisms

2.4.1 Drainage and Imbibition

Depending on the wetting properties of fluids and porous media, two types of fundamental mechanisms, drainage and imbibition, occur in the course of immiscible displacement in porous media. Figure 2.12 depicts the piston-like displacement processes occurring in capillary tubes which are water wet. Drainage refers to the process when a wetting fluid is displaced by non-wetting fluid, for example water displaced by gas or oil in a water-wet porous medium. When a non-wetting phase (NAPL or gas) is displaced by wetting phase (water), the process is called imbibition.

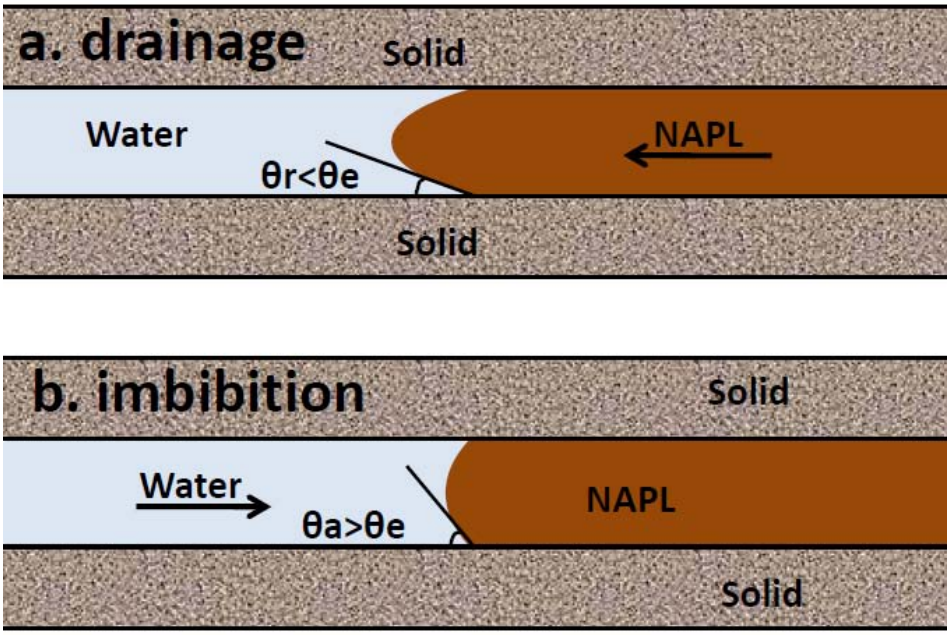

Figure 2. 12 Piston-like displacements in capillary tubes

When three immiscible phases are present in porous media, the displacement mechanisms are more complicated. For example in a water-wet system, there are six possible types of displacements as shown in Table 2.1 (Suicmez et al, 2006).

Table 2. 1 Possible displacement mechanisms in a water-wet porous medium

Name	**Displacement Sequence**
Double Drainage	Gas displaces oil and oil displaces water
Drainage-Imbibition	Gas displaces water and water displaces oil
Imbibiton-Drainage	Water displaces gas and gas displaces oil
Double Imbibition	Water displaces oil and oil displaces gas
Imbibition-Drainage	Oil displaces gas and gas displaces water
Drainage-Imbibition	Oil displaces water and water displaces gas

2.4.2 Capillary Pressure–Saturation Relationships

The capillary pressure （P_c）and saturation (S_n or S_w) relation is one of the constitutive relationships characterizing multiphase flow. It is usually determined through drainage and imbibition experiments on a specific system. Typical P_c - S_n curves for a system containing two immiscible fluid phases are shown in Figure 2.13. The first curve is the primary drainage curve, which starts from S_n = 0. The pressure required to effect drainage increases with increasing S_n . A noticeable characteristic of the P_c - S_n curves is hysteresis, i.e. for a given S_n the value of P_c is not unique. This hysteresis phenomenon is attributed to advancing and receding contact angle, ink bottle effect, and fluid trapping by the mechanisms of by-passing and snap-off.

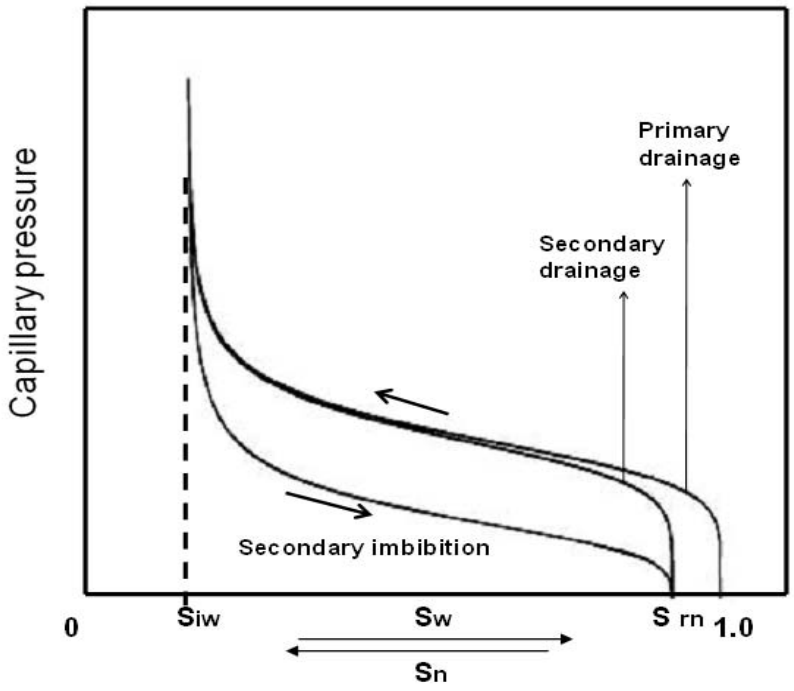

Figure 2. 13 Typical Pc – S curves in porous media

2.4.3 Snap-off and Bypassing

Studies have identified that two main mechanisms, snap-off and bypassing, cause NAPL entrapment in porous media. Figure 2.14 schematically describes the process of snap-off during imbibition in a water wet porous medium. When the aspect ratio，the ratio of the pore body diameter to pore throat diameter, is close to 1, piston-like displacement happens and the non-wetting phase is completely displaced as shown in Figure 2.14 a. However, if the aspect ratio is high, snap-off takes place as shown in figure 2.14 b. The wetting fluid tends to flow along the pore walls in the form of layers or films at the displacement front. When the wetting-phase films reach the pore throat, the high aspect ratio causes the low wetting-phase pressure to increase, and accumulation of wetting-phase at pore throat to take place. Eventually, the wetting phase completely occupies the pore throat and breaks the non-wetting phase, i.e. the snap-off happens. That way, the non-wetting phase is entrapped in the pore body and becomes immobile.

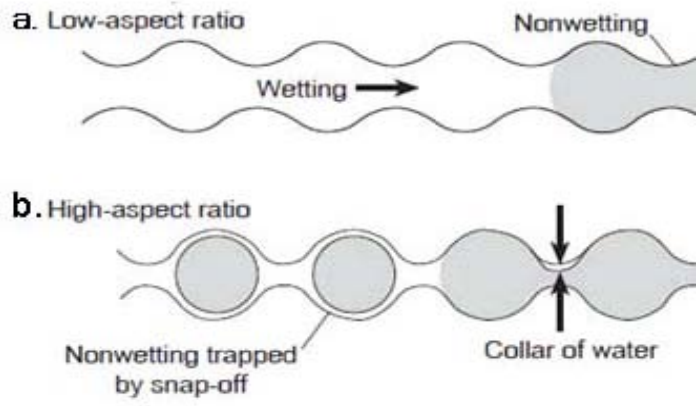

Figure 2. 14 Schematic of snap-off mechanism (after Chatzis et al., 1983)

When NAPL is displaced by water in a water-wet porous medium, the wetting phase tends to flow through smaller pores, bypassing the larger pores that contain the non-wetting phase. The extent of bypassing depends on heterogeneity and the geometries of pores in porous media. A pore doublet model (Chatzis et al., 1983) is usually used to depict the bypassing process, as shown in Figure 2.15. For case (A), during the displacement, the interface of immiscible phases in the upper narrow branch reaches the downstream node first, but still can maintain stable. Thus, non-wetting phase in the lower branch can be completely pushed out and the two interfaces rejoin at downstream node, i.e. no bypassing happens. However, in the case (B), when the wetting phase in the upper narrow branch reaches the downstream node, a stable interface cannot be maintained due to the configuration at the downstream node. Thus, the non-wetting phase in the lower wider branch is disconnected from the main non-wetting phase liquid, and bypassed by the advancing wetting phase.

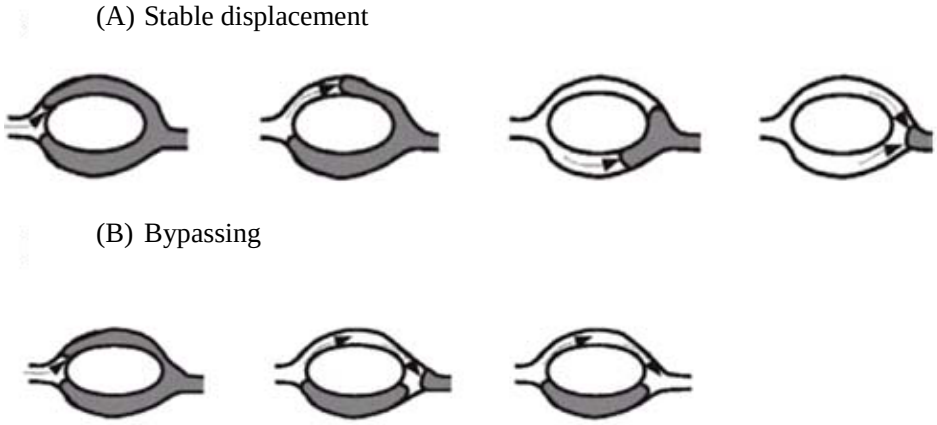

Figure 2. 15 Entrapment of non-wetting phase by bypassing (after Chatzis et al., 1983)

Entrapment mechanisms of NAPLs in porous media determine the size distribution and shape of residual NAPL blobs, which have significant effect on the transport properties and NAPL

fate (Mayer et al., 1992; Reeves et al., 1996). In general, snap-off creates smaller NAPL blobs with spherical shape, which occupy single pore bodies, whereas bypassing produces larger NAPL clusters which involving multiple pores (Cho et al., 2005).

The snap-off and bypassing during imbibition in water-wet porous media are influenced by pore structure, physical properties of the fluid-solid system, and applied pressure gradient. Studies have shown that snap-off strongly depends on wettability and aspect ratio (Chatzis et al, 1983; Li et al., 1986 a & b, Wardlaw et al., 1988; Jerauld et al., 1990; Mahmud et al., 2006); bypassing is generally favored by heterogeneity of porous media (Fagerlund et al., 2007); and snap-off is usually suppressed during high capillary number displacement (Mogensen et al., 2001).

2.4.4 Capillary Number and Bond Number

Immiscible fluid displacement in porous media is generally controlled by capillary, gravitational, and viscous forces (Grattoni, et al., 2001). Capillary forces tend to hold the residual NAPL blobs in the porous medium matrix, while the buoyancy and viscous forces tend to mobilize the trapped NAPL blobs. To mobilize entrapped NAPL blobs, capillary pressure must be overcome, i.e. the vectorial sum of gravitational forces and viscous forces must exceed the capillary forces. In order to quantitatively measure the influence of forces on the mobilization of entrapped NAPL blobs, two dimensionless groups, the capillary number (N_{Ca}) and Bond number (N_{Bo}), are usually used.

The capillary number (N_{Ca}), which is defined as the ratio of viscous forces to the capillary forces, can be used to measure the relative strength of viscous and capillary forces and assess

the potential for the mobilization of trapped NAPL blobs. When NAPL is displaced by water, N_{Ca} is expressed as (Chevalier et al., 2000.):

$$N_{Ca} = \frac{v_w \mu_w}{\sigma_{nw}} \text{ ----------Equation 2.12}$$

where μ_w is the viscosity of water, σ_{nw} is the interfacial tension between NAPL and water, v_w is the Darcy velocity of water. The above equation is a common expression for N_{Ca}, which does not incorporate any properties of the porous media or NAPL blob geometry. If other factors are taken into account, alternative definitions exist (Piri et al., 2007; Jeong et al, 2005; Pennell et al, 1996; Dong et al., 1998; Morrow et al., 1982). The correlation between N_{Ca} and residual saturation, S_{rn}, has been widely studied. A typical correlation between N_{Ca} and S_{rn} is shown in Figure 2.16 (Dawson et al., 1997)

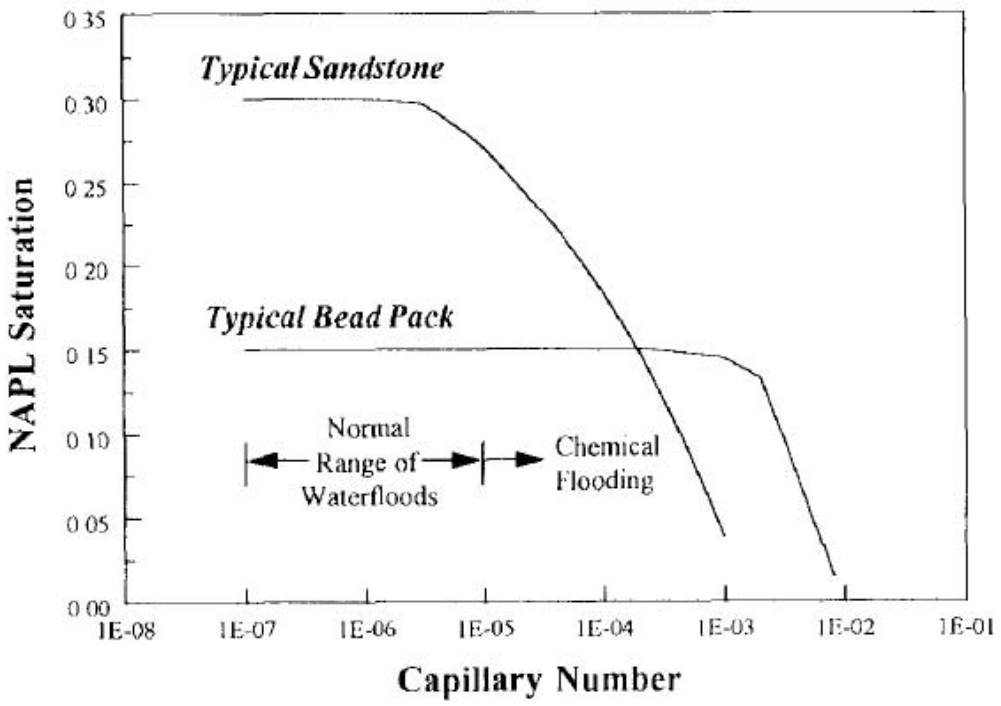

Figure 2. 16 NAPL saturation as a function of N_{Ca} (Dawson et al., 1997)

The Bond number, N_{Bo}, is the ratio of buoyancy (gravitational) to capillary forces and can be expressed as:

$$N_{Bo} = \frac{\Delta\rho g R^2}{\sigma}$$ ----------Equation 2.13

where $\Delta\rho$ is the density difference between the two immiscible fluids, g is the gravitational acceleration constant, R is a characteristic medium size, and σ is the interfacial tension between the two immiscible fluids. N_{Bo} can be also defined in terms of the absolute permeability of the porous medium, k:

$$N_{Bo} = \frac{\Delta\rho g k}{\sigma}$$ ----------Equation 2.14

Figure 2.17 shows the relationship between NAPL saturation and N_{Bo} at various N_{Ca}. It is apparent that N_{Bo} has a greater influence on NAPL saturation at displacement conditions characterized by a low N_{Ca} value.

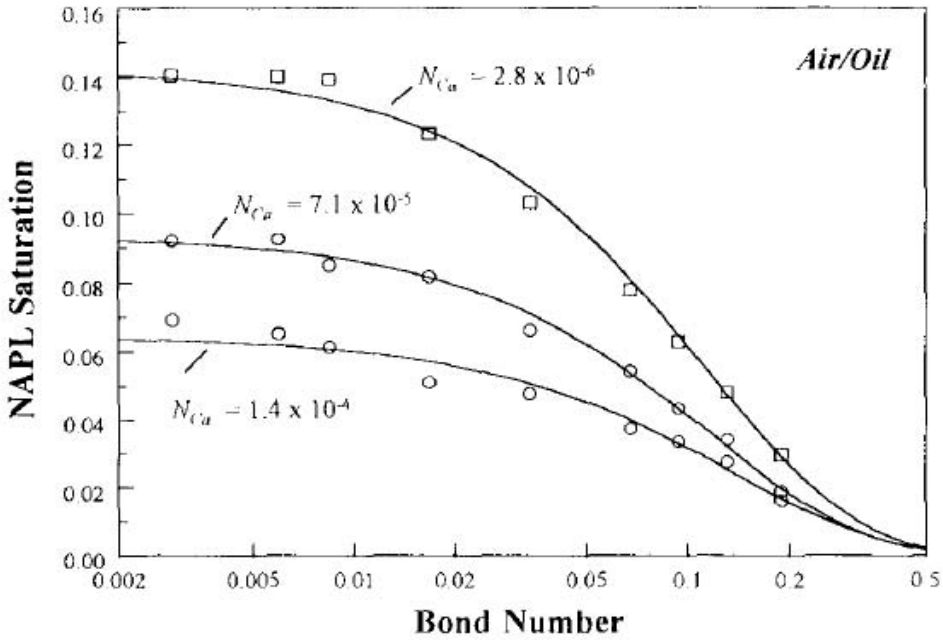

Figure 2. 17 NAPL saturation as a function of N_{Bo} at various N_{Ca} (Dawson et al., 1997)

Actually, viscous and gravitational forces are acting on a trapped NAPL blob simultaneously, such that a trapping number, N_T, defined as the vectorial sum of capillary number and Bond number, is used to measure the combined influence of viscous and gravitational forces (Gioia et al., 2006; Li et al., 2007; Pennell et al., 1996; Longino et al., 1999). The trapping number, N_T, derived by Pennell et al. (1996) is given as:

$$N_T = \sqrt{N_{Ca}^2 + 2N_{Ca}N_{Bo}\sin\alpha + N_{Bo}^2}$$ ----------Equation 2.15

Here N_{Ca} and N_{Bo} are expressed as $\frac{v_w \mu_w}{\sigma_{nw}\cos\theta}$ and $\frac{\Delta\rho g k k_{rw}}{\sigma_{nw}}$ respectively, α is the angle of the direction of flow from the horizontal plane. In the case of $\alpha = 0^o$ or $\alpha = 90^o$, Equation 2.15 is reduced to Equation 2.16 and 2.17:

$$N_T = \sqrt{N_{Ca}^2 + N_{Bo}^2}$$ ----------Equation 2.16

$$N_T = \left|N_{Ca} + N_{Bo}\right|$$ ----------Equation 2.17

2.5 Descriptions of Flow in Porous Media

2.5.1 Darcy's Law

Darcy's Law is a phenomenological equation that describes a fluid flow through porous medium, based on the experimental results of Henry Darcy (1856). When a single phase flows through a porous medium, the relationship of fluid flow rate and pressure drop over the porous medium can be expressed as:

$$\vec{v} = -\frac{k}{\mu}\nabla p$$ ----------Equation 2.18

where k is the absolute permeability of the fluid in the porous medium, $\vec{v}$ is the Darcy velocity; μ is the dynamic viscosity, and ∇p is the pressure gradient vector. In a system which contains two or more immiscible fluids, the fluids can be thought of as residing in different subsections of the pore space (Blunt et al., 1992). The permeability of each fluid will be reduced due to the competition for the pore space. We refer to the permeability of fluid i in this situation as its effective permeability (k_i). At steady-state, Darcy's law can be extended to the multiphase fluid flow as:

$$\vec{v}_i = -\frac{k_i}{\mu_i}\nabla p_i$$ ----------Equation 2.19

where the subscript, i, represents the specific fluid in the multiphase flow system.

2.5.2 Relative Permeability

The concept of relative permeability, k_{ri}, is introduced to measure the degree of permeability reduction in a multiphase flow. The relative permeability is defined as the ratio of effective permeability (k_i) of the fluid i to its absolute permeability (k):

$$k_{ri} = \frac{k_i}{k}$$ ----------Equation 2.20

Thus, Darcy's law in a multiphase fluid flow can also be written in the following form (Jerauld et al., 1990):

$$\vec{v}_i = -\frac{k_{ri}k}{\mu_i}\nabla p_i$$ ----------Equation 2.21

Usually, in two-phase immiscible fluid flow, relative permeability is empirically correlated with the fluid saturation in a porous medium. A typical relative permeability-saturation curve in a two-phase flow system is shown in Figure 2.18 (Dernond et al., 1987). The relative

permeability-saturation relationship and its hysteretic nature are thoroughly discussed by Dullien (1992).

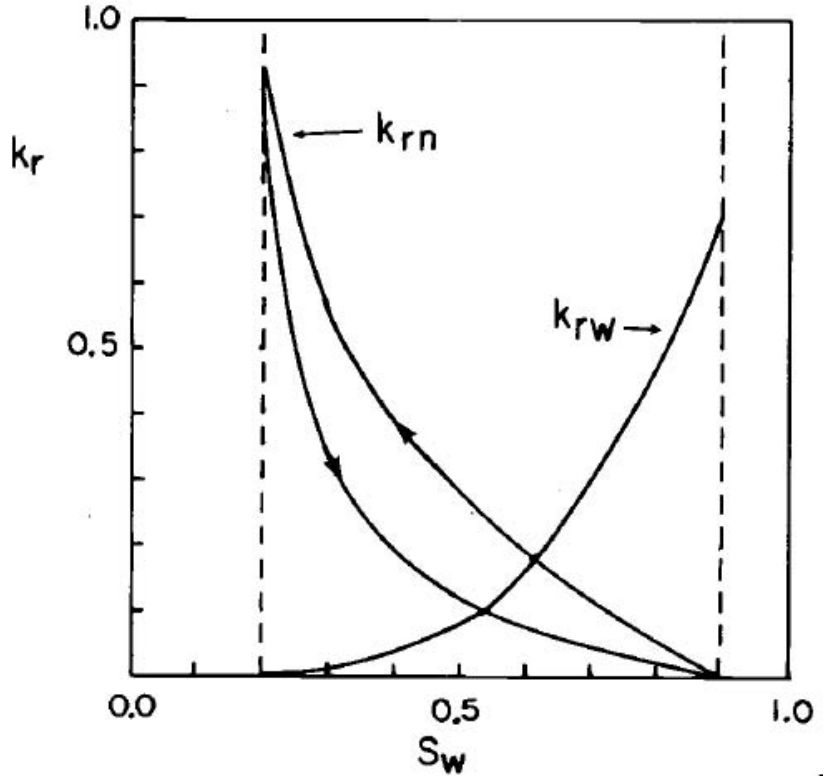

Figure 2. 18 Typical $k_r - S_w$ -saturation curves in porous media (Dernond et al., 1987)

2.6 NAPL Remediation Technologies

During the past few decades, a number of technologies have been developed for remediating NAPL contaminated sites. Based on the applicable regulations and site characteristics, different remediation technologies are designed to achieve different remediation objectives (Lai et al., 2007). The remediation strategies are either to physically remove the pure phase NAPLs from the source zone i.e., source zone remediation, or to reduce the concentration of NAPLs in groundwater to a "safe level" i.e., plume remediation (Soga et al., 2004). Comparatively speaking, source zone remediation technologies which physically remove the

contaminants from the contaminated sites can achieve permanent remediation. Source zone remediation methods are commonly classified into two categories: destructive (e.g. chemical oxidation, biodegradation etc.) and non-destructive (e.g. pump-and treat, surfactant enhanced aquifer remediation, air sparging etc.)

2.6.1 Pump-and-Treat

Pump-and-treat is the most conventional remediation technology to restore NAPL contaminated sites. This technology involves applying hydraulic pressure gradients to the contaminated zone to remove the NAPLs by mobilization and dissolution. Because of the great hydraulic pressure gradients needed to overcome the capillary forces, this technology is not effective for displacing the residual NAPLs (Haley et al., 1991; Mackay et al, 1989). After the treatment by pump-and-treat technology, there is still a considerable amount of residual NAPLs entrapped in subsurface, which acts as long-term source of groundwater contamination (Held et al., 2001). On the other hand, the removal of NAPLs by solubilization requires decades or even longer before the contamination levels are reduced due to the low aqueous solubility of NAPLs (Johnson, et al, 1992).

Many studies have shown that the conventional pump-and-treat technology is very inefficient and its use is practically limited to contaminant plume containment. In order to improve the recovery, the pump-and treat technology can be enhanced by delivery of non-reactive chemicals, such as surfactants (Chevalier et al., 1997; Chevalier, 2003; Childs et al., 2006) and/or cosolvents (Taylor et al., 2004; Palomino et al., 2004) into the contaminated source zones. The surfactant enhanced aquifer remediation (SEAR) can improve the recovery of residual NAPLs by either increasing the solubilities of contaminants in aqueous phase due to

the formation of micelles or/and by mobilizing the entrapped residual NAPLs by lowering the interfacial tension (IFT). Cosolvents, such as ethanol, methanol, and pentanol, can increase the NAPL aqueous solubility due to the changes in the bulk properties of the isotropic solution and enhance the mobilization. Besides, cosolvents can also modify the densities of DNAPL contaminants to improve recovery.

2.6.2 In situ Air Sparging

In situ air sparging (IAS) came into use in the middle of 1980's (Ahlfeld et al., 1994). IAS is effective at removing volatile organic compounds (VOCs) and semi-volatile volatile organic compounds (SVOCs) dissolved in groundwater or entrapped in saturated and unsaturated zones as residuals (Semer et al., 1998). During air sparging, fresh air is injected into groundwater below the contaminated zone. When the injected air moves upwards due to the buoyancy and contacts the contaminants, the VOCs are removed by volatilization (Waduge et al., 2004). Additionally, the injected fresh air brings oxygen into subsurface, enhancing the aerobic biodegradation (Dror et al., 2004). Soil vapor extraction (SVE) is frequently used to remove the gas phase which contains contaminant vapor to improve the remediation efficiency of air sparging. A conceptual model for air sparging is shown in Figure 2.19 (Johnson, 1998).

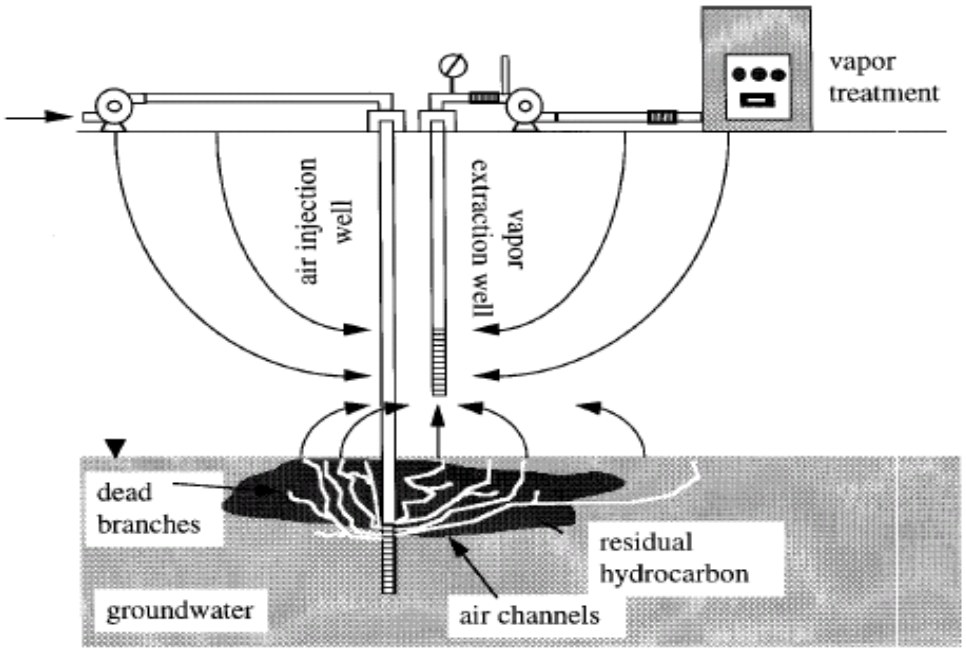

Figure 2. 19 A conceptual model of IAS (Johnson, 1998)

2.6.2.1 Mechanisms and Studies of Contaminant Removal

Generally speaking, physical removal of NAPL by volatilization and aerobic biodegradation are the two main processes for both trapped and dissolved contaminants during air sparging (Johnson et al., 1993; McCary et al., 1996; Adams et al., 2000). Comparatively, the biodegradation rates are much lower than the volatilization rates (Johnston et al., 1998) and depend on the contaminant chemical structure and environment parameters (Suthan et al., 1999), such as oxygen concentration, *pH* , and temperature. However, as contaminant concentration decreases during long-term operations, the air sparging induced biodegradation might play a greater role in contaminant removal (Aelion et al., 2000).

Theoretically, volatilization is a mass transfer process involving VOC partitioning from the liquid phase into the gas phase, i.e., evaporation. During air sparging, two types of

partitioning of the organic contaminant are involved: from the NAPL phase and/or from the aqueous phase into the gas phase. For dissolved VOCs, the mass transfer between liquid and gas phases is governed by Henry's Law:

$p_i = Hx_i$ ---------- ----------Equation 2.22

where p_i is the partial pressure of species i, x_i is the mole concentration of species i in the aqueous phase, and H is Henry's constant. For free-phase liquid, Raoult's law is often used to describe the partitioning of components between the gas and liquid phases:

$p_i = p_i^o x_i$ ----------Equation 2.23

where p_i is the partial pressure of species i, x_i is the mole fraction of species i in the NAPL phase, and p_i^o is the equilibrium vapor pressure of pure species i. Thus, contaminants with higher Henry's constant or higher vapor pressure can be removed by IAS more effectively (Marley et al., 1992; Gordon, 1998; Jang et al., 2009).

Both Henry's Law and Raoult's Law are only valid when the partitioning has reached the equilibrium. However, in reality, the residence time of injected air is such that insufficient contact between air and contaminants results in departure from equilibrium. Thus, the removal of contaminant by volatilization is mainly dependant on the nature of airflow in saturated porous media, the chemical properties of contaminants, and the mass transfer mechanisms (Chao et al., 2008).

To remove the VOCs from the contaminated groundwater, effective contact between the gas and liquid phases must be achieved, and this is crucial to the performance of IAS. The studies indicate that the air flow patterns in saturated porous media are very complex and directly depend on the properties of porous media and operation conditions (Ji et al., 1993; Clayton,

1998). Visualizations conducted by Ji et al. (1993) provided insight into the air flow patterns influenced by grain size, heterogeneity, and air flow rate. The main conclusions were as follows: (1) In homogenous porous media with uniform grain size, bubbly flow occurred in the packs with bigger grain size (4 mm glass beads), and channel flow in the packs with smaller grain size (0.75 mm). (2) The increase of air flow rate caused widening of air flow channels. (3) Slight heterogeneities, achieved by mixtures of glass beads with different sizes, caused significant flow pattern changes. (4) The low permeability layers prevented the direct contact of air with the contaminants above the layers. Adams et al. (2000) used a 2D Plexiglas aquifer simulation test setup to study the removal of benzene by air sparging. They concluded that both dissolved and free-phase benzene could be effectively removed; the removal rate of benzene was increased as the air injection flow rate increased. Groundwater flow could cause migration of NAPLs off-site, but was prevented by the injected air.

To date, several field studies of remediation have been carried out. In order to determine the performance parameters necessary for full-scale design, Murray et al. (2000) carried out a pilot test of air sparging without SVE. The results indicated that air sparging would be very effective in the cleanup of the contaminated site: air sparging was able to dramatically increase the amount of dissolved oxygen decrease the amount of carbon dioxide, and stimulate aerobic bacteria, all of which led to effective removal of VOCs. Bass et al. (2000) studied the data of in situ air sparging tests compiled by IT Corporation. The results indicated that, of the 44 source area air sparging systems, 21 (48%) achieved permanent reductions (greater than 90%), whereas the performance of 10 sites (23%) was unsatisfactory. It was also found that the air sparging was more effective on chlorinated solvent than petroleum hydrocarbon removal, whereas pulsed operation improved the performance of air sparging.

2.6.2.2 Enhanced Air Sparging

Several methods can be used to improve the performance of air sparging. One of these methods is pulsed sparging operation, which creates non-steady-state conditions of groundwater mixing to enhance the mass removal efficiency (Suthan et al., 1999). The performance of pulsed air sparging has been demonstrated in both laboratory and field (Johnson et al., 1999; Heron et al., 2002; Yang et al., 2005; Balcke et al., 2009). Other methods to improve in situ air sparging involve surfactant addition (Kim et al., 2009), and thermal processes (Mohamed et al., 2007).

Heron et al. (2002) used a two-dimensional laboratory tank (4 cm thick, 116 cm long, 56 cm high) with a transparent front wall, allowing visual observation of DNAPL mobilization, to investigate the removal of PCE under pulsed air sparging operation. The initial PCE recovery rates were high, corresponding to fast removal of residual DNAPL within the zone influenced directly by air channels. Increasing the sparging rate and pulsing air injection led to improved mass recovery. Depending on the aggressiveness of the pulsing, the time-weighted mass removal was accelerated by 40%-600%， meaning that 40%-80% of the energy cost used to run the blower may be saved in the field application. Yang et al. (2005) conducted a pilot test to evaluate the influence of pulsed air sparging in a field contaminated by petroleum hydrocarbons. The results indicated that pulsing air injection increased the dissolved oxygen in the saturated zone and hydrocarbon removal rates from both volatilization and biodegradation mechanisms. The contribution of hydrocarbon mass loss via volatilization to the total hydrocarbon mass removal increased during pulsed sparging.

2.6.3 Supersaturated Water Injection

Recovery of residual NAPLs from contaminated soil by supersaturated water injection (SWI) is a novel technology (United States Patent 7300227). Figure 2.20 gives a conceptual description of SWI. Water supersaturated with CO_2 is injected from the SWI well into ground water below the NAPL source zone, where the CO_2-supersaturated water degasses due to the pressure drop. The gas flows upwards under the action of buoyancy. Water and gas are produced by a multiphase extraction well. When the gas flows through the NAPL source zone, the volatile NAPLs can be removed by volatilization similar with air sparging. Furthermore, when the gas flows in a way of disconnection and reconnection due to the presence of the water flow in the NAPL source zone, the entrapped residual NAPL may become mobilized and be removed.

Li (2004) conducted a SWI experiment in a glass column packed with homogenous sand and emplaced a mixture of hexane and octane as contaminant. Table 2.2 is the mass balance of the column experiment after 50 hours of SWI treatment. The results indicated:

(1) The SWI technology was very effective at removing the residual volatile NAPLs, as only less than 7% of the initial residual NAPL remained,

(2) The more volatile NAPL (hexane) was more easily removed by volatilization,

(3) Some residual NAPL was removed by mobilization during SWI operation.

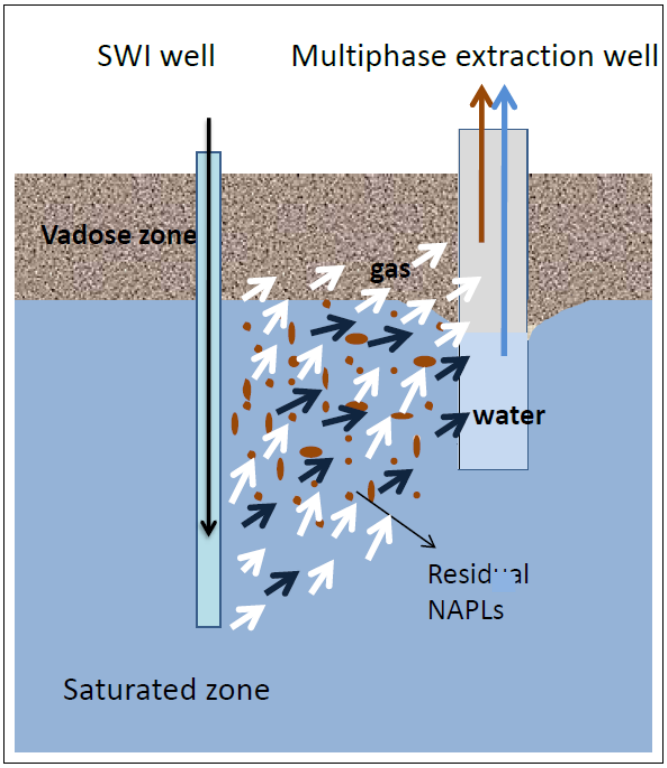

Figure 2. 20 Conceptual model of supersaturated water injection for NAPL recovery (after Li, 2004)

Table 2. 2 Mass balance of SWI column experiment (Li, 2004)

	Hexane	Octane
Initial	33.6g	17.4g
Removed by volatilization	19.2g	5.7g
Removed by mobilization	3.2g	3.5g
Measured removal	22.4g	9.2g
Residual NAPL after experiment	1.2g	2.3g
NAPL unaccounted for	29.8%	33.1%

In order to study the NAPL removal by mobilization during SWI, Li (2004) conducted another experiment in a transparent micro-model. Figure 2.21 is the comparison of the initial NAPL residual saturation and the NAPL remaining in the glass micro-model after 16 minutes of CO_2-supersaturated water injection. Nearly all of the residual NAPL was removed at the end of 16 minutes. A 2D experiment by Li (2004) revealed that the SWI significantly alleviated gas flow channeling in the porous media. Zhao (2006) developed a pore network model to simulate the process of in situ gas evolution during SWI. The simulations showed that bubbles could be nucleated and grow inside the zone of low permeability, in agreement with Li's (2004) 2D experimental result.

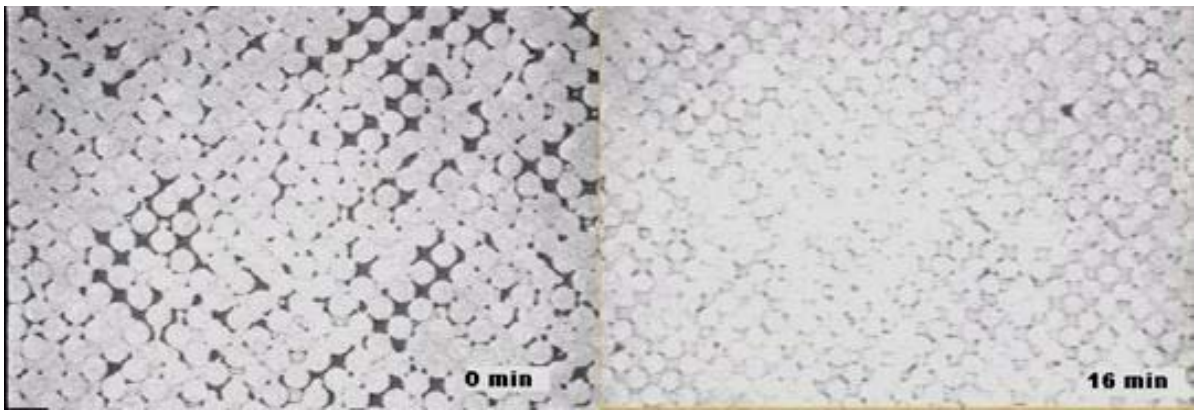

Figure 2. 21 Comparison of the initial NAPL residual saturation and the NAPL remaining in the glass micro-model after 16 minutes of SWI (Li, 2004)

Doughty (2006) conducted field 3-D experiments in a site with relatively homogeneous fine to medium sand at CFB Borden. The experiments determined the zone of influence during SWI to provide for field scale NAPL recovery design. Based on Li's (2004) laboratory results, Nelson (2007) conducted a field trial of residual LNAPL recovery using CO_2-supersaturated water injection at CFB Borden. The experiments were conducted in a hydraulically isolated cell. The contaminants (80 liters of pentane, 80 liters of hexane, and 40

liters of Soltrol 130) were emplaced below the water table. After 22.25 days of operation over three months, the results (see Table 2.3) showed that 77% of pentane and 53% of hexane were removed by volatilization alone, respectively; the total recovery of volatile NAPLs (pentane and hexane) was 64%; however the recovery of non-volatile NAPL (Soltrol 130) was negligible. The distributions of residual NAPL concentration in soil sample after SWI remediation showed that the NAPL moved upward to the water table, indicating the mobilization of NAPL took place during SWI operations.

Table 2. 3 Total masses of pentane and hexane removed in the vapor phase during the entire experiment. The percentages are based on the initial masses (the mass in the subsurface after the use of soil vapor extraction); 42.7 kg of pentane and 46.7 kg of hexane (Nelson, 2007)

	Pentane		Hexane		Total	
	Mass, kg	%	Mass, kg	%	Mass, kg	%
Phase I	24	57	15	35	39	40
Phase II	9.3	20	8.3	18	17	20
Total	33	77	23	53	57	64

Chapter 3

Mobilization of Entrapped Residual NAPL under Three-Phase Flow Conditions

3.1 Scope

Mobilization of entrapped residual NAPLs in saturated porous media during supersaturated water injection (SWI) is a complex three-phase fluid flow process. In order to understand the mechanisms of NAPL recovery via mobilization of residual NAPLs during SWI, four experiments were conducted in sand-packed columns. One of the column experiments was operated in three different modes, gas sparging, gas-water co-injection at different water flow rates, and CO_2-supersaturated water injection, to compare the influence of the different factors on the recovery behaviors. Another column experiment was conducted under water-flooding at various water flow rate levels to examine the mobilization behavior of entrapped residual NAPL. The other two columns were operated under intermittent gas sparging schedules with air and carbon dioxide sparging respectively to investigate the mobilization of the residual NAPL and the displacement mechanisms during the gas de-saturation in the columns after gas sparging.

3.2 Experimental Setup and Procedures

The experimental setup is shown in Figure 3.1. All experiments were conducted in a Plexiglas column of 150 cm long and 3.8cm in inner diameter. The columns were packed with silica sands. Non-volatile LNAPL, kerosene, was used as contaminant. The properties of sand and kerosene can be found in Table 4.1 and 4.2, respectively.

The carbon dioxide and air were supplied by a CO_2-cylinder and utility system, respectively, and tap water was used. CO_2-supersaturated water was produced by a gPRO^{TM} gas saturator, which is essentially a hollow-fiber membrane contactor. Further information about the gPRO^{TM} is given in section 4.2.1 in Chapter 4. The fluids were injected at the bottom of the sand-packed column containing residual kerosene. The injection flow rates were carefully controlled by two separate metering valves. The effluent from the column entered into a three-phase separator. The volume of water and NAPL produced during the experiment could be measured by their accumulations in the separator. The gas phase came out of the top of the separator, and the gas flow rate was measured by a mass flow meter (Omega, model FMA 3304) and/or gas bubble flow meter. The pressure at the bottom of the column was measured by a pressure transducer (Validyne, model DP10-44). In the experiments, the instantaneous pressure values at the bottom of the column and the gas flow rates in the effluent from the column were automatically recorded by computer using Lab View 7.1, which was connected to the pressure transducer and mass flow meter.

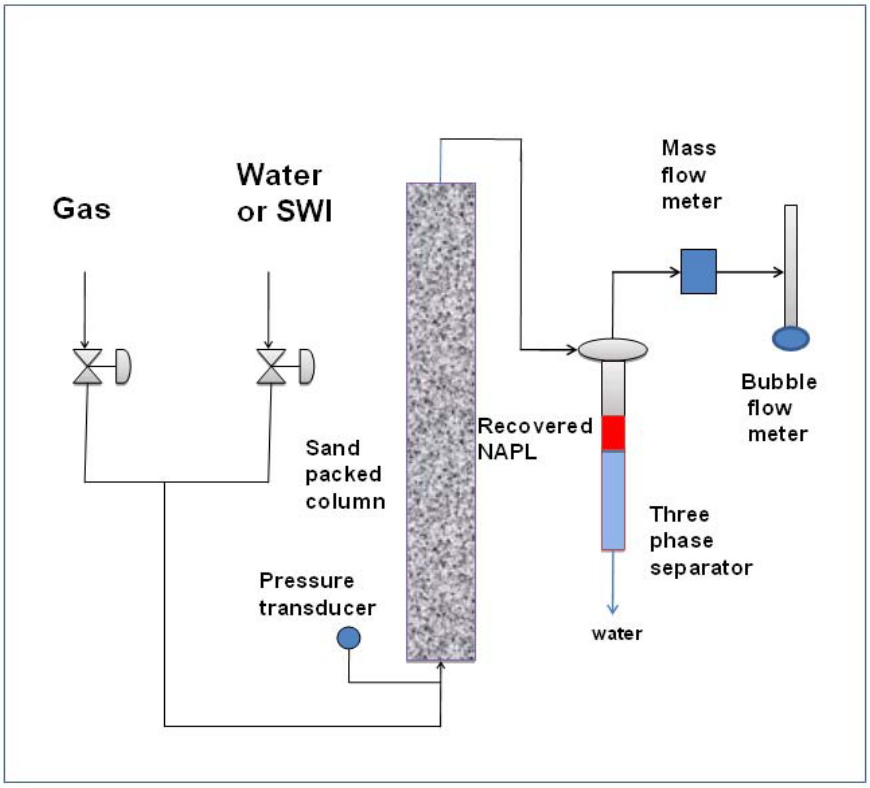

Figure 3. 1 Schematic of experiment setup for gas sparging, co-injection, and SWI

3.2.1 Column Packing

The columns were wet-packed under vibration. The column was fixed on a vibrator before packing started. A known volume of de-aired tap water (about 650 ml) was filled into the column. Sand was loaded from the top of the column after the vibrator was turned on. The loading rate of sand was controlled by a funnel with suitable opening. This operation must be continuous to prevent the formation of any layering in the column during the packing. Sand loading was stopped when the sand in the column reached 1-2 cm above the target height. After about 1 hour of vibration after sand loading stopped, the sand pack became tighter, and the sand height would continuously drop. More sand was then added into the column to achieve the target height. Every time sand was added, manual mixing with a stick was needed to ensure packing uniformity. Following packing, the excess water was removed from the

sand pack and measured. The volume of water that remains in column was the pore volume of porous medium (V_p). The bulk volume of the porous medium (V_b) was the space of the column occupied by water and sand. Thus the porosity of the porous medium was found as:

$$\Phi = \frac{V_p}{V_B} \quad \text{----------Equation 3.1}$$

3.2.2 Permeability Measurement

The column was filled with de-aired water to the very top and a short tube was connected to the bottom of the column. The valve at the bottom was opened to let the water drain out of the column while the water level was kept at the very top. The steady flow rate of the water was measured by a graduate cylinder and stop watch. The permeability was calculated by straightforward application of Darcy's law:

$$k = \frac{Q\mu}{A}\frac{L}{H\rho_w g} \quad \text{---------- Equation 3.2}$$

where k is the permeability, cm^2,

Q is the water flow rate, ml/s,

μ is viscosity of water, cp,

L is the length of the porous medium, cm,

A is the sectional area of the column, cm^2,

H is the hydraulic height (from outlet to the very top of the column), cm,

ρ_w is the density of water, g/cm^3,

g is gravitational acceleration, $981\,cm/s^2$.

3.2.3 Establishment of Residual NAPL Saturation

After permeability measurement, the excess water was removed from the top of the sand column. NAPL was added from the top of the column, and the water displaced out from the outlet at the bottom of the column was collected. The operation was continued until the NAPL breakthrough was observed at the bottom. The volume of water displaced by NAPL was the volume of NAPL emplaced in the column (V_{en}).

The excess NAPL was then removed from the top of the sand column. Rings with fine screen and supported springs were installed on the top of the column to prevent the fluidization of sand during subsequent experiments and the upper flange was bolted to the column. At this stage, the column was ready for water flooding to establish residual NAPL saturation. De-aired water was injected into the column from the bottom at a flow rate of 3 ml/min by a syringe pump (Harvard Apparatus, Model 944). The NAPL displaced by water was collected from the top of the column. Water-flooding continued until no more NAPL came out of the column. The volume of the NAPL displaced by water-flooding, V_{1dn}, was measured. The residual NAPL saturation, S_{irn}, was calculated by the following equations:

$$V_{1rn} = V_{en} - V_{1dn} \quad \text{---------- Equation 3.3}$$

$$S_{irn} = \frac{V_{1rn}}{V_p} \times 100\% \quad \text{---------- Equation 3.4}$$

where V_{irn} is the volume of residual NAPL in the column.

3.2.4 Gas Sparging, Co-injection, and Supersaturated Water Injection

Gas sparging: Following the establishment of residual NAPL saturation in the column, gas (carbon dioxide or air) was injected from the bottom of the column. During the sparging operation, the gas flow rate was controlled as low as possible in the early stage, to ensure that the water flow rate caused by gas injection was less than 3 ml/min. The effluent of the column, including gas, water, and recovered NAPL, was separated in the three-phase separator. Produced volumes of water (V_{wp}) and NAPL (V_{np}) during the operations were carefully measured at various times to calculate the instantaneous water, NAPL, and gas saturations in the column by the following equations:

$$S_g = \frac{V_{wp} + V_{np}}{V_p} \quad \text{----------Equation 3.5}$$

$$S_{rn} = \frac{V_{irn} - V_{np}}{V_p} \quad \text{---------- Equation 3.6}$$

$$S_w = 1 - S_g - S_{rn} \quad \text{----------Equation 3.7}$$

where V_p and V_{irn} are the pore volume of the porous medium and the initial residual NAPL in the column, respectively. The gas flow rate was then gradually increased, more water and NAPL were produced, and the gas saturation in the column increased. When the gas saturation in the column approached 40%, the gas flow rate was kept unchanged to let the column run at steady state. After about 8 hours of steady gas sparging, the gas flow rate was increased to produce more water and NAPL. A maximum gas flow rate of 80ml/min was

used in gas sparging experiments, while the gas saturation was about 40%.

At the conclusion of the operation described above, hereafter referred to as 1st sparging, gas continued to come out of the column after gas injection stopped and gas saturation in the gas saturation in the column decreased. The instantaneous gas saturations at corresponding time were estimated by the changes of the headspace of water above the sand pack. The free NAPL in the top of the column was displaced out by injecting water from the sample port which was located above the sand pack and measured. Before next gas sparging, the free NAPL layer on the top of the column in the headspace was displaced the same way. Except for the 1st sparging operation, no steady gas sparging was run.

Co-injection and SWI: After gas sparging, tap water was injected into the column from the bottom of the column at the target flow rate, while the gas flow was still controlled at around 80 ml/min. Four different levels of water flow rates, 3, 10, 20, and 30 ml/min, were applied. Firstly, the column was run at the lowest level of 3 ml/min. This operating condition was maintained until no more NAPL was produced. Then, the water flow rate was increased to the next higher level. The experiments were conducted in an intermittent schedule, i.e. after one day's operation, injection ceased and the system was let to stand overnight. Every time the experimental operation was restarted with gas sparging until the gas saturation reached about 40% and gas flow rate was around 80 ml/min. For SWI operations, CO_2-supersaturated water was directly injected into the column; no gas sparging was applied before SWI. The SWI operation procedures are described in detail in section 4.2.3 in Chapter 4.

3.2.5 Measurement of Saturations

At the end of a gas sparging or SWI operation, the saturations of NAPL, water and gas were determined by the total weight changes of the column and the volume of NAPL recovered based on mass balance. The residual NAPL saturation (S_{rn}), water saturation (S_w), and gas saturation (S_g) in the column were calculated as follows:

$$S_{rn} = \frac{V_{irn} - V_{cn}}{V_p} \times 100\% \text{ ----------Equation 3.8}$$

$$S_w = \frac{(V_p - V_{irn})\rho_w + V_{cn}\rho_n - (M_{ic} - M_c)}{\rho_w V_p} \times 100\% \text{ ----------Equation 3.9}$$

$$S_g = 1 - (S_{rn} + S_w) \text{ ----------Equation 3.10}$$

where V_{irn} is the initial volume of residual NAPL in the column before SWI, ml,

V_{cn} is the cumulative volume of NAPL recovered, ml,

ρ_w is the density of water, 1.0 g/cm^3,

ρ_n is the density of NAPL, g/cm^3,

M_{ic} and M_c are initial and final weight of the column, g.

For residual gas saturation measurement after overnight standing, water was added to the very top of the column before the column was weighed.

3.3 Experiment Results and Discussion

Four column experiments are discussed below. The operations associated with experiment No.1 involved three stages. In stage I, only free CO_2 gas was injected. In stage II, free CO_2 gas and tap water were co-injected into the column. In stage III, only CO_2-supersaturated water was injected. Experiment No.2 was operated under various water-flooding conditions varying from 3 to 75 ml/min. Experiments No.3 and No.4 were gas-sparged intermittently with air and CO_2, respectively. Column properties and operating parameters are summarized in Table 3.1.

Table 3. 1 Main properties and operating parameters for experiments No.1 - No.4

Experiment ID.	No. 1	No.2	No. 3	No.4
Type of column pack	Homogeneous	Homogeneous	Homogeneous	Homogeneous
Sand grain size, μm	305.8	324.1	324.1	324.1
Bulk volume, ml	1596	1586	1586	1586
Porosity, %	39.0	34.8	34.9	34.6
Permeability, Darcy	30.2	35.8	39.6	37.8
Type of NAPL	Kerosene	Kerosene	Kerosene	Kerosene
Volume of NAPL emplaced,	385ml	392ml	386ml	382ml
saturation of NAPL emplaced,	68.6%	71.0%	69.8%	69.6%
V of residual NAPL, after water-flooding	88 ml	97 ml	106.2ml	100.2ml
Residual saturation, Initial	15.7%	17.6%	19.2%	18.3%
Operation conditions	Sparging, co-injection, SWI	Water flooding	Intermittent spagring	Intermittent spagring
Final cum. recovery	55.5%	9.4%	41.1%	40.9%
Residual saturation, Final	7.0%	15.9%	11.3%	10.8%

3.3.1 Comparison of Gas Sparging, Gas-water Co-injection, and Supersaturated Water Injection

Figure 3.2 is a three-phase diagram depicting the path of saturation change for gas, water and NAPL during the water flooding and the first gas sparging in experiment No.1. Water flooding at injection flow rate of 3 ml/min started at point A, where the gas, NAPL, and water saturations were 0%, 68.6%, and 31.4%, respectively, and ended at point B, where the gas, NAPL, and water saturations were 0%, 15.7%, and 84.3%, respectively. As a result of NAPL displacement during the water flooding, the residual NAPL saturation in column decreased by 52.9%. After the water flooding, the NAPL phase in the porous became isolated (trapped) by snap-off and/or bypassing. The 1st gas sparging started at point B and ended at point C, where the saturations of gas, NAPL, and water were 39.1%, 15.4%, and 45.5% respectively. During the 1st gas sparging, the gas saturation increased by 39.1%, whereas the saturations of water and NAPL decreased by 38.8% and 0.3%, respectively.

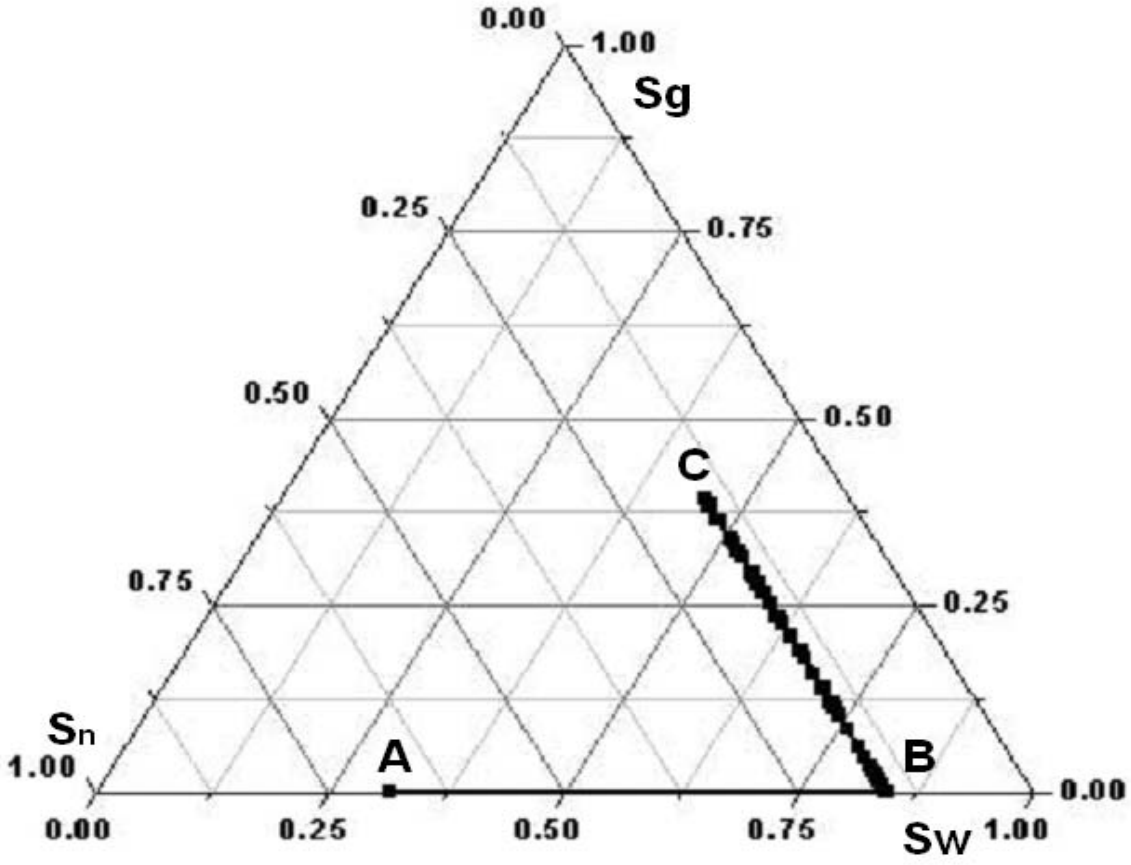

Figure 3. 2 Three-phase saturation diagram during water flooding and 1st gas sparging in experiment No.1

Recoveries of water and NAPL, and gas saturation in the column vs. the time elapsed are plotted in Figure 3.3 to investigate the recovery behaviors during the 1st gas sparging in detail. Gas breakthrough at the top of column occurred at the 75th minute from the start of gas sparging, when the gas saturation in the column was around 11%. Before the gas breakthrough, there was no NAPL recovery at all, although the water recovery was 12.9%. About 5 minutes after the gas breakthrough, immediately 0.5 ml of NAPL recovery was observed in the separator, indicating a small NAPL bank had formed. The NAPL recovery rate remained at a relatively high level for about 90 minutes, then decreased and was maintained at a rather low level, while the water recovery and the build-up of gas saturation

in the column depended on the increments of the gas flow rate. During the period of steady gas sparging operation, the gas flow rate was constant all along, and there was neither gas saturation build-up in the column nor water or NAPL recovery. After steady gas sparging, when the gas flow rate was increased again, the gas saturation began to build up and more water and NAPL were recovered, but the NAPL recovery rate was very low, indicating there was no NAPL bank formed during about 8 hour's steady gas sparging. Finally, when the gas sparging stopped at the 1200th minute, gas saturation reached 39.1%, and 46.1% of water and 1.8% of NAPL were produced.

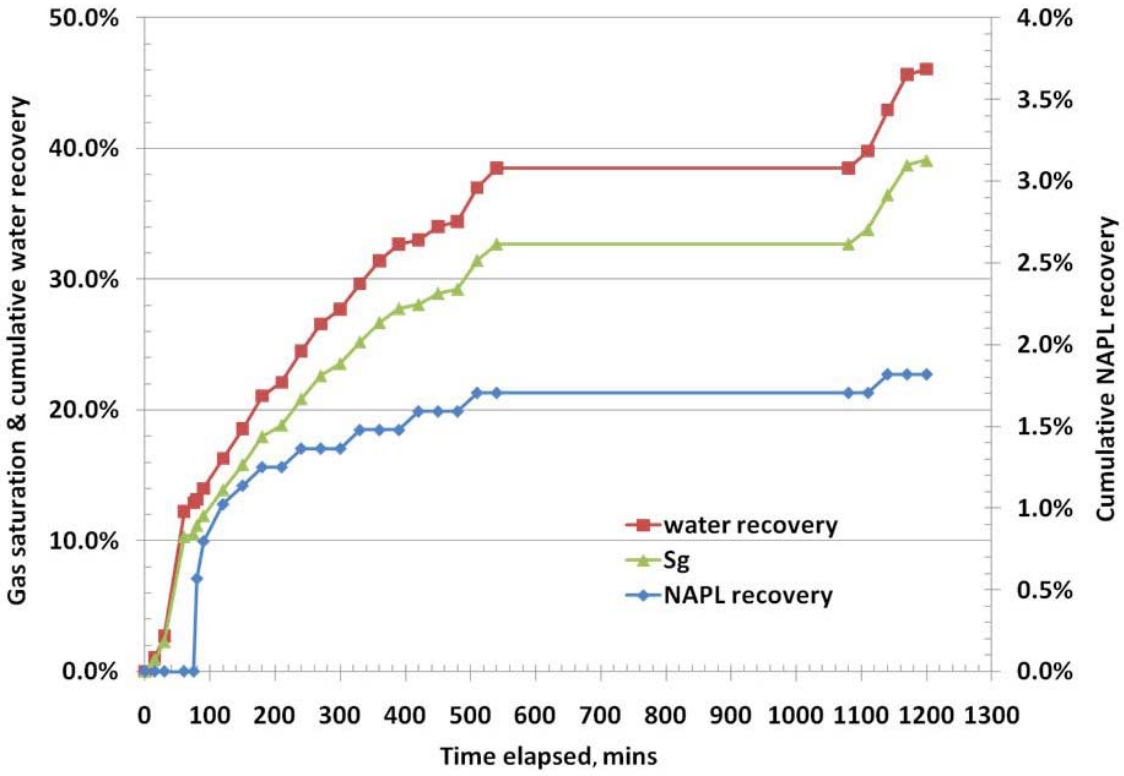

Figure 3. 3 Gas saturation, water and NAPL recoveries vs. time elapsed in experiment No.1 during the 1st gas sparging

In the period prior to gas breakthrough, only water and NAPL phases existed between the gas-liquid displacement front and the top of the column, so that any the displacement in that zone was single displacement of the kind taking place during water-flooding. Furthermore, the rates of water flow out of the column caused by gas injection were carefully controlled to less than 3 ml/min, the water flow rate of the water-flooding, such that the viscous forces exerted on NAPL ganglia by water flow were insufficient to mobilize the entrapped residual NAPL, resulting in no NAPL recovery. The recovery of NAPL after the gas breakthrough must be attributed to the presence of gas at and behind the displacement front in the saturated porous medium. At the gas-liquid displacement front, a NAPL bank was likely formed by double drainage displacement mechanisms. When gas was injected into the saturated porous medium with residual NAPL saturation, double drainage displacement, the process of continuous gas phase displaces the entrapped residual NAPL phase which then displaces water, most likely took place. That way, the entrapped disconnected NAPL phase became partially reconnected by the double drainage displacements through the pore migration and coalescence of the NAPL clusters (Suicmez et al., 2008), gradually forming a NAPL bank. Thus, when the displacement front left the porous medium, i.e., at the gas breakthrough, the NAPL bank moved out of the column and a higher NAPL recovery rate was obtained. The continuous low NAPL recovery after the NAPL bank completely moved out of the column might be due to the continuous fragmentation and reconnection of the gas phase in the presence of water flow (Vedvik et al., 1998).The movement of gas that way would cause the redistribution of the entrapped residual NAPL, forming bigger NAPL clusters that could be mobilized by both viscous and buoyancy forces. However, during steady gas sparging, there was no water flow present, the above mentioned continuous fragmentation and reconnection

of the gas phase could not happen, resulting in the complete ineffectiveness of steady gas sparging on the recovery of the entrapped residual NAPL in the saturated porous media by mobilization mechanisms.

Figure 3.4 is the plot of NAPL recovery and residual saturation of NAPL vs. time elapsed for experiment No1. The NAPL recoveries during various operation conditions in the experiment are summarized in Table 3.2. In stage I, 1.6 ml of NAPL was recovered, only accounting for 3.2% of the total recovery. In stage II, 43.1 ml of NAPL was recovered, accounting for 86.5% of the total recovery. The recovery curve in Figure 3.4 clearly shows that substantial increase of NAPL recovery was obtained very soon after a 3ml/min of water flow was co-injected with an 80 ml/min of gas flow into the column. When the NAPL recovery reached a plateau under this operating condition, 35.1 ml of NAPL was recovered. This NAPL contributed 81.4% to the recovery in stage II, or 70.5% to the total recovery, indicating that higher water flow rate was not necessarily required to mobilize the entrapped residual NAPL in saturated porous medium under gas-water co-injection conditions. As the residual NAPL saturation in porous medium became lower, a higher water flow rate was needed to obtain additional recovery of the residual NAPL. The NAPL recoveries under operating conditions with higher water flow rates, 10, 20, and 30 ml/min, were only 10.4%, 4.6%, and 1.0%, and accounted for 12.1%, 5.3%, and 1.2% of the recovery of stage II, respectively.

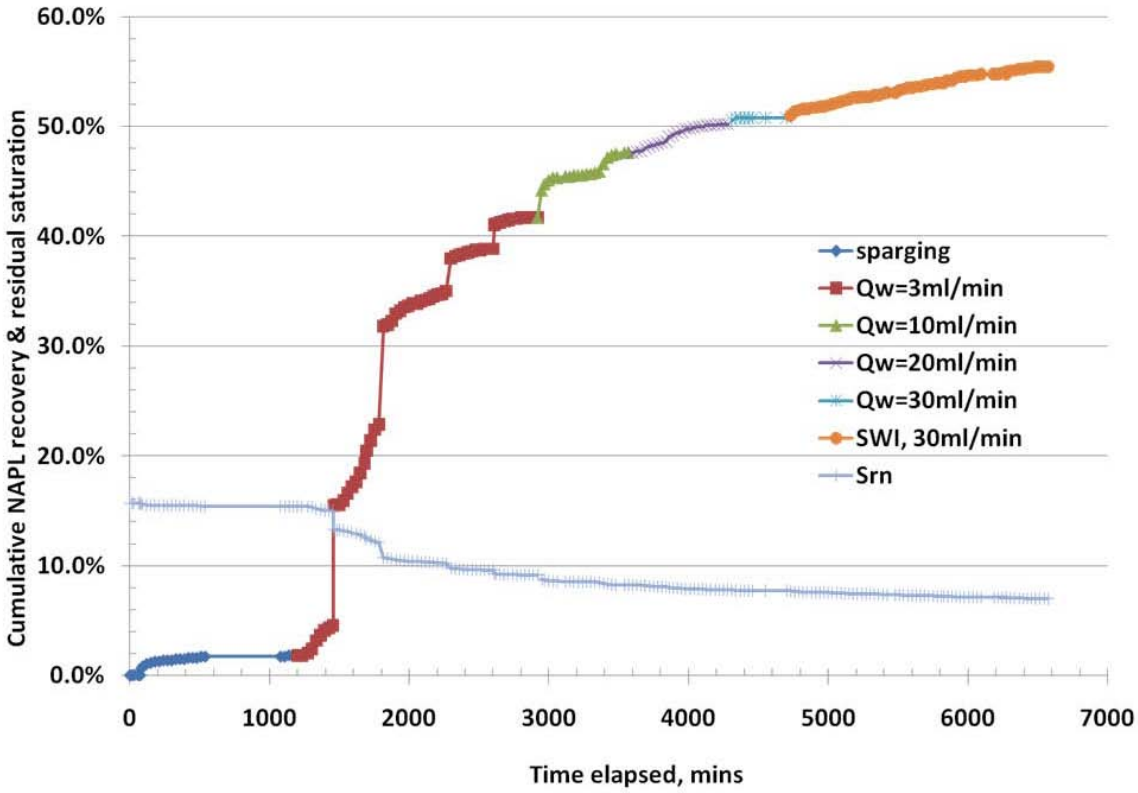

Figure 3. 4 Plot of NAPL recovery and residual NAPL saturation vs. time elapsed in experiment No.1 for the entire operation

Table 3. 2 Summary of NAPL recovered under various operation conditions for experiment No.1

stage	Target condition		Recovered by flows	Recovered from standing	Sum	Weight ,%	
	Q_g, ml/min	Q_w, ml/min					
I	80	0	**1.6 ml**	**0 ml**	**1.6 ml**	**3.2**	
II	80	3	13.1 ml	22 ml	35.1 ml	70.5	81.4
	80	10	4.6 ml	0.6 ml	5.2 ml	10.4	12.1
	80	20	1.9 ml	0.4 ml	2.3 ml	4.6	5.3
	80	30	0.2 ml	0.3 ml	0.5 ml	1.0	1.2
	Sub-sum		**19.8 ml**	**23.3 ml**	**43.1 ml**	**86.5**	100
III	80	30	**5.1 ml**	**0 ml**	**5.1 ml**	**10.2**	
Sum,			26.5 ml	23.3 ml	49.8 ml	**100.0**	
Weight, %			**53.2**	**46.8**	**100.0**		

The sudden increase of NAPL recovery by gas-water co-injection may be attributed to the following two aspects. Firstly, as mentioned above, the higher water flow rate might enhance the processes of fragmentation and reconnection of gas phase, favoring the reconnection of the isolated NAPL clusters in the porous medium. Secondly, it could increase the viscous forces acting to mobilize the entrapped residual NAPL.

In stage III, 5.1 ml of NAPL, or 10.2% of the total NAPL recovery, was obtained by SWI at almost the same flow rates of water and gas with those in the last water-gas co-injection operation, indicating that SWI was more effective at recovering the entrapped residual NAPL than water-gas co-injection. The possible reason might be that during SWI gas evolves in situ (Zhao, 2006; Li 2004), and the gas can reach areas which are not accessible to gas during gas-water co-injection. Thus, higher sweeping efficiency could be achieved in SWI operations.

Another interesting observation of the recovery behaviors in the experiment was that 23.3 ml of NAPL, or 46.8% of the total recovery came from the sparging operation after the system was let to stand overnight. At higher residual saturations, the NAPL recoveries realized that way were higher. It seems that during the process of gas de-saturation from high gas saturation to the residual gas saturation level, significant reconnection of isolated residual NAPL clusters happened, resulting in the increase of residual NAPL mobilization.

3.3.2 Intermittent Gas Sparging

Figures 3.5 and 3.6 are three-phase diagrams describing the saturation paths during the operations for experiments No.3 (air sparging) and 4 (CO_2 sparging). The saturation changes during water-flooding and the 1st gas spargings were similar with what happened in

experiment No.1. The NAPL saturations for experiment No.3 and 4 changed from 69.8% and 69.6% to 19.2% and 18.3% respectively during the water-flooding at 3 ml/min water flow rate, from point A to B. The saturations of gas, water, and NAPL changed from 0%, 80.8%, and 19.2% to 42.9%, 38.3%, and 18.8% for experiment No.3, and from 0%, 81.7%, and 18.3% to 41.6%, 40.6%, and 17.9% for experiment No.4 respectively during the 1st gas spargings, from point B to C. The situations after the 1st gas spargings will be introduced and discussed later.

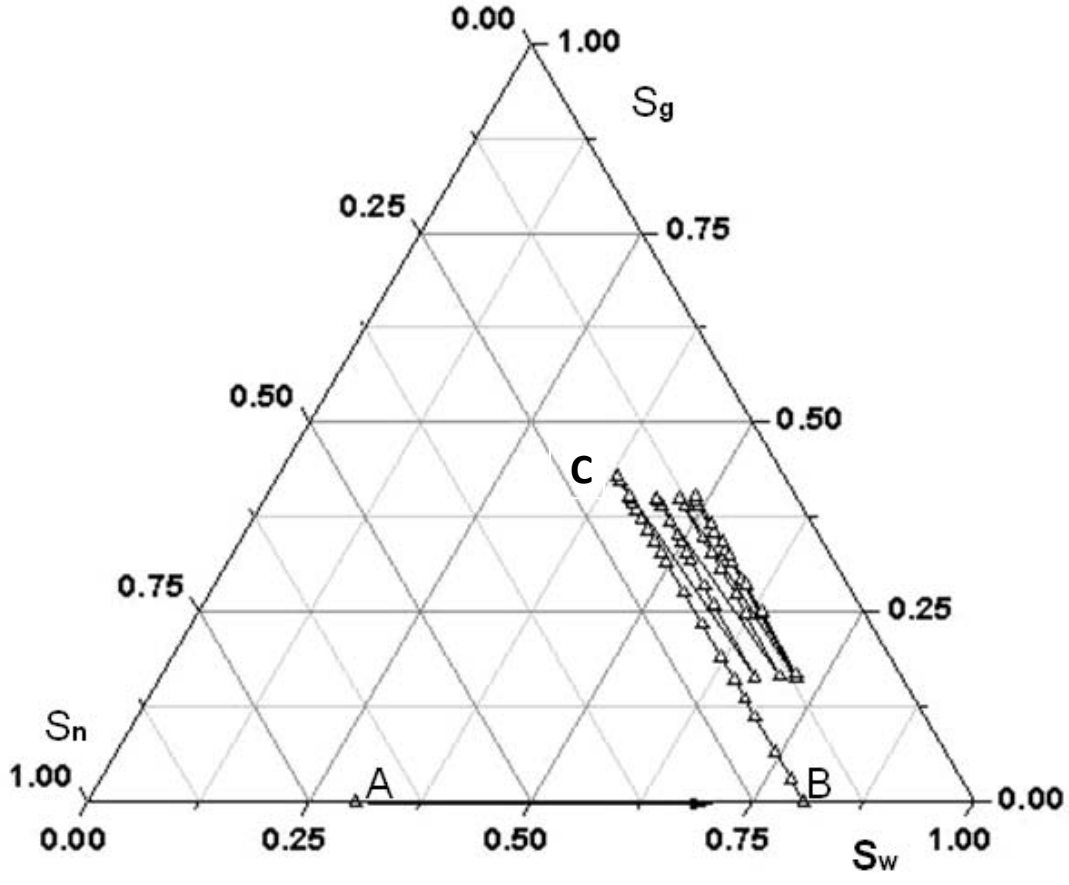

Figure 3. 5 Three-phase diagram of saturation paths of NAPL, gas, and water in experiment No.3

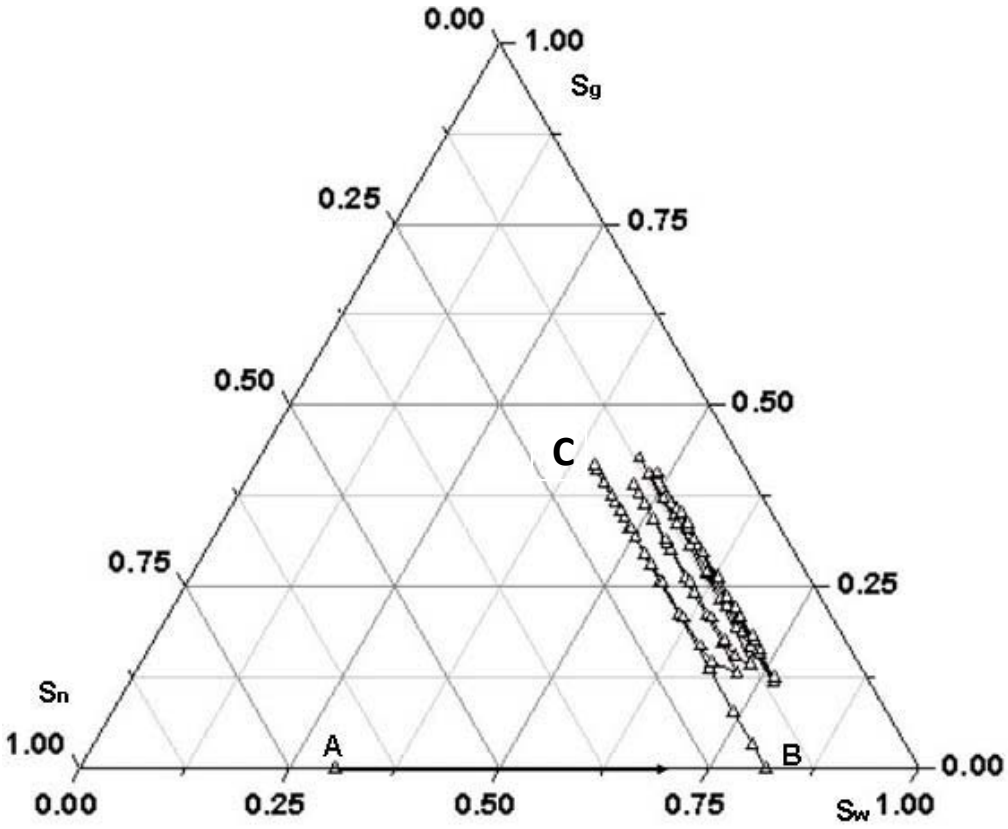

Figure 3. 6 Three-phase diagram of saturation paths of NAPL, gas, and water in experiment No.4

The recoveries of water and NAPL, and saturations of gas in the column vs. time elapsed are plotted in Figures 3.7 and 3.8. Similar to the situations in experiment No.1, gas breakthroughs happened when the gas saturations were around 10% in the column. Before gas breakthrough, there was no NAPL recovery. Significant NAPL recovery occurred after gas breakthrough due to the formation of a NAPL bank, and then the NAPL recoveries fell to a very low level and remained at this low level until the steady gas sparging started. During steady gas spargings, no NAPL banks were formed.

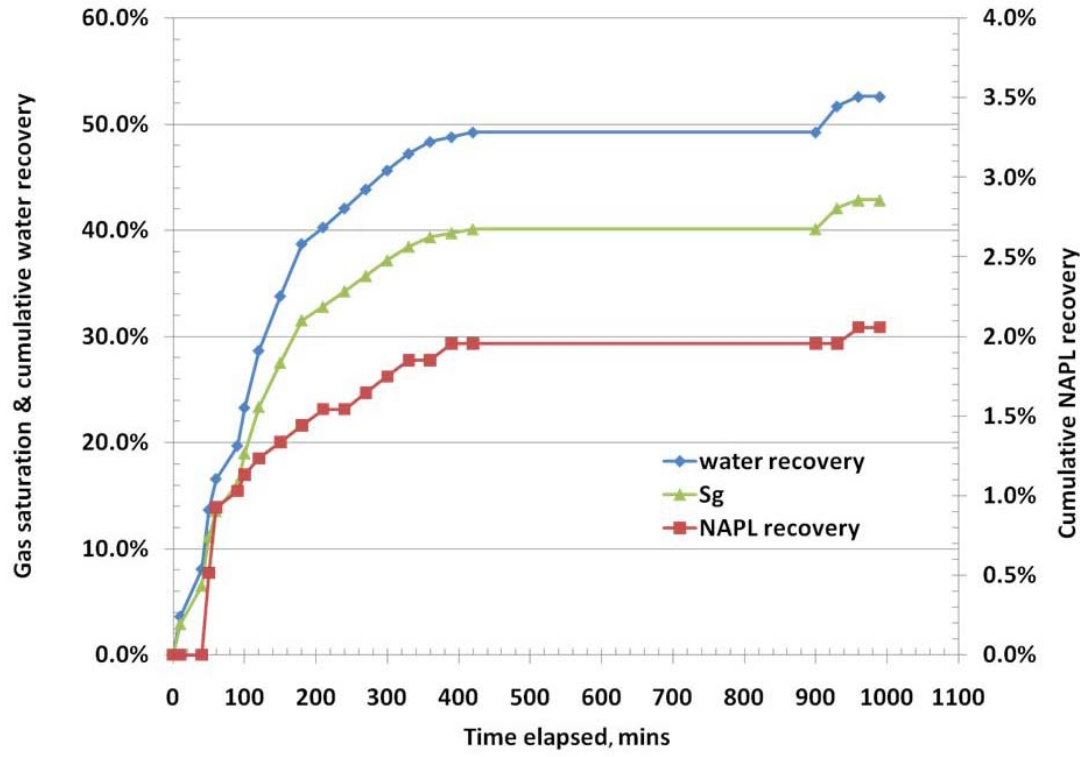

Figure 3. 7 Saturations of gas and water, NAPL recovery vs. time elapsed during 1st gas sparging in No.3

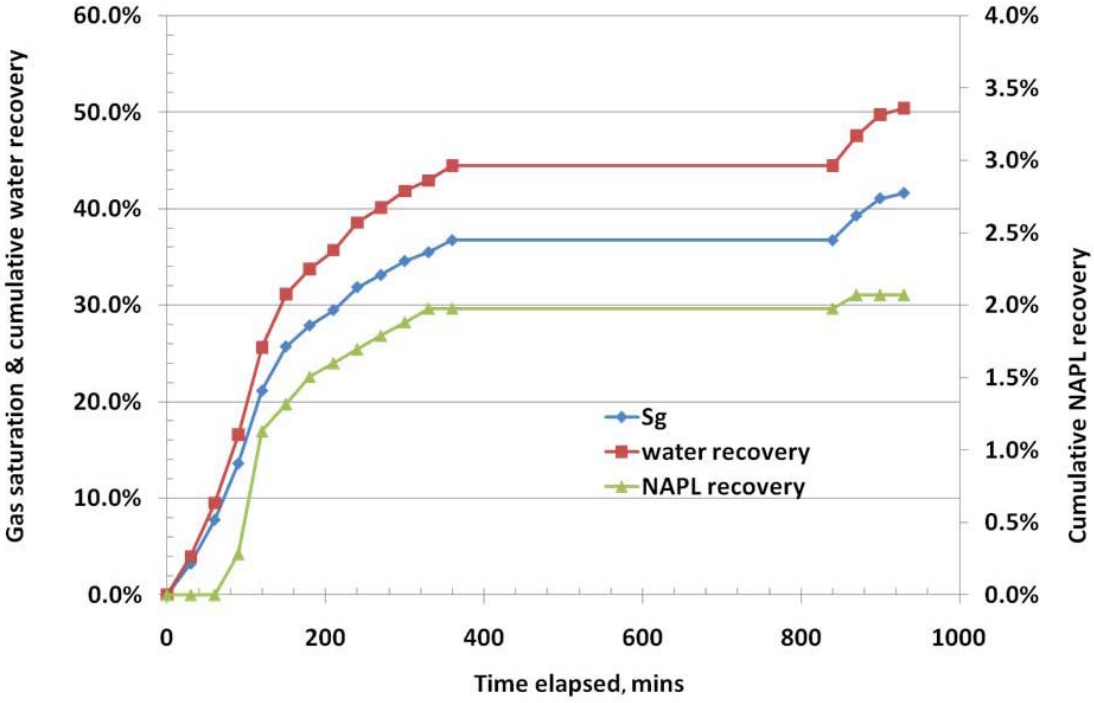

Figure 3. 8 Saturations of gas and recoveries of water, NAPL vs. time elapsed during 1st gas sparging in No.4

The NAPL recoveries from the different runs in experiments No.3 and 4 are summarized in Tables 3.3 and 3.4. The data in the tables indicate that the recoveries decreased as the NAPL residual saturations decreased. When the 1st gas sparging ended, the NAPL residual saturations were 18.8% and 17.9%, 16.5 ml and 18.5 ml of NAPL, or 37.8% and 45.1% of the total recoveries were obtained in the forms of NAPL layer and by the 2nd gas sparging operations in experiment No.3 and 4 respectively. After the 2nd gas sparging operations, the residual NAPL saturations became 15.8% and 14.5%; 14.8 ml and 14.1 ml of NAPL, or 33.9% and 34.4% of the total recoveries were obtained in the same way. During the last runs, when the NAPL saturations decreased to around 11%, no NAPL was recovered in the form of NAPL layer. The data also indicate that most of the NAPL was recovered in the forms of NAPL layer, implying that significant reconnection of isolated NAPL clusters happened during the processes of gas de-saturation after gas sparging stopped, resulting in the NAPL cluster sizes sufficiently large that the reconnected clusters could be moved upward under the action of buoyancy and be recovered in the form of NAPL layers. 72.5% and 70% of total NAPL recoveries were came in the form of NAPL layers in experiments No.3 and No.4, respectively. Finally the data indicate that, although the columns were sparged by air and CO2 separately, the recovery behaviors were very similar. The final NAPL recoveries were 41.1% and 40.9% for experiments No.3 and 4, respectively.

Table 3. 3 NAPL recoveries from different runs in No.3

Run series.	1st	2nd	3th	4th	5th	Sum	Wt,%
V, ml, in layers	0.0	12.4	12.3	6.8	0.1	31.6	72.5
V, ml, by sparging	2.1	4.1	2.5	1.8	1.5	12	27.5
Sum, ml	2.1	16.5	14.8	8.6	1.6	43.6	100.0
Weight,%	4.8	37.8	33.9	19.7	3.7	100.0	
Residual saturation	18.8%	15.8%	13.2%	11.6%	11.3%		
Cumulative recovery	2.0%	17.5%	31.5%	39.5%	41.1%		

Table 3. 4 NAPL recoveries from different runs in No.4

Run series.	1st	2nd	3th	4th	5th	Sum	Wt,%
V, ml, in layers	0.0	15.0	10.8	2.8	0.1	28.7	70.0
V, ml by sparging	2.2	3.5	3.3	2.0	1.3	12.3	30.0
V Sum, ml	2.2	18.5	14.1	4.8	1.4	41.0	100.0
Weight,%	5.4	45.1	34.4	11.7	3.4	100.0	
Residual saturation	17.9%	14.5%	11.9%	11.0%	10.8%		
Cumulative recovery	2.2%	20.7%	34.7%	39.5%	40.9%		

The NAPL residual saturation vs. gas saturation at different times in experiments No.3 and No.4 are plotted in Figure 3.9 and Figure 3.10. The two experimental results were very similar, except for the residual gas saturations in air sparging column were around 3% higher than that in CO_2 sparging column after the overnight standings, which might be caused by convective mass transfer of the dissolved CO_2. Because in experiment No.3 the instantaneous gas saturations after sparging stopped were not measured, the results of experiment No.4 are discussed here below.

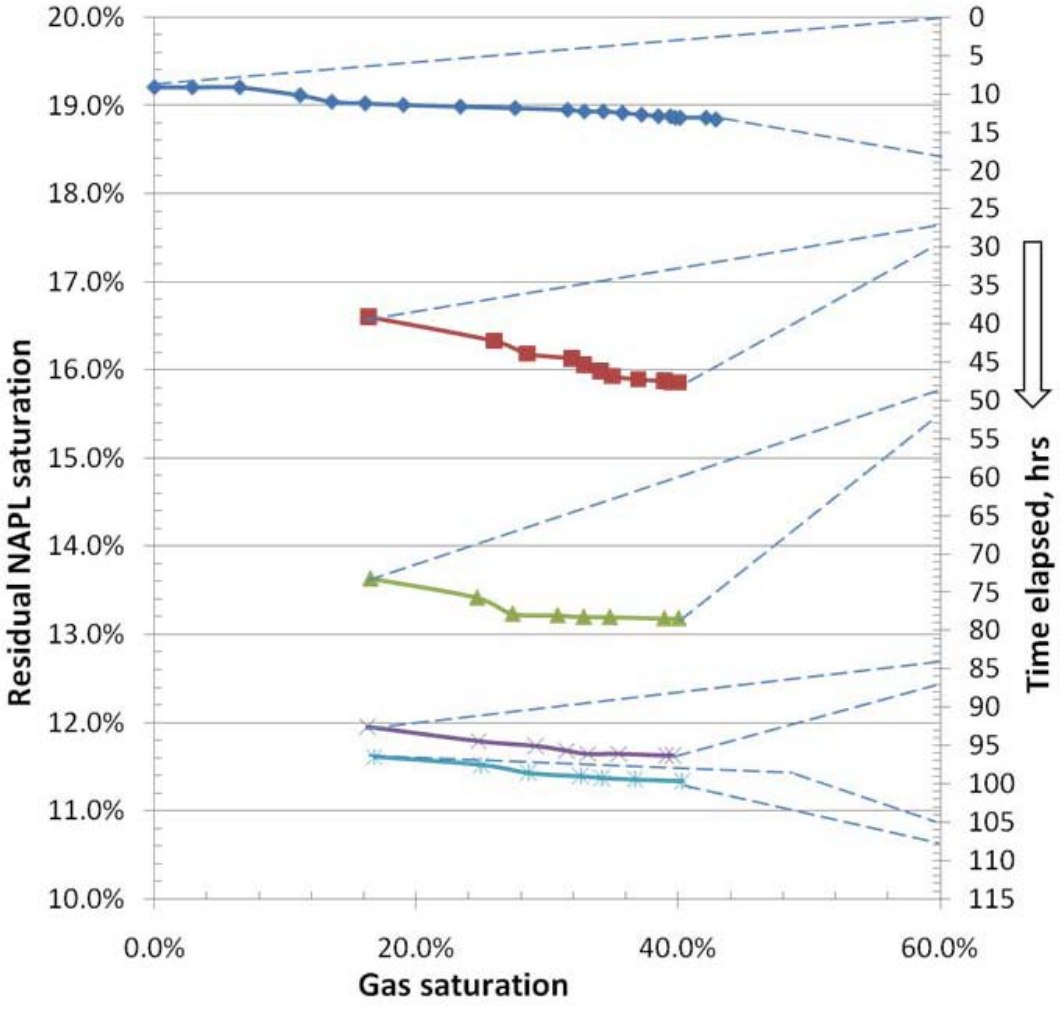

Figure 3. 9 NAPL residual saturation vs. gas saturation at corresponding time in experiment No.3

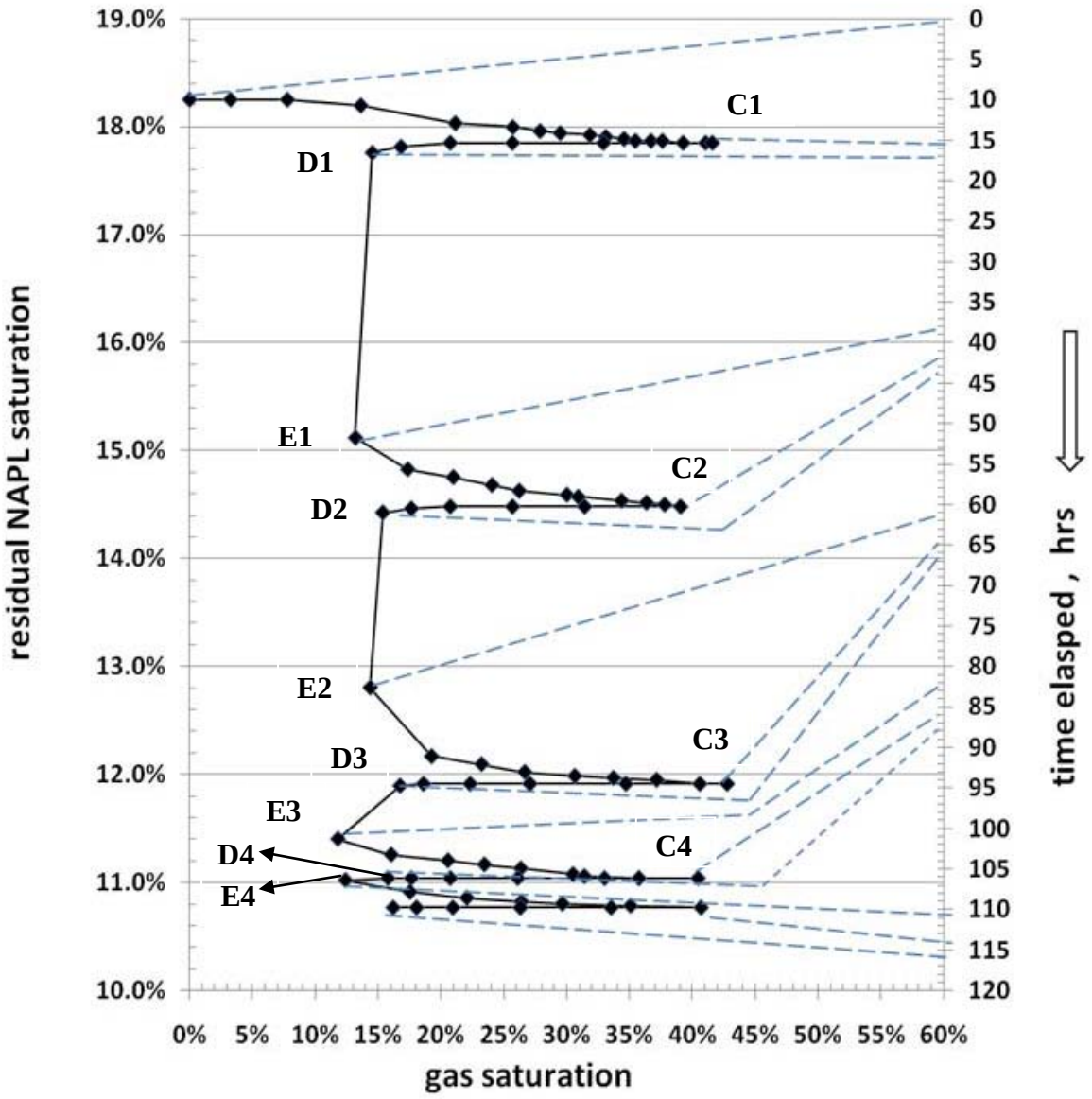

Figure 3. 10 NAPL residual saturation vs. gas saturation at corresponding time in experiment No.4

Shown in Table 3.5 are the data of saturation and saturation change at different times corresponding to the points in Figure 3.10. After the gas injections ceased, around 25% of gas saturation decrease happened from point C_i to D_i in 90 minutes, however the NAPL recovered during this period was negligible. Significant NAPL was recovered in the form of free NAPL layer from point D_i to E_i, while the gas saturation decreased very little. For

example, during 22 hours of standing time from point D_1 to E_1, 18.5 ml NAPL was recovered in the form of free NAPL layer; the NAPL saturation and gas saturation decreased by 2.64% and 2.41% respectively, accordingly the water saturation increased by 5.05%. Although most of NAPL was recovered during this period, the majority of the NAPL cluster reconnection might have happened during the process of gas de-saturation from C_1 to D_1 after stopping gas injection, as rather long time is required for the reconnected NAPL clusters to slowly move up to the top of the column under the action of buoyancy.

Table 3. 5 Saturation changes at different time corresponding to the points in Figure 3.10

t, the hr.	Point	S_g	S_{rn}	Δt ,hr	ΔS_g	ΔS_{rn}
15.5	C1	41.59%	17.85%	n/a	n/a	n/a
17	D1	15.61%	17.76%	1.5	-25.98%	-0.09%
39	E1	13.20%	15.12%	22	-2.41%	-2.64%
42.5	C2	39.06%	14.48%	3.5	25.86%	-0.64%
44	D2	15.37%	14.43%	1.5	-23.69%	-0.05%
61	E2	13.17%	12.81%	17	-2.20%	-1.62%
64	C3	42.76%	11.91%	3	29.59%	-0.90%
65.5	D3	16.74%	11.89%	1.5	-26.02%	-0.02%
83	E3	11.80%	11.40%	17.5	-4.94%	-0.49%
86.5	C4	40.45%	11.04%	3.5	28.65%	-0.36%
88	D4	15.78%	11.04%	1.5	-24.67%	0.00%
111	E4	12.40%	11.02%	23	-3.38%	-0.02%

3.3.3 Dimensionless Group Number Analysis

The capillary number is commonly used to measure the relative strength of viscous forces to capillary forces and assess the potential for entrapped NAPL blob mobilization in porous media. In immiscible displacement, the capillary number might be calculated by different expressions. If it is calculated from Darcy velocity, and takes into account of the porosity of the porous medium and the fluid saturation, the capillary number, N_{Ca1}, can be calculated by the following equation:

$$N_{Ca1} = \frac{v\mu}{\Phi S\sigma} \quad \text{---------- Equation 3.11}$$

where, μ is the viscosity of the displacing fluid, σ is the interfacial tension between the fluids, v is the Darcy velocity of the displacing fluid, Φ is the porosity of the porous medium, and S is the fluid saturation.

In experiment No.1, water and gas are flowing through the porous medium simultaneously, exerting shear stresses on the entrapped residual NAPL. Thus it might be reasonable to use the sum of capillary numbers of water and gas to represent the capillary number for our case. The capillary number may also be calculated from the pressure gradient over the porous medium by incorporating the absolute permeability (Morrow et al., 1982; Zhou et al., 1993):

$$N_{Ca2} = \frac{k\Delta p}{\sigma_{nw} L} \quad \text{---------- Equation 3.12}$$

where N_{Ca2}, k, $\Delta p / L$, and σ_{nw} are the capillary number, absolute permeability, pressure gradient in the invading phase, and interfacial tension between water and NAPL.

Another relevant dimensionless group number is Bond number, N_B, which is calculated by:

$$N_{Bo} = \frac{\Delta\rho g k}{\sigma}$$ ----------Equation 3.13

where $\Delta\rho$ is the density difference between the two immiscible fluids, g is the gravitational constant, k is absolute permeability. Pennell at el. (1996) derived a total trapping number to quantify the potential for mobilization of the entrapped residual NAPL. In our case, the directions of viscous and buoyancy forces are same, thus the total trapping number can be expressed as follows:

$$N_T = \left| N_{Ca} + N_{Bo} \right|$$ ---------- Equation 3.14

Tables 3.6 and 3.7 list the results of capillary numbers calculated by different expressions in experiments No. 1 and 2. Experiment No. 2 was carried out under water flooding operations at flow rates from 3 to 75 ml/min.

Table 3. 6 Capillary numbers, N_B, and N_T in experiment No.1 (co-injection)

	Water flooding	Co-injection of water and gas				SWI
Q_w, ml/min	3.1	2.9	10.22	20.05	29.87	31.6
Q_g, ml/min	0	83.1	80.6	78.9	81.2	79.5
S_{rn}	15.7%	9.1%	8.2%	7.80%	7.7%	7.0%
S_g	0.0%	32.5%	29.1%	27.2%	25.6%	25.1%
S_w	84.3%	58.4%	62.7%	65.0%	66.7%	67.9%
p, psig, bottom	3.01	6.18	9.12	12.63	16.31	16.39
$N_B \times 10^{-6}$	2.21	2.21	2.21	2.21	2.21	2.21
$N_{Ca1} \times 10^{-6}$	5.86	10.9	29.2	52.5	75.1	77.9
$N_{Ca2} \times 10^{-6}$	4.86	22.4	38.6	58.0	78.3	78.8
$N_T \times 10^{-6}$	8.07	13.1	31.4	54.7	77.3	80.1

Table 3. 7 Capillary Number in experiment No.2 (water flooding)

Q_w, ml/min	3.10	10.31	18.53	29.04	36.23	62.57	75.28
S_{rn}	17.6%	16.4%	16.3%	16.3%	16.1%	16.1%	15.9%
S_w	82.4%	83.6%	83.7%	83.7%	83.9%	83.9%	84.1%
p, psig, bottom.	3.06	4.67	6.71	8.43	10.15	15.11	17.65
$N_{Ca1} \times 10^{-6}$	6.06	19.8	35.7	55.9	69.6	120	144
$N_{Ca2} \times 10^{-6}$	6.24	17.0	30.7	42.3	53.8	87.1	104

Figures 3.11 and 3.12 are the plots of capillary number vs. water flow rate. The results show that N_{Ca1} and N_{Ca2}, are very close. In experiment No.2, N_{Ca1} is greater than N_{Ca2} and the difference between N_{Ca1} and N_{Ca2} becomes greater as the water flow rate increases. However, in experiment No.1, N_{Ca1} is smaller than N_{Ca2} and the difference between N_{Ca1} and N_{Ca2} becomes smaller as the water flow rate increases. The possible reason might be that the interfacial tension used in N_{Ca2} calculation is the interfacial tension between water and NAPL, σ_{nw}. For experiment No.1, both water and gas flows contribute to the pressure drop over the porous medium, thus it does not make sense to just take into account the interfacial tension of between water and NAPL, σ_{nw}, only. It might be reasonable if a weighted average interfacial tension of σ_{nw} and σ_{ng} is used to the calculation, which could represent the relative contribution of pressure drop from gas and water flows: at lower water flow rate, the contribution of gas to the pressure drop over the porous medium would be greater than that at higher water flow rate. The Bond number is 2.21×10^{-6} for experiment No.1. Comparatively speaking, at high flow rate displacement condition, it is pretty small.

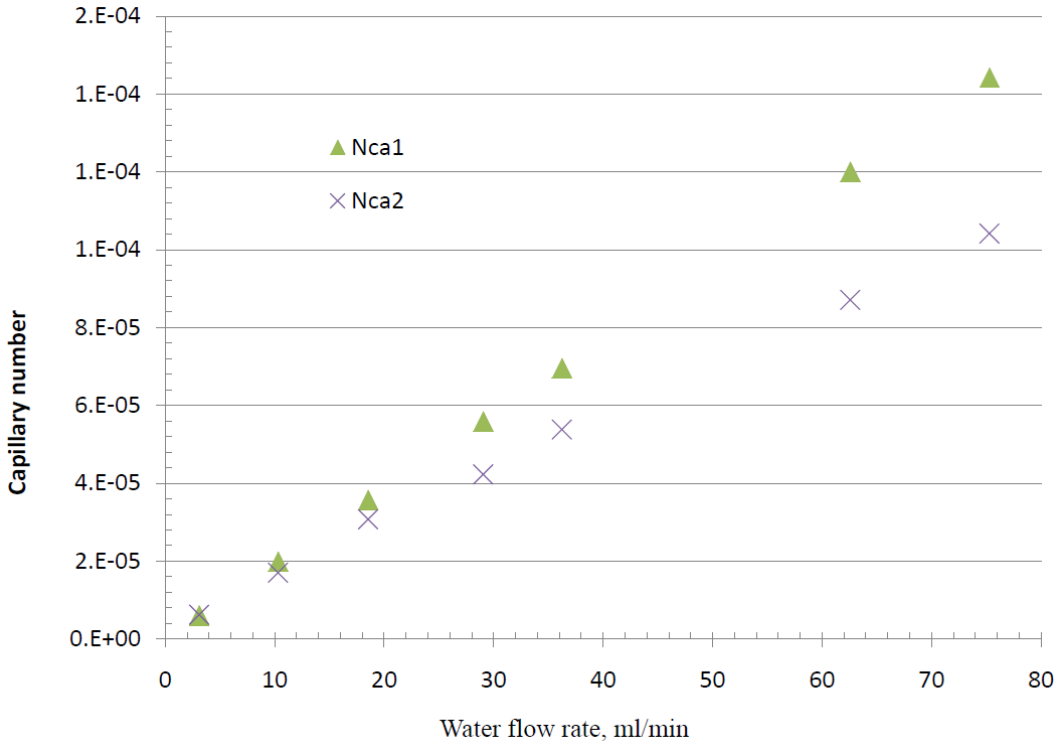

Figure 3. 11 Plots of capillary number vs. water flow rate in experiment No. 2

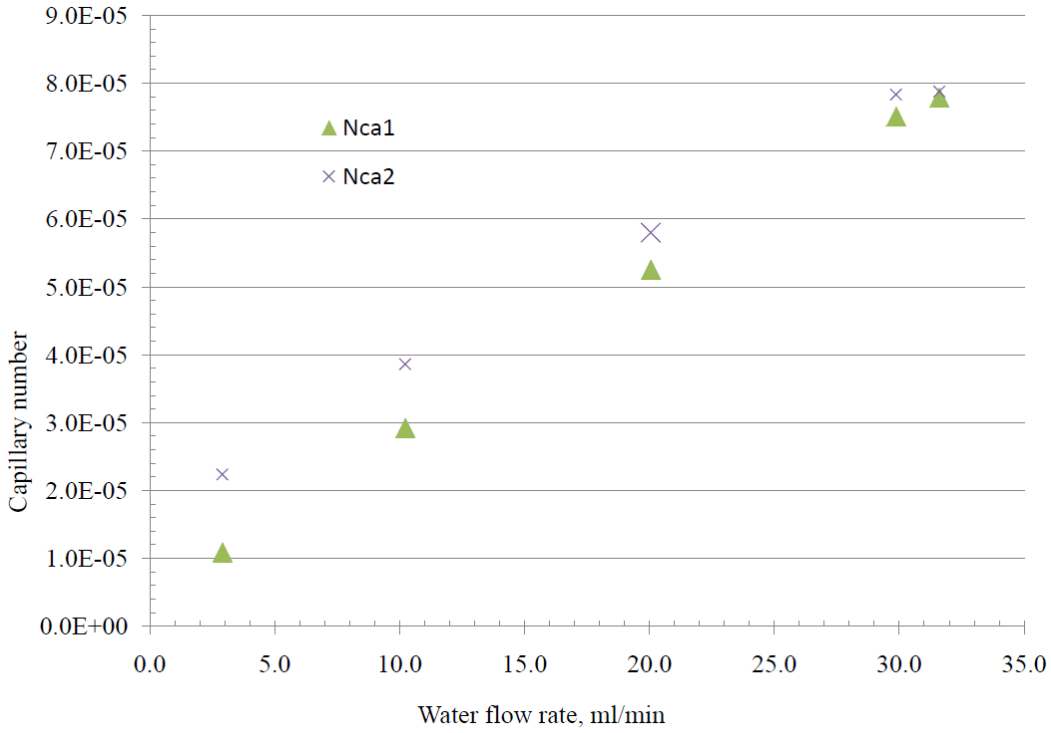

Figure 3. 12 Plots of capillary number vs. water flow rate in experiment No. 1

Figure 3.13 is the plot of residual NAPL saturation vs. capillary number, N_{Ca1}, for experiment No1 and No.2 respectively. In experiment No.2, which was carried out under water flooding conditions, as the capillary number, N_{Ca1}, increased from 6.06E-6 to 1.44E-4, the saturation decreased from only 17.6% to 15.9%, indicating that hardly any of initial residual NAPL could be removed. In water-gas co-injection experiment, No.1, the highest value of N_{Ca1} was only 7.79E-05, at which the entrapped residual NAPL clusters should not have been mobilized based on the result of experiment No.2. However, the displacement under only N_{Ca1} =1.09E-05 (co-injection at 3 ml/min water flow rate) caused significant mobilization of entrapped residual NAPL clusters. In the experiment No.1, there were two instances when the residual NAPL saturations decreased significantly while capillary numbers changed very little. In the first instance, the capillary number, N_{Ca1}, increased from 4.94E-6 (water flooding condition) to 1.09E-5 (co-injection at 3 ml/min water flow rate), the residual NAPL saturation decreased from 15.7% to 9.1%. In the second instance, when the capillary number increased from 5.86E-6 (co-injection) to 7.79E-05 (SWI), the residual NAPL saturation decreased from 7.7% to 7.0%.

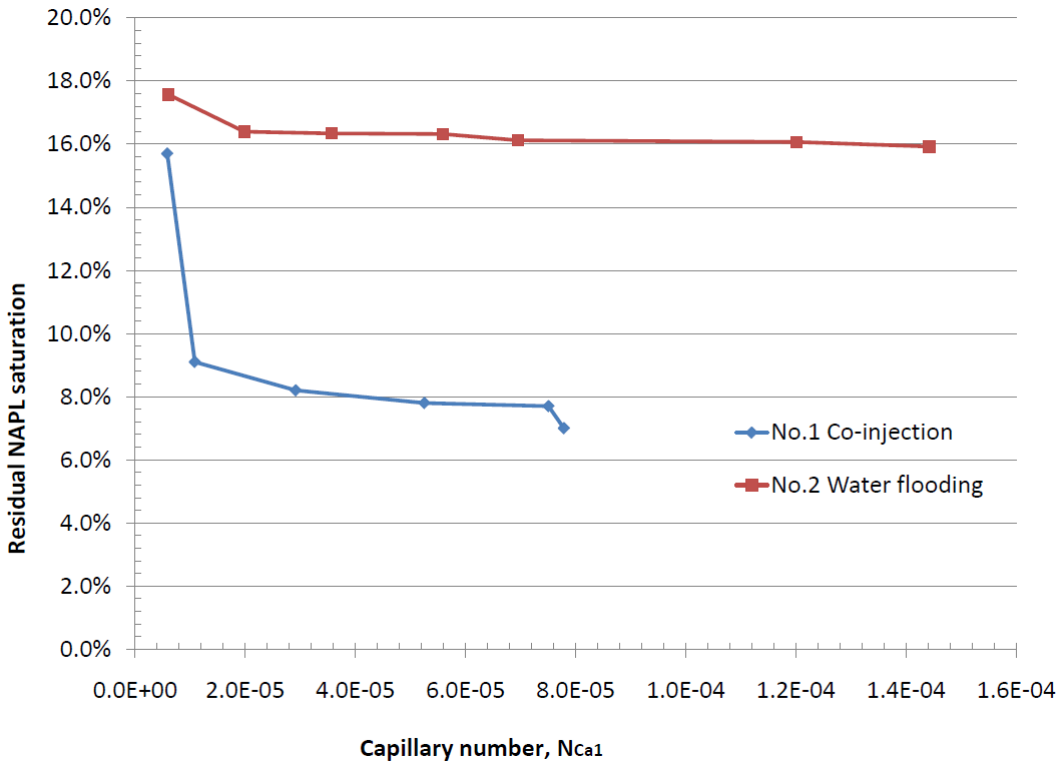

Figure 3. 13 Correlations between residual NAPL saturation and capillary number, N_{Ca1}, for experiments No.1 and 2

The mobilization of entrapped residual NAPL blobs in the saturated porous medium is caused by either increasing the viscous forces exerted by the displacing fluid flow or the increase in the blob sizes which results in a decrease of the viscous forces needed to mobilize the blob and increase of buoyancy influence. From the above results, it seems that the reason for the mobilization of the entrapped residual NAPLs is likely not the increase of capillary number in experiment No.1, because the value of capillary numbers in experiment No.1 were much smaller than that in experiment No.2, when water flow rate was 75 ml/min at which no significant mobilization happened. The major reason might be the redistribution of isolated residual NAPL clusters, caused by reconnection due to gas-water co-injection, increasing the size of the NAPL clusters. The increase of the NAPL cluster size not only decreased the value of viscous forces required to mobilize the NAPL clusters, but also increased the

influence of the buoyancy on the mobilization of NAPL clusters.

Ng et al. (1978) have shown that the capillary number required to mobilize a blob is inversely proportional to blob length in the direction of Darcy-law pressure gradient. To mobilize an entrapped residual NAPL cluster with a certain size in the saturated porous media, a minimum value of capillary number has to be applied. This minimum value of capillary number is referred to as critical capillary number, N_{CC} . Amili et al. (2006) simulated the dependence of critical capillary number for mobilization of a random ganglion as a function of the ganglion size, as shown in Figure 3.14. Based on the balance of forces on a NAPL blob, Mayer et al. (1992, 1993) derived the relations between the maximum stable height of a NAPL blob and the capillary and Bond numbers.

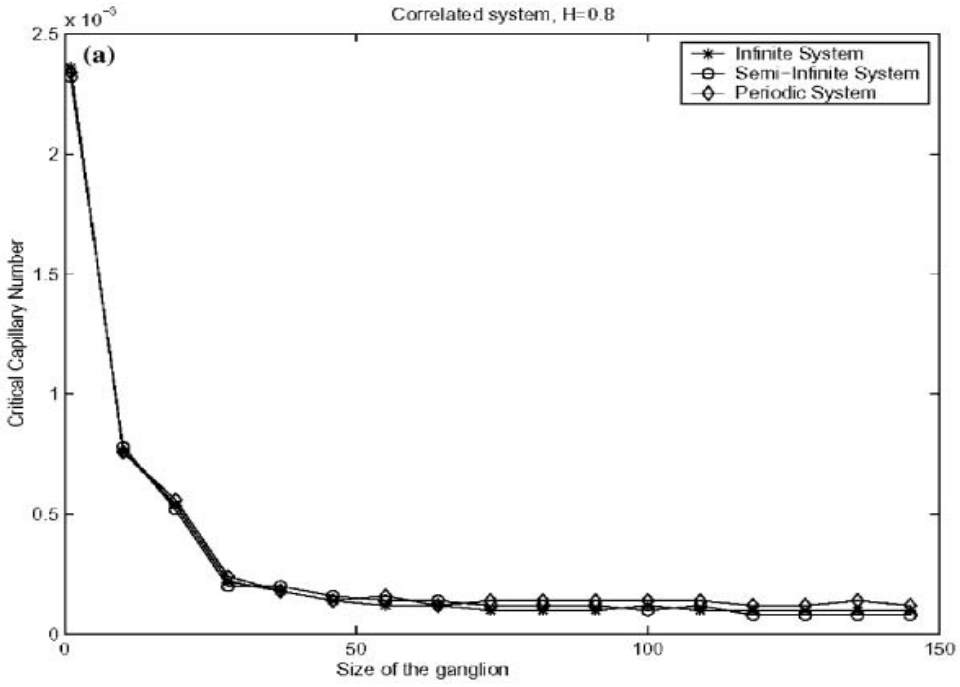

Figure 3. 14 The dependence of critical capillary number for mobilization of a random ganglion as a function of the ganglion size ($n \times n$) (Amili et al., 2006)

From the derivation of Pennell at el. (1996), in the case of co-linear gravitational and viscous forces, the following relationship is obtained:

$$(\frac{\Delta P}{L} + \rho_w g)l - \rho_n g l = \frac{2\sigma_{nw}\cos\theta}{r_t}(1 - \frac{r_t}{r_b}) \text{ ---------- Equation 3.15 a}$$

or, $$(\frac{\Delta P}{L} + (\rho_w - \rho_n)g)l = \frac{2\beta\sigma_{nw}\cos\theta}{r_t}(1 - \frac{r_t}{r_b}) \text{ ---------- Equation 3.15 b}$$

where ΔP is the pressure drop caused by fluid flows over the porous medium, L is the length of the porous medium, l is the length of the NAPL cluster, σ_{nw} is the interfacial tension of NAPL and water, θ is the contact angle of water, r_t and r_b are the radii of pore throat and pore body, ρ_n and ρ_w are the density of NAPL and water, respectively. The physical meaning of Equation 17b is that the sum of viscous and gravitational forces must be equal to the net capillary forces at the onset of mobilization. Rewriting Equation 3.17b yields:

$$l = \frac{2\sigma_{nw}\cos\theta}{(\frac{\Delta P}{L} + \rho_w g - \rho_n g)r_t}(1 - \frac{r_t}{r_b}) \text{ ---------- Equation 3.15 c}$$

From Equation 3.17 c, the minimum length of NAPL cluster to be moved under the given pressure gradient applied over the porous medium can be calculated. In this calculation, it was assumed that the aspect ratio, r_t / r_b equals 0.5 (Brooks et al., 1999), r_t is equal to 0.25 times of the particle diameter (Mayer et al., 1993). The results for different contact angles, θ, i.e.,0^o, 30^o, and 60^o, and buoyancy was neglected, are shown in Tables 3.8 and 3.9 for experiments No.1 and 2, respectively.

Table 3. 8 Minimum length of cluster to move at various N_{Ca1} and θ for experiment No.1

	ID.	θ	Length of NAPL cluster, cm				
Buoyancy considered	No.1-1	0°	1.586	0.955	0.648	0.484	0.481
	No.1-2	30°	1.374	0.827	0.561	0.419	0.417
	No.1-3	60°	0.794	0.478	0.324	0.242	0.241
Buoyancy neglected	No.1-1A	0°	1.743	1.010	0.672	0.498	0.495
	No.1-2A	30°	1.509	0.875	0.582	0.431	0.429
	No.1-3A	60°	0.872	0.505	0.336	0.249	0.248
$N_{Ca1}\times10^{-6}$			10.9	29.2	52.5	75.1	77.9

Table 3. 9 Minimum length of cluster to move at various N_{Ca1} and θ for experiment No.2

	ID.	θ	Length of NAPL cluster, cm						
Buoyancy considered	No.2-1	0°	5.009	2.265	1.337	0.994	0.791	0.498	0.418
	No.2-2	30°	4.338	1.962	1.158	0.861	0.685	0.431	0.362
	No.2-3	60°	2.507	1.134	0.669	0.497	0.396	0.249	0.209
Buoyancy neglected	No.2-1A	0°	7.161	2.622	1.454	1.057	0.830	0.513	0.429
	No.2-2A	30°	6.202	2.271	1.259	0.916	0.719	0.444	0.372
	No.2-3A	60°	3.584	1.312	0.728	0.529	0.416	0.257	0.215
$N_{Ca1}\times10^{-6}$			6.06	19.8	35.7	55.9	69.6	120	144

Figure 3.15 is the correlation of the capillary number N_{Ca1} and the minimum cluster length calculated under various arbitrary contact angles, 0^o, 30^o, and 60^o. It is obvious that the contact angle significantly affected the values of the minimum cluster length, and the degree of the influence became greater as the capillary number became smaller, as expected since wettability and contact angle hysteresis were of significant importance to the behavior of immiscible displacement.

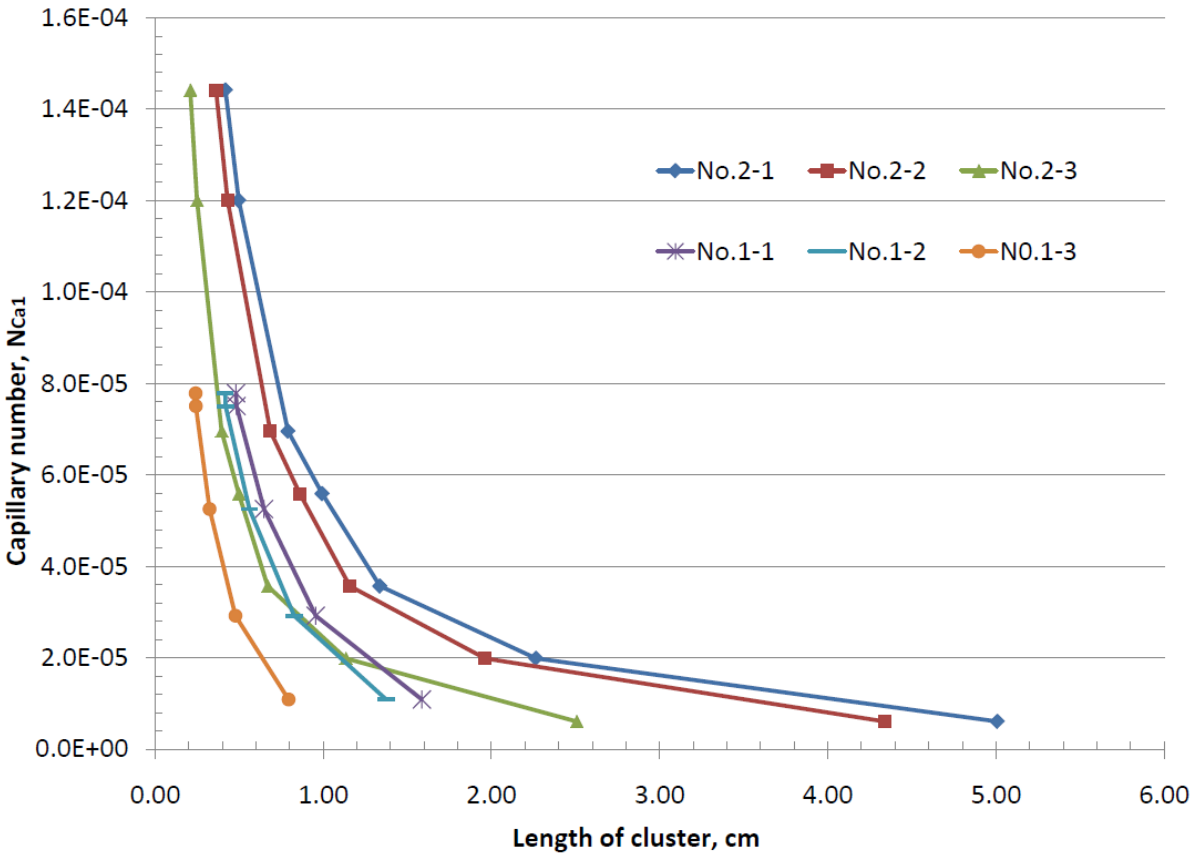

Figure 3. 15 Correlation between the capillary number N_{Ca1} and the minimum cluster length to be mobilized under various arbitrary contact angles in experiments No.1 and 2

Plotted in Figure 3.16 is the calculated result at 0^o contact angle when the buoyancy was neglected. The curves in the figure show that the influence of buoyancy increased as the capillary number decreased. The buoyancy could not be neglected at the low capillary

number displacement conditions or when the size of entrapped NAPL clusters was large enough.

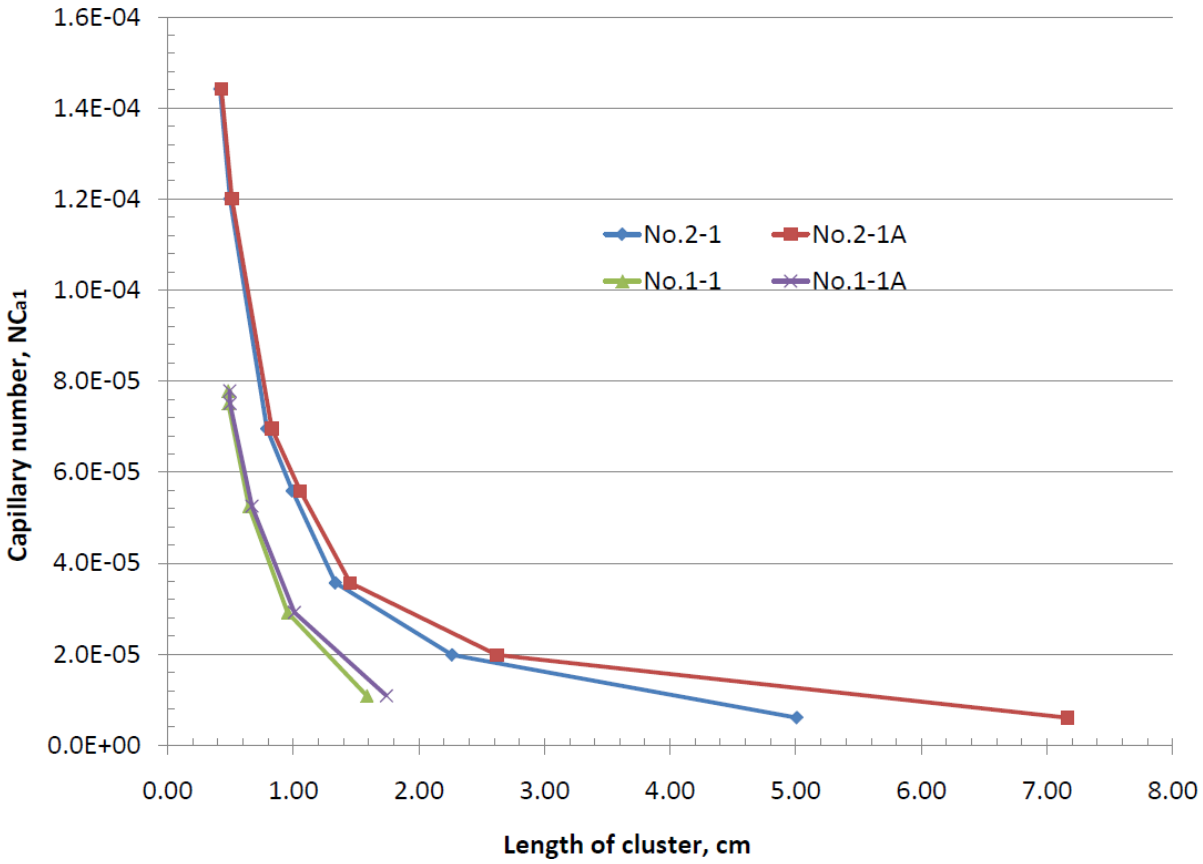

Figure 3. 16 Correlation between the capillary number N_{Ca1} and the minimum cluster length to be mobilized when the buoyancy was neglected in experiment No.1 and 2

In Figure 3.17, curve No.2-1 is the relationship between the capillary number and the minimum cluster length to be mobilized in experiment No.2 under water flooding conditions. The minimum cluster lengths to be mobilized at the lowest capillary number (6.06E-06) and the highest capillary number (1.44E-04) were 5.009 and 0.418 cm, respectively. The results of experiment No.2 showed that no significant NAPL mobilization had occurred at a capillary number of 1.44E-04, indicating the majority of the NAPL clusters after water flooding should be of a length less than 0.418 cm. From curve No1-1, we could know that, at

the lowest capillary number (1.09E-05) under co-injection condition, the minimum cluster length to be mobilized was 1.586 cm. This meant that, only if the NAPL cluster had a length more than 1.586 cm, could it be possible to be mobilized under the displacement condition with this capillary number. The fact that significant entrapped residual NAPL was recovered under this co-injection displacement condition demonstrated that the reconnection of entrapped residual NAPL clusters did have happened, and increased the length of NAPL from less than 0.418 cm to more than 1.586 cm under the above displacement condition; or there should not have been any NAPL recovery.

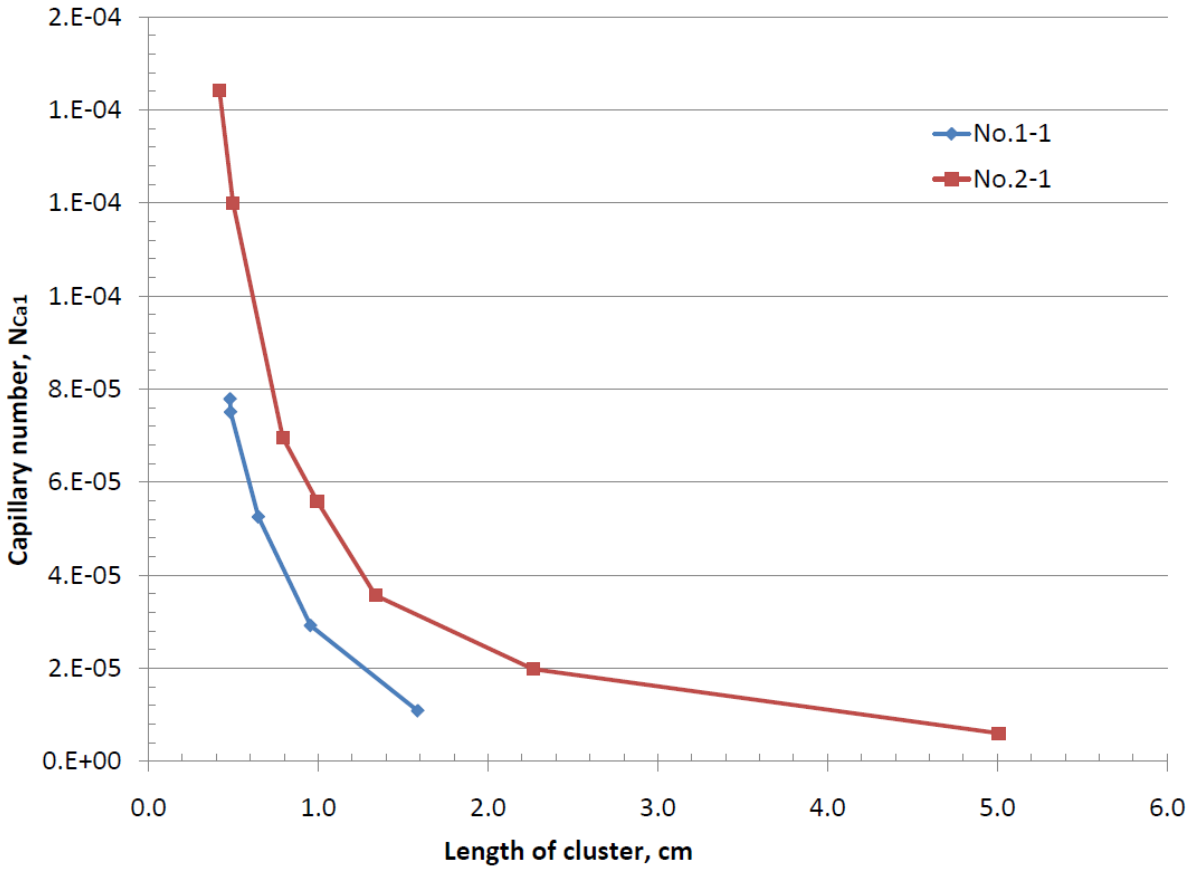

Figure 3. 17 Comparison of the relationship of the capillary number N_{Ca1} and the minimum cluster length to be mobilized under 0^{o} contact angle between experiments No.1 and 2

3.3.4 Pore-scale Displacement Mechanisms

It is instructive to consider the pore-scale three-phase displacement mechanism consistent with the experimental observations. After water flooding, the NAPL is entrapped in the saturated porous media in the form of ganglia occupying one, two or several pores. In order to simplify the situation, we may consider a singlet ganglion as an example to illustrate how isolated NAPL blobs might become reconnected during the process of three phase flow in porous media. The processes should be similar for NAPL clusters.

Figure 3.18A depicts the isolated NAPL blobs in the saturated porous medium after water flooding. Gas has already invaded into pore 2 from the bottom. Which pore adjacent to pore 2 will be invaded by gas next, depends on the pore throat radius, r_{tij}, where i and j are pore numbers. Assuming r_{t25} is the largest, the gas will invade into the throat between pore 2 and 5 due to the smaller capillary pressure. Before the gas contacts a NAPL blob in pore 5, it is actually a single drainage displacement, i.e. the gas displaces the water. Assuming the gas can invade into body of pore 5 to a certain depth, where the radius is $r_{b5d} = xr_{t56}$, and the NAPL blob is still confined in the pore as shown in Figure 3.18B, and if r_{t56} is the largest among the pore throats between pore 5 and the adjacent pores, and r_{t12} is the second large next to r_{t25} among the pore throats between pore 2 and its adjacent pores, now there are two possible displacements happening: One is the double drainage displacement, i.e., the gas displaces the NAPL blob in pore 5 and the NAPL blob in pore 5 displaces the water at the pore throat between pore 5 and 6, then enters pore 6. The other one is a single drainage, i.e., the gas in pore 2 invades into pore 1.

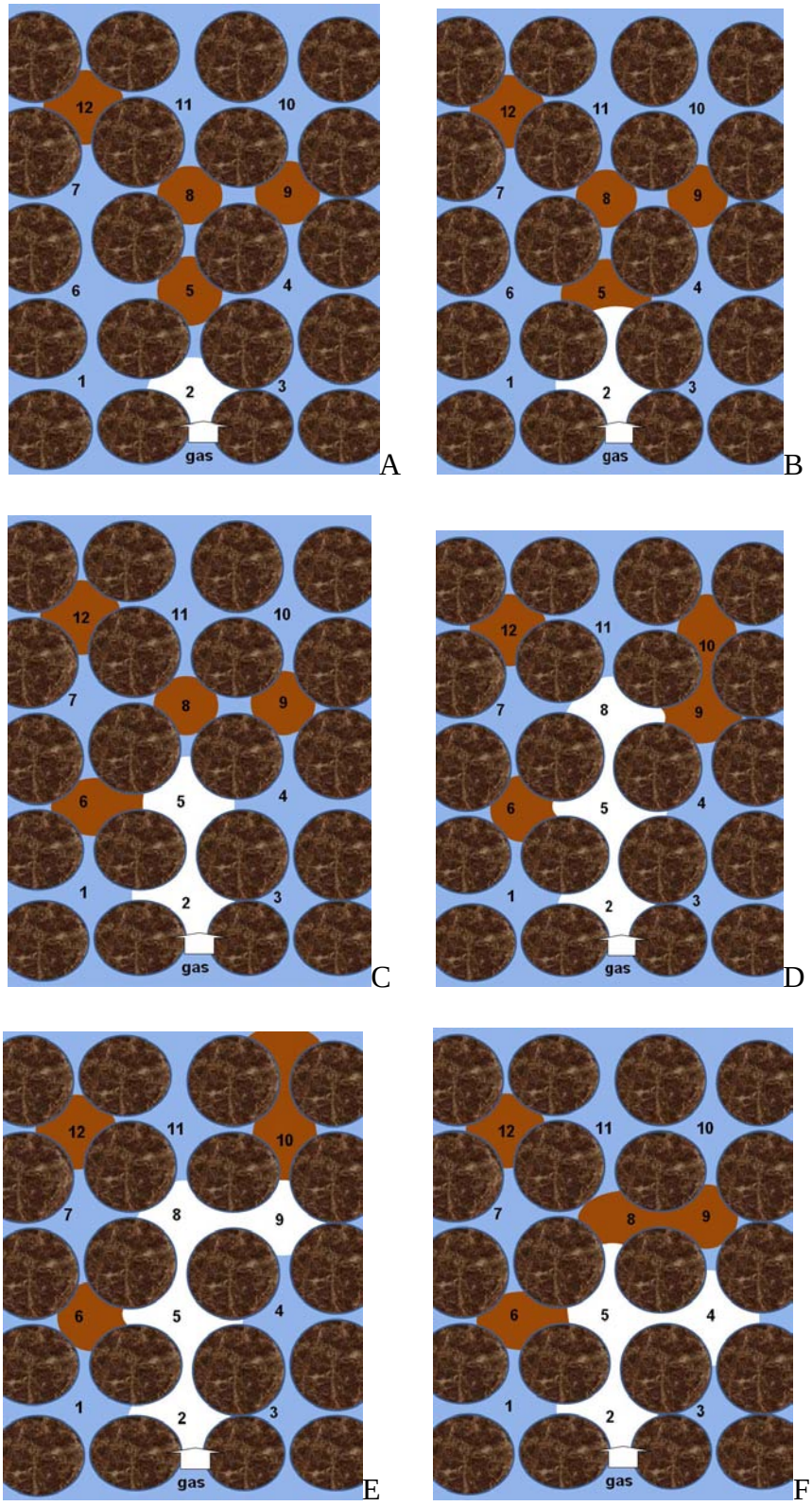

Figure 3. 18 Schematics of the reconnection of residual NAPL blobs during the three-phase flow in the porous medium

The capillary pressures for the double drainage displacement ($p_{C,DD}$) and single drainage ($p_{C,D}$) can be expressed as Equation 3.16 and 3.17:

$$p_{C,DD} = \frac{2\sigma_{nw}\cos\theta_{nw}}{r_{t56}} + \frac{2\sigma_{ng}\cos\theta_{ng}}{xr_{t56}} \text{ ----------Equation 3.16}$$

$$p_{C,D} = \frac{2\sigma_{gw}\cos\theta_{gw}}{r_{t12}} \text{ ----------Equation 3.17}$$

where σ_{nw}, σ_{ng} , and σ_{gw} are interfacial tensions of NAPL and water, NAPL and gas, and gas and water; and θ_{nw} , θ_{ng} , and θ_{gw} are contact angles between the solid wall and the interfaces of NAPL and water, NAPL and gas, and gas and water. Only if $p_{C,DD} < p_{C,D}$, will the double drainage displacement probably happen. Now assume that $r_{t12} = r_{t56} = r_t$, and the sand is completely water wet, i.e., $\theta_{nw} = \theta_{gw} = 0^o$, the double drainage displacement will happen if:

$$x > \frac{\sigma_{ng}\cos\theta_{ng}}{\sigma_{gw} - \sigma_{nw}} \text{ ----------Equation 3.18}$$

In this work, σ_{nw} , σ_{ng} , and σ_{gw} are 53.4, 26.2, and 72.6 dyne/cm, respectively, and $1 \geq \cos\theta_{ng} > 0$. From Equation 3.18, we see that when $r_{b5d} \geq 1.15 r_t$, $p_{C,DD}$ will be less than $p_{C,D}$, meaning that the double drainage displacement may happen. Certainly, $r_{t56} > r_{t12}$ will also favor the double drainage displacement. Thus the NAPL blob will be displaced into pore 6 as shown in Figure 3.18 C. Assuming the capillary pressure at the pore throat of pore 5 and 8 is the least, the gas will invade pore 8 and the double displacements will continue to occur if the condition is favorable. In that case, the isolated NAPL blobs in pore 8 and 9 will

become reconnected and be pushed into pore 9 and 10 as shown in Figure 3.18 D. As the displacement continues that way, more isolated NAPL blobs will be reconnected as shown in Figure 3.18E. If the double drainage displacement cannot happen after the NAPL blobs are reconnected in pore 8 and 9, the gas will invade pore 4.

The above displacement processes depend on the pore structure and the properties of the fluids. The reconnection of the NAPL blobs is affected by population density of the residual NAPL distribution. Generally speaking, higher residual NAPL saturation favors isolated NAPL blob reconnection. During steady gas sparging, because the gas flows through distinct channels in the porous medium in a steady way and does not invade new pores, no reconnection happens, resulting in no recovery in the experiment. In gas-water co-injection experiments however, the water flow will disconnect the gas flow, causing the gas to invade new pores and reconnect the isolated NAPL blobs. Thus NAPL can be continuously recovered during gas-water co-injection. In the case of SWI operation, because the gas saturation is produced in situ, it is able to reach the isolated NAPL blobs (e.g. blob in pore 12 in the figures), which would not be accessed by gas during free gas injection, resulting higher efficiency of NAPL recovery from SWI.

The processes of isolated NAPL blob reconnection during de-saturation after gas sparging is stopped are illustrated in Figure 3.19. Before gas sparging stops, the gas saturation is highest. Assume a gas channel exists in the porous medium as shown in Figure 3.19A. Under the action of buoyancy, the gas cluster will move upward. Assume the gas cluster occupies pores 2, 5, 8, and 11, as shown in Figure 3.19B. When the gas continues moving upward out of pore 5, the pressure in pore 5, p_g, will drop. This will “drag” the liquid, either water or

NAPL, from the adjacent pores through the pore throat with the least capillary pressure to refill this pore. The capillary pressures between gas and NAPL, and between gas and water, can be expressed as:

$$p_g - p_n = \frac{2\sigma_{ng}\cos\theta_{ng}}{r_{t56}}$$ ----------Equation 3.19

$$p_g - p_w = \frac{2\sigma_{ng}\cos\theta_{gw}}{r_{t25}}$$ ----------Equation 3.20

where p_g, p_n, and p_w are the pressure in gas, NAPL and water phases; θ_{ng}, and θ_{gw} are contact angles between the solid wall and the interfaces of NAPL and gas, and gas and water. For a water wet system, NAPL is the intermediate wetting phase, and gas is the non-wetting phase. Usually $p_g - p_n$ is smaller than $p_g - p_w$, thus it is the NAPL, not the water, that will be "dragged" into pore 5, previously occupied by the gas, when the gas leaves, as shown in Figure 3.19C. As the gas cluster continues to move up and leaves pore 8, either the blob in pore 5 or the blob in pore 9 and 10 will refill pore 8. These two NAPL blobs will get reconnected in either case as shown in Figure 3.19D or E. That way, as the gas cluster continues to move up, more NAPL blobs will be reconnected, and move up to the top of the column with the rising gas cluster together.

The minimum length of a cluster of gas or NAPL to move upwards under the action of its own buoyancy can be estimated from Equation 3.15c by assuming viscous pressure gradient is zero and the contact angle is zero. The result indicates that, gas and NAPL clusters greater than 9.7 cm and 17.7 cm, respectively, could be mobilized. In the experiment, the size of gas clusters should be greater than 9.7cm at about 40% of gas saturation in porous medium when the gas sparging ceased. During the gas de-saturation, the size of NAPL clusters might reach

17.7 cm due to the reconnection of NAPL clusters caused by the double displacement. As a matter of fact, for a complex cluster, which consists a gas cluster and a NAPL cluster as shown in Figure 3.19F, the buoyancy forces acting on both gas and NAPL will be in favor of the upward movement. In a word, during the process of de-saturation of gas, it is a buoyancy-driven and capillary-pressure-controlled double imbibition displacement to reconnect the isolated NAPL clusters.

In addition to the above-mentioned mechanisms, the spreading of NAPL across the interface of water and gas in a saturated porous medium might also contribute to the mobilization of entrapped residual NAPL blobs. Visualization micro-model experiments conducted by Dong et al. (1994) demonstrated the spreading of paraffin with a negative spreading coefficient across the gas water interface in porous medium, as shown as in Figure 3.20. Similar spreading is expected of the kerosene in this experiment, which favors the mobilization of entrapped residual NAPL.

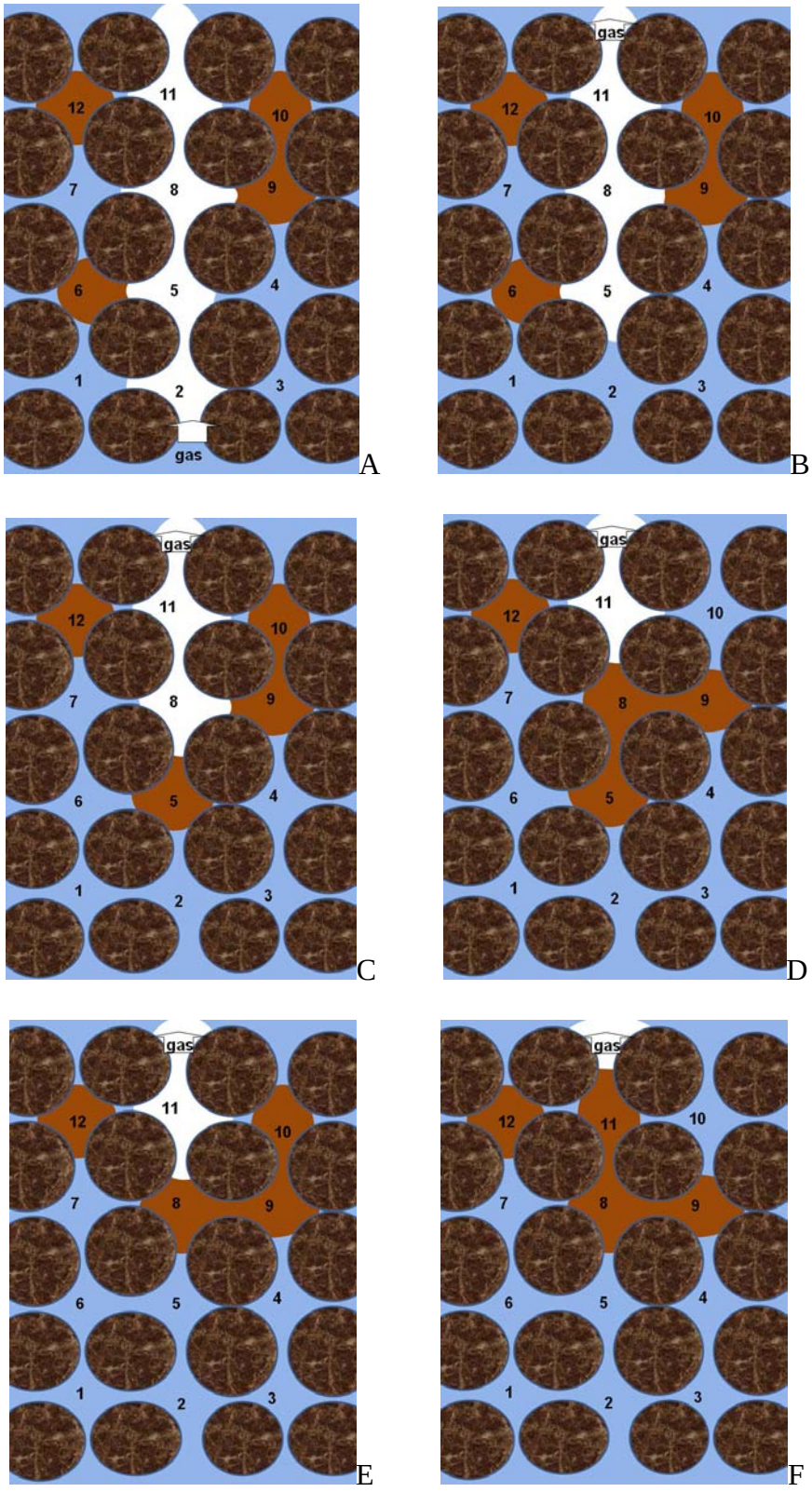

Figure 3. 19 Schematics of the reconnection of residual NAPL blobs during de-saturation of gas in the porous medium.

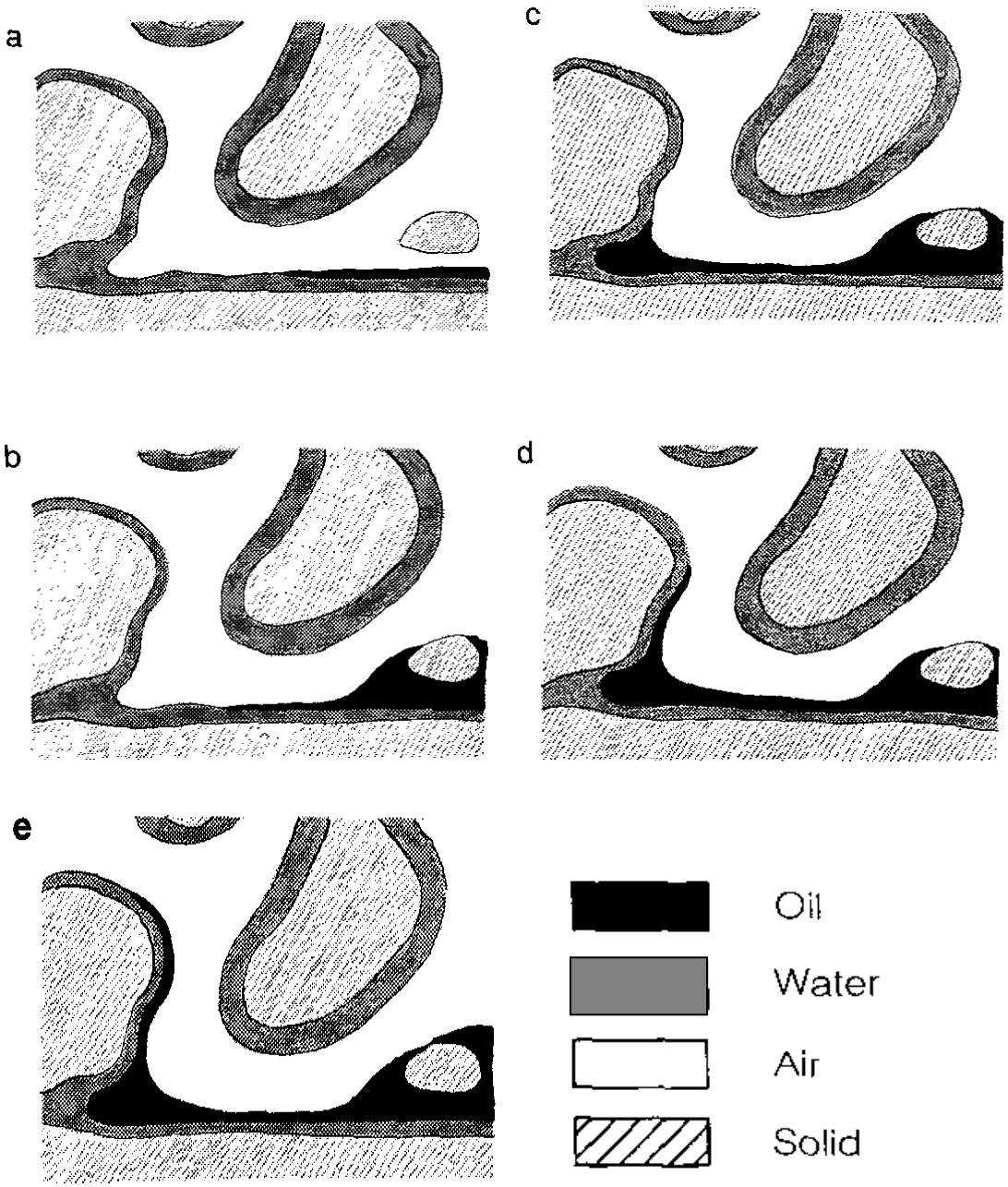

Figure 3. 20 Photomicrographs illustrating imbibition of paraffin oil over a water film in the presence of air. (Dong et al., 1994)

Chapter 4

NAPL Recovery Experiments

by CO_2-Supersaturated Water Injection

4.1 Scope

The recovery of entrapped residual NAPLs in saturated porous media by mobilization mechanisms during supersaturated water injection (SWI) operations is affected by many factors, such as properties of porous media and contaminants etc. A series of column experiments were conducted in this part. The influence of low permeability layers on NAPL recovery behavior was investigated in two sand-packed kerosene columns with low permeability layers set at middle and top respectively. The effect of grains size, different types of contaminants on the recovery performance was studied in homogeneous columns packed with sands of different grain sizes and contaminated with kerosene or a kerosene-hexadecane mixture.

4.2 Experimental Setup and Materials

4.2.1 Experimental Setup

A schematic diagram of the experimental setup is shown in Figure 4.1. A gas cylinder acts as the source of carbon dioxide. Before entering the gPRO^{TM} gas saturator, the gas pressure is adjusted to the required value by a regulating valve. The water for the gPRO^{TM} gas saturator is tap water at a pressure of around 60 psig. The gPRO^{TM} gas saturator is a patented technology (patent No. 6,209,855). A photograph of gPRO^{TM} gas saturator is shown in Figure

4.2. In this technology, hydrophobic hollow fibers are used as a membrane phase contactor, as shown in Figure 4.3, to provide large area for mass transfer between gas and liquid. A self-regulating valve automatically regulates the pressure in gas phase (inside the hollow fibers) at 0.5 to 1 psi below the liquid phase (water) to prevent free gas entering into the liquid phase (outside the hollow fibers). NAPL recovery experiments were conducted in a 150 cm long Plexiglas laboratory column of 38mm inner radius with sampling ports at 5, 75, and 145 cm. Flanges were bolted to the top and bottom of the column with rubber O-rings between them to create a closed system for SWI operations.

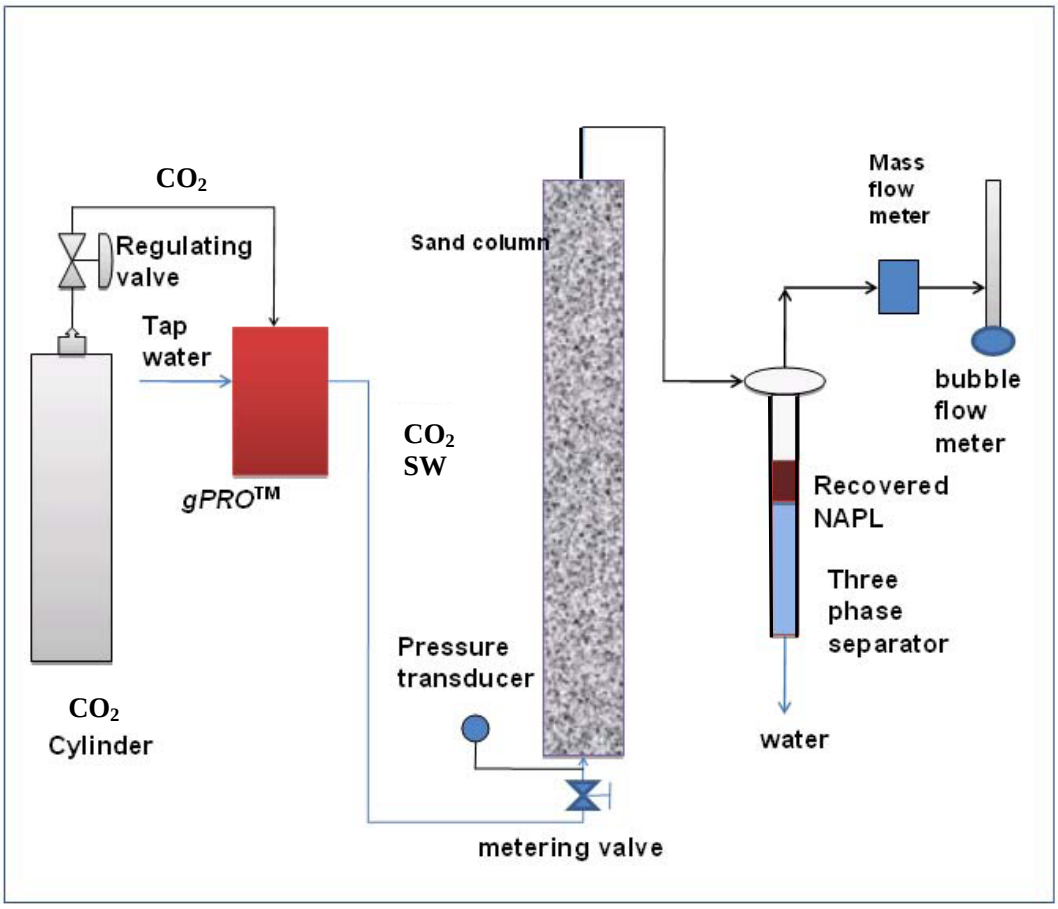

Figure 4. 1 Schematic illustration of experimental setup for SWI recovery

Figure 4. 2 Photograph of gPRO^{TM} generator

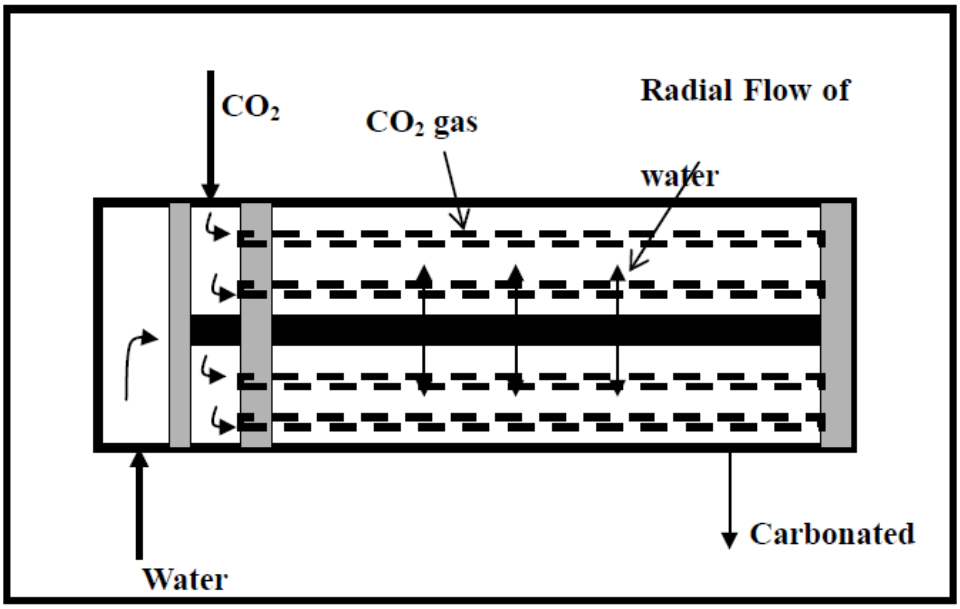

Figure 4. 3 Schematic of gPRO^{TM} gas saturator operation (Li, 2004)

4.2.2 Materials

Sands: Four different silica sands were used in the experiments: Barco 49, Barco 49A, Barco 95, and sieved fine sand (SFS) with average grain sizes of 305.8, 324.1, 168.9, and 96.3 μm respectively. The sieving analyses of the sands are shown in Table 4.1.

Table 4. 1 Results of sand sieving experiments

Sieve opening, μm	Weight of sand retained on the sieve			
	Barco 49*	Barco 49-A*	Barco 95	SFS
595	0	0	0	0
500	2%	3%	0	0
425	13%	13%	0	0
250	48%	58%	5%	0
212	16%	14%	8%	0
180	8%	7%	10%	0
150	7%	2%	45%	0
125	4%	2%	17%	0
106	1%	1%	11%	48.51%
75	1%	0	4%	38.01%
63	0	0	0	5.52%
45	0	0	0	4.24%
0	0	0	0	0
Average grain size, μm	305.8	324.1	168.9	96.3

*Barco 49 &49A are sands with same specification but somewhat different granulometry

Chemicals: Two types of petroleum hydrocarbons, kerosene (Escort^{TR}) and n-hexadecane (Sigma-Aldrich), were used as contaminants in the experiments. The properties of kerosene and hexadecane are shown in Table 4.2.

Table 4. 2 Properties of kerosene and n-hexadecane

	kerosene	n-Hexadecane
Molecular formula	N/a	$C_{16}H_{34}$
Density, g/ml	0.8	0.773
Vapor pressure	0.1 psi	1 mmHg @105.3 ^{o}C
Melt point, °C	-20	18
Viscosity, cp	2	3.24[a]
Aqueous solubility	Insoluble	Insoluble
IFT, air/water, dyne/cm	72.6[b] @20^{o}C	71.8[a]
IFT, NAPL/water, dyne/cm	26.2[b] @20^{o}C	27.0[a]
IFT, air/NAPL, dyne/cm	53.4[b] @20^{o}C	53.3[a]
Cs, dyne/cm	-7.0[b] @20^{o}C	-8.4[a]

a. Keller et al., (2003). b. Heymann, et al., (1942)

4.2.3 Operation Procedures

For column packing and permeability measurements refer to sections 3.2.1 and 3.2.2 in Chapter 3. For establishment of residual NAPL saturation, water-flooding at water flow rate of 3 ml/min was used as detailed in section 3.2.3 in Chapter 3. After the first water flooding, another water-flooding at around a much greater water flow rate was applied to the column. The tap water was directly injected and the flow rate of water injection was controlled at around 20 ml/min by a metering valve. The effluent of the column was introduced into a separator where the water and NAPL were separated. The water-flooding continued until no

more NAPL was recovered. The volume of NAPL displaced (V_{2dn}) and the total weight of the column (M_{ic}) were measured. The volume of NAPL finally remaining in the column (V_{irn}) and the initial residual NAPL saturation (S_{irn}) was calculated as:

$$V_{irn} = V_{rn} - V_{2dn} \text{ ----------Equation 4.1}$$

$$S_{irn} = \frac{V_{irn}}{V_p} \times 100\% \text{ ----------Equation 4.2}$$

Supersaturated Water Injection (SWI) Recovery: The pressure of carbon dioxide was regulated at 80 – 90 psig before the valve connecting tap water and the gPRO^{TM} gas saturator was opened. Following a 1-hr delay, during which CO_2 gas and water were contacted at 60 psig. CO_2-supersaturated water was continuously admitted at the bottom of the column. The injection flow rate was adjusted by the metering valve. The pressure at the bottom of column was measured by a pressure transducer (Validyne, model DP10-44). After the CO_2-supersaturated water entered into the sand-packed column saturated with NAPL, carbon dioxide gas evolved due to the drop of pressure inside the column. The effluent from the top of the column, which contained water, NAPL, and gas, was introduced into a three-phase separator, where the water, recovered NAPL, and gas were separated. The gas phase came out from the top of the separator, and the flow rate of the gas was measured by a mass flow meter (Omega, model FMA 3304) and/or a bubble flow meter. A sample port was set between the mass flow meter and bubble flow meter, which allowed gas samples to be drawn for analysis of NAPL vapor concentration in gas phase. The recovered NAPL was collected in the separator. The rate of NAPL recovery was measured as the rate of volume change of recovered NAPL in the separator over the time. Water flowed out from the bottom of

separator and was measured by either weighing it on a balance or as the volume change of water in the separator over the time when the outlet of the separator was closed. At the conclusion of SWI operation, the total weight of the column (M_c) was measured by a balance. The final residual NAPL saturation (S_{rn}), water saturation (S_w), and gas saturation (S_g) in the column were determined as detailed in section 3.3.5 in Chapter 3. All the SWI operations were conducted intermittently. The injection flow rate began at the lowest level. After the NAPL recovery reaches plateau, the injection flow rate was increased to the next higher level.

4.2.4 GC Analysis of Residual NAPL in Sand after SWI and NAPL Vapor in Gas Phase Stream

Analysis of residual NAPL in sand packs after SWI treatment was carried out by gas chromatography (Agilent 6890A), using a capillary GC column (HP-1 Crosslinked Methyl Siloxane) and a flame ionization detector (FID). An external calibration method was employed for residual NAPL analysis. Calibration samples of different concentrations of NAPL (kerosene or hexadecane) in ethanol were prepared through diluting the standard sample, a completely dissolved mixture of known amounts of NAPL and ethanol, in dichloromethane. The characteristic peaks of the NAPL components were determined and calibration curves were prepared by plotting the characteristic peak heights of the GC analysis against the corresponding concentrations of NAPL and ethanol. At the conclusion of an SWI experiment, the sand pack in the column was separated into 10 to 11 testing samples. Suitable amount of ethanol was added to completely dissolve the residual NAPL in the sand.

Then the testing samples were diluted by dichloromethane and analyzed by GC. By comparing the characteristic peak heights of the testing samples with the calibration curve, the concentrations of the NAPL in the sample were determined. Because kerosene is a very complex mixture with hundreds of components, a peak at 6.125 minutes was chosen as the representative peak for kerosene.

An internal calibration method was used for the analysis of kerosene vapor in gas phase. Four calibration samples were prepared. To prepare a calibration sample, four one-liter Tedlar bags (Supelco^{TM}) were filled with 500 ml of carbon dioxide using a polyethylene syringe. 10, 20, 30, and 40 µl of kerosene were drawn by a Hamilton gas syringe and injected into the Tedlar bags. The calibration bags were allowed to stand for more than 12 hours to ensure complete evaporation of kerosene took place. The calibration samples were then analyzed by GC to produce a calibration curve. The same Tedlar bags were used for sampling of the gas phase from a port between the mass flow meter and the bubble flow meter during experiments. Then the samples were analyzed by GC. By comparing the sample GC peak with the calibration curve, the vapor concentrations of kerosene in gas phase was determined.

4.3 Results and Discussion

4.3.1 Influence of Low-Permeability Layer on NAPL Recovery

In order to investigate the influence of low permeability layers on residual NAPL recovery, three column experiments were conducted. The parameters of the three column experiments are shown in Table 4.3. The coarse sand used in experiments No.5 and No.6 was Barco49 and the low permeability layers were made of sieved fine sand (SFS). The low permeability

layers were arranged at the middle and the upper of the column for experiments No.5 and No.6, respectively, as shown in Figure 4.4. Experiment No.7 was a homogeneous column packed with coarse sand of similar granulometry (Barco 49A).

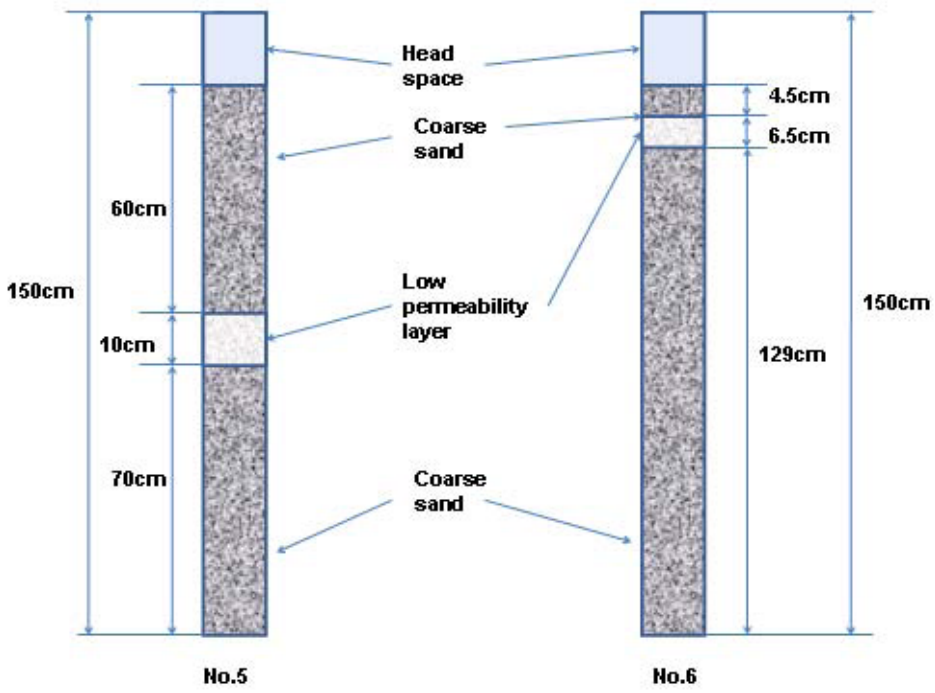

Figure 4. 4 Arrangement of low permeability layers in columns

Table 4. 3 Main properties and operating parameters of experiments No.5, 6, and 7

Experiment ID.	No. 5	No. 6	No.7
Type of column pack	layered	layered	Homogeneous
Coarse sand average grain size, μm	305.8	305.8	324.1
Average grain size of fine sand(SFD), μm	96.3	96.3	n/a
Height of layer, cm	10	6.5	n/a
Porosity	39.0%	37.8%	37.8%
Permeability, Darcy	34.7	27.3	42.1
Type of NAPL	Kerosene	Kerosene	Kerosene
Residual NAPL saturation, after 1st Water-flooding	17.5%	16.8%	18.3%
Initial residual saturation, after 2nd water-flooding	15.8%	14.2%	17.9%
Water flow rate of SWI	15-30 ml/min	30 ml/min	20-30 ml/min
Total running time, hrs	35.9	20.1	55.3
PV of water injected	106	69	137
Final cumulate recovery	42.0%	26.8%	62.0%
Final residual NAPL saturation	9.2%	10.4%	6.8%

The cumulative NAPL recoveries and residual NAPL saturation vs. pore volume of water injected during SWI operation are plotted in Figure 4.5 and 4.6 respectively. The curves in the figures clearly indicate that a low permeability layer in the column significantly decreases the final NAPL recovery, leaving a higher final residual NAPL saturation in layered column packs after SWI recovery operation. The location of low permeability layers in the column strongly affects the recovery behavior of entrapped residual NAPL during SWI operation.

The highest cumulative NAPL recovery is achieved in experiment No.7 with a homogenous

sand-packed column without a low permeability layer. The final recovery and residual saturation are 62% and 6.8% after 55.3 hours of SWI operation, or 137 pore volumes of water injected. The final accumulative NAPL recovery of experiment No.5, the column with low permeability layer in the middle, is lower than that of experiment No.7, but higher than that of experiment No.6. The final recovery and residual saturation are 42% and 9.2% after 35.9 hours of SWI operation, or 106 pore volumes of water injection. The final cumulative NAPL recovery of experiment No.6, the column with low permeability layer at the top, is lowest. The final NAPL recovery and residual NAPL saturation are 26.8% and 10.4% after 20.1 hours of SWI operation, or 69 pore volumes of water injection.

The recovery rate, corresponding to the slope of the recovery curves, was different from column to column in the early stages. Experiment No.7 exhibited the highest recovery rate during the first 30 pore volumes of water injected. This might be due to the higher initial residual NAP saturation, higher permeability, and homogeneous character of the column. Although experiment No.6 (with low permeability layer at top) had the lowest permeability and initial residual NAPL saturation, the recovery rate of experiment No.6 after the first 2 pore volumes of injection was as high as that of experiment No.7 and higher than that of experiment No.5 after the first 8 pore volumes of injection. This might be mainly caused by the higher starting injection flow rate of SWI for experiment No.6: the starting injection flow rates for experiments No.6, No.5, and No.7 were 30, 15, and 20 ml/min respectively. Mobilization of residual NAPL during overnight stoppage of injection was observed in the experiments and was more significant when the residual NAPL saturation was more than 10% in the early stages.

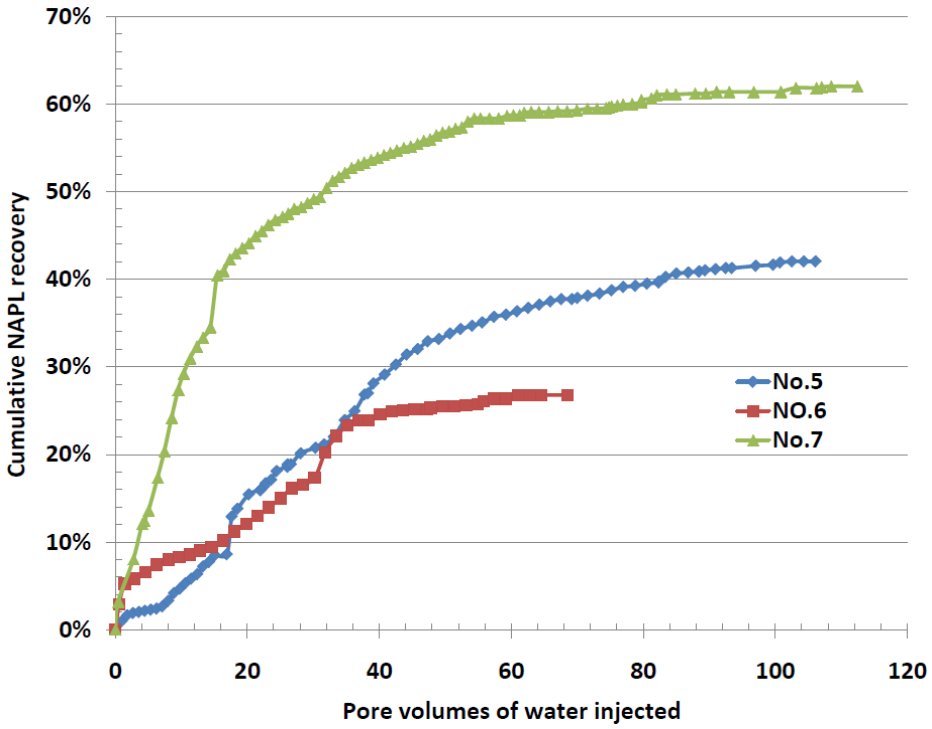

Figure 4. 5 Plot of cumulative NAPL recovery vs. PV of water injected for experiments No.5, 6 and 7

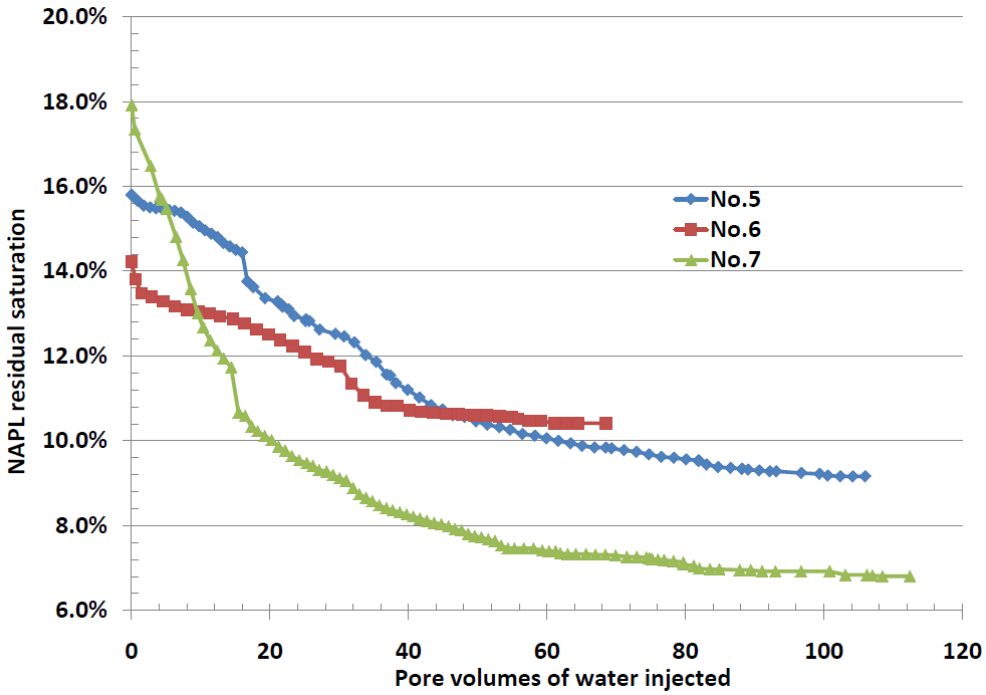

Figure 4. 6 Plot of residual NAPL saturation vs. PV of water injected for experiments No.5, 6 and 7

In order to investigate the influence of low-permeability layers on the immiscible displacement, a visualization experiment was also conducted. A series of photographs in Figure 4.7 describe the changes observed during SWI operations. After packing the column with a low-permeability layer, kerosene dyed by Sudan Black was injected from the top of the column. In the homogeneous coarse sand packs, a diffuse displacement front developed, as shown in Figure 4.7 (A). When the displacement front reached the upper boundary between coarse sand and low permeability layer, the kerosene began to collect in the coarse sand close to the upper boundary and the kerosene saturation built up there, as shown in Figure 4.7 (B). When the kerosene saturation was high enough, the kerosene was able to enter into the fine sand, and the displacement continued. However, when the displacement front passed through the lower coarse sand-fine sand interface, there was no build-up of kerosene saturation in low permeability layer close to the lower boundary, as shown in Figure 4.7 (C). After water flooding, the NAPL saturation built up in the coarse sand below the lower boundary. The color in the low permeability layer was lighter than the color in the coarse sand; it seems that the kerosene saturation in the low permeability layer was lower than that in coarse sand, as shown in Figure 4.7 (D). The situation during and after SWI recovery operations are shown in Figures 4.7 (E) and (F). It is obvious that a high NAPL saturation zone still existed in the coarse sand below the lower boundary after SWI recovery, although the color was lighter than the color before SWI. The result of residual saturation distribution in experiment No.6 analyzed by GC and shown in Figure 4.8 was in agreement with this visualization observation. In the sample which contained the low permeability layer, the kerosene saturation was 15.56%, even higher than the initial average residual kerosene saturation in experiment No.2 which was 14.2%.

a) Emplacement of NAPL in coarse sand

b) Saturation build-up at upper boundary

c) After NAPL emplacement

d) After water flooding.

e) During SWI recovery

f) After SWI recovery

Figure 4. 7 Photographs of low permeability layer visualization experiment

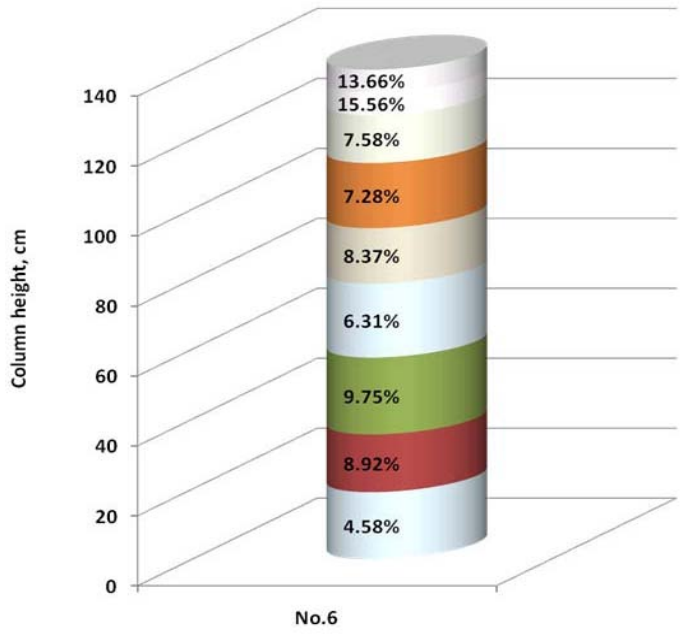

Figure 4. 8 Residual saturation distribution of experiment No.6 after SWI recovery

The above observations of high NAPLs saturations building up in the coarse sand close to the boundaries, low recovery, and high residual saturations in column experiments with the low permeability layers, might be attributed to the capillary barriers (Valkenburg et al., 2002) caused by small pore throat size of fine sand, which hindered the passage of NAPL-water interfaces. The capillary pressure can be expressed as:

$$p_c = \frac{2\sigma \cos\theta}{r} \text{----------Equation 4.3}$$

In the experiments described here, the contact angle θ and the interfacial tension are constant. Thus the capillary pressure is dependent on the pore radius (r) only. In the low permeability layer, the pore throat radii are smaller than those in the coarse sand. Especially at the boundaries, there is a zone where the coarse sand and fine sand mix, where even

smaller throat sizes could be produced during the process of column packing when vibration was applied, resulting in substantially higher capillary pressure. When the displacement front arrived at this zone, the NAPL accumulated because a relatively higher displacement pressure was needed. Only when the local NAPL saturation was high enough, could the NAPL move through.

4.3.2 Effect of Grain Size and Contaminant Type on Recovery

To study the effect of sand grain size and the contaminant type on the recovery performance of SWI operation, five column experiments were conducted. The parameters of the experiments are shown in Table 4.4. Because the melting point of hexadecane is 18^{o}C and the temperature of tap water is 17^{o}C, a kerosene-hexadecane mixture with a volume ratio of 1:2 was used in the experiments to avoid freezing the NAPL. All experiments were conducted in columns with homogeneous sand packs. The injection flow rate was initially around 20 ml/min and reached final value of about 40 ml/min. Depending on the working state of gPRO^{TM}, the pressure of the tap water system, and injection flow rates, the final gas saturations in the column ranged between 21% and 26%; and the ratios of gas flow rate to water flow rate at steady state varied from 1.9 to 2.8.

Table 4. 4 Main properties and operating parameters for the columns No.8 -12

Experiment ID.	No. 8	No. 9	No.10	No.11	No.12
Type of column pack	Homogeneous	Homogeneous	Homogeneous	Homogeneous	Homogeneous
Type of sand	Barco 95	Barco 95	Barco 49	Barco 49	Barco 49A
Average grain size, μm	168.9	168.9	305.8	305.8	324.1
Bulk volume, ml	1616	1616	1616	1616	1616
Porosity	38.7%	36.9%	37.9%	35.0%	35.7%
Permeability, Darcy	11.4	9.1	31.2	29.4	41.9
Type of NAPL	Mixture	kerosene	Mixture	Kerosene	Kerosene
volume of NAPL, ml after 1st Water-flooding	102.5	100.2	114	95.5	97.2
Residual saturation, after 1st Water-flooding	16.3%	16.8%	18.5%	16.9%	16.8%
Volume of NAPL, ml after 1st Water-flooding	83.3	88.7	93.2	86.5	93.8
Initial residual saturation, after 2nd flooding	13.3 %	14.9 %	15.2 %	15.3 %	16.2 %
Injection rate, SWI,	20-40	20-40	20-40	20-40	20-40
PV of water injected	317	256	283	221	162
Total running time, hrs	136	95	118	88	63
Volume recovered, ml	36.8	51.5	47.6	51	56.3
Final cumulate recovery	44.2%	58.1%	51.1%	59.0%	59.9%
Volume of residual, ml	46.2	37.2	45.6	36.5	37.5
Final residual saturation by mass balance	7.4%	6.2%	7.4%	6.3%	6.5%

NAPL recovery behavior of columns with different grain sizes: Experiments No.8 and No.10 involved columns with permeabilities of 11.4 and 31.2 Darcy (average grain sizes of 168.9 and 305.8 μm) contaminated with a kerosene-hexadecane mixture. The final cumulative recoveries for these two experiments were 44.2% and 51.1% after 136 and 118

hours of SWI operations, or 317 and 283 pore volumes of water injected, respectively. However, the final residual NAPL saturations were the same at 7.4%. Experiments No.9, No.11, and No.12 were conducted in columns with the permeabilities of 9.1, 29.4, and 41.9 Darcy (average grain sizes of 168.9, 305.8, and 324.1μm) contaminated with kerosene. The final cumulative recoveries for these three experiments were 58.1%, 59.0, and 59.9% after 95, 88, and 63 hours of SWI operation, or 256, 221, and 162 pore volumes of water injected, and the final residual saturations were 6.2%, 6.3%, and 6.5%, respectively.

Plotted in Figures 4.9 and 4.10 are cumulative NAPL recovery and residual NAPL saturation vs. pore volume of water injection during SWI for the columns with the same contaminant, but different sand grain size. The residual saturation curves indicate that the grain sizes of the sands almost has no influence on the final residual saturations after SWI. Wettability, pore size distribution (especially pore-throat aspect ratio), and displacement conditions are three major factors that affect the residual NAPL saturation. In these experiments, for a given contaminant, the sands were made of the same material, and the particle size distributions were very similar as shown in Figure 4.11, the systems should have same wettabilities, and similar pore-throat aspect ratios for the pore structures, although the pore sizes were different. Furthermore all columns were operated at similar injection conditions, thus the finally residual saturations were very close for the same contaminant, while the final cumulative NAPL recoveries were determined by the initial residual NAPL saturations, i.e. the higher the initial residual saturation, the higher the final cumulative recovery. The grain size (permeability), combined with injection flow rate, affect the NAPL recovery rate and recovery operation time; the higher the permeability and injection flow rate, the higher recovery rate and the shorter the recovery time.

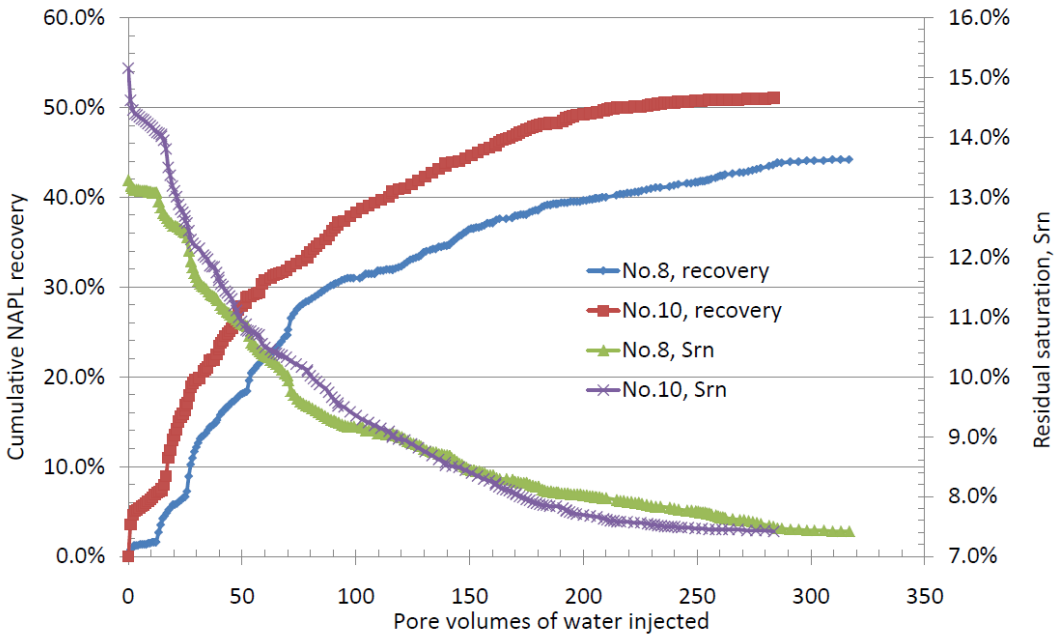

Figure 4. 9 Cumulative NAPL recovery and residual NAPL saturation vs. PV of water injected in kerosene-hexadecane mixture column experiments

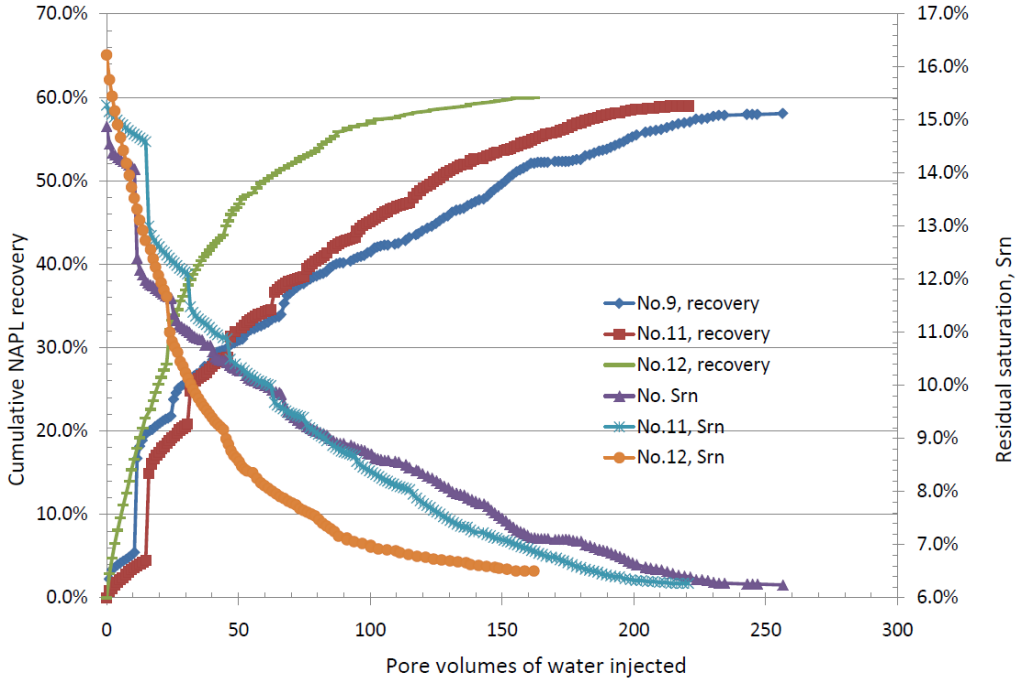

Figure 4. 10 Cumulative NAPL recovery and residual NAPL saturation vs. PV of water injection in kerosene columns

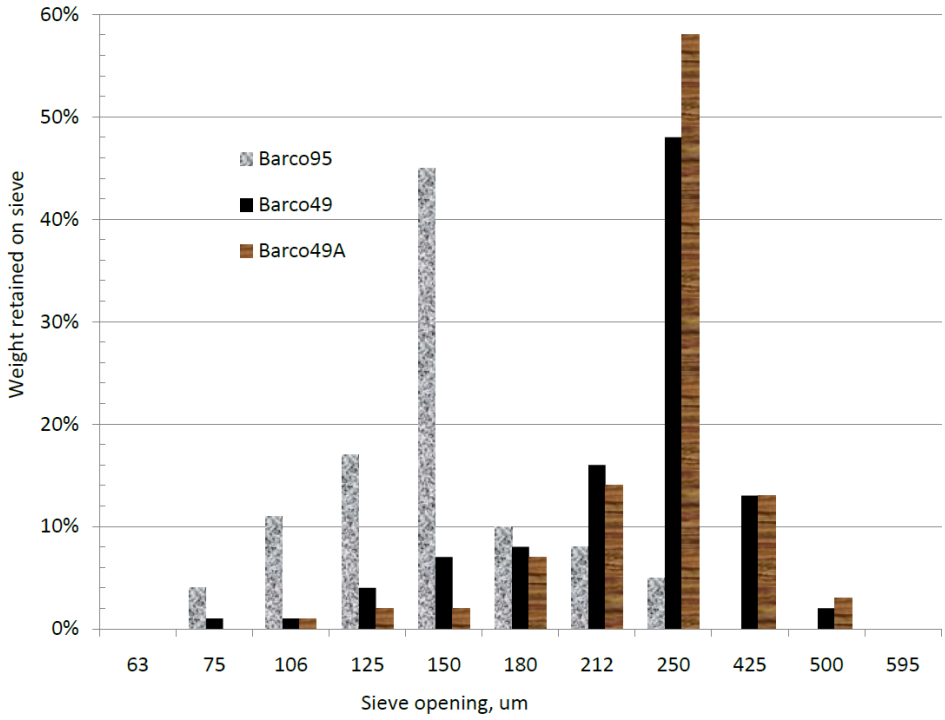

Figure 4. 11 Particle size distributions of the sands

NAPL recovery behaviors of columns with different contaminants: Plotted in Figures 3.12 and 3.13 are cumulative recoveries and residual NAPL saturations vs. pore volume of water injected during SWI for columns with same average grain size, but different contaminants. The curves in the figures show that the properties of contaminant strongly affect the entrapped residual recovery behavior during SWI. One observes that, the kerosene-hexadecane mixture columns had higher final residual saturations, lower final cumulative recoveries and recovery rates, longer recovery time. Additionally, significant kerosene banks were observed to form during overnight stoppage of SWI, when the residual saturations were more than 10%, consistent with the previous observations in experiments No.3 and No.4. In columns contaminated with the kerosene-hexadecane mixture, such NAPL banks were very small.

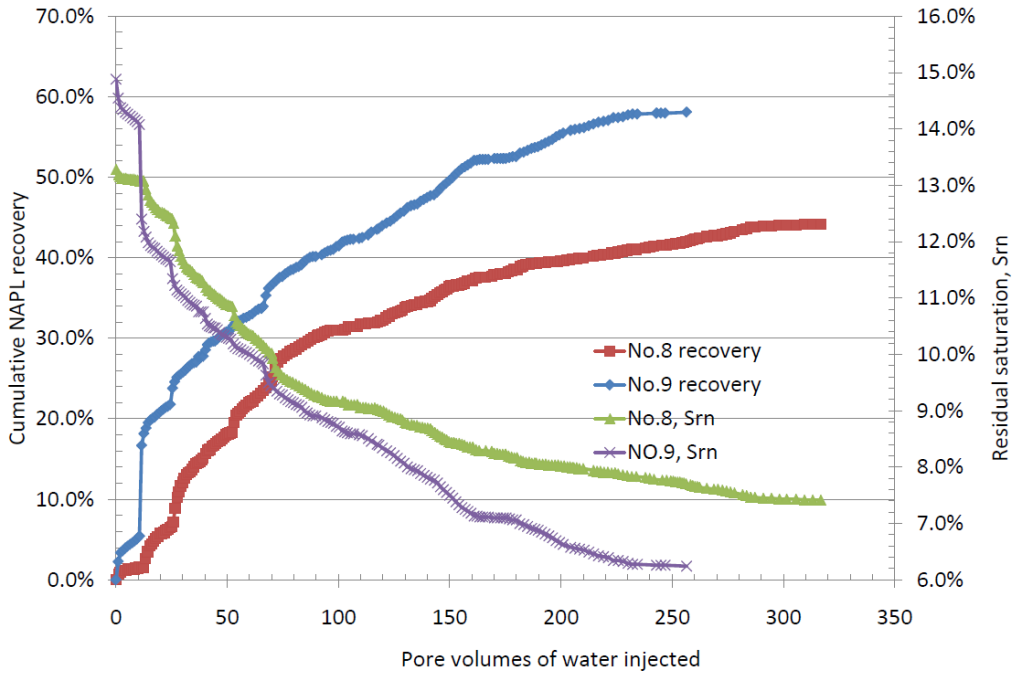

Figure 4. 12 Cumulative NAPL recovery and residual NAPL saturation vs. PV of water injection in lower permeability columns

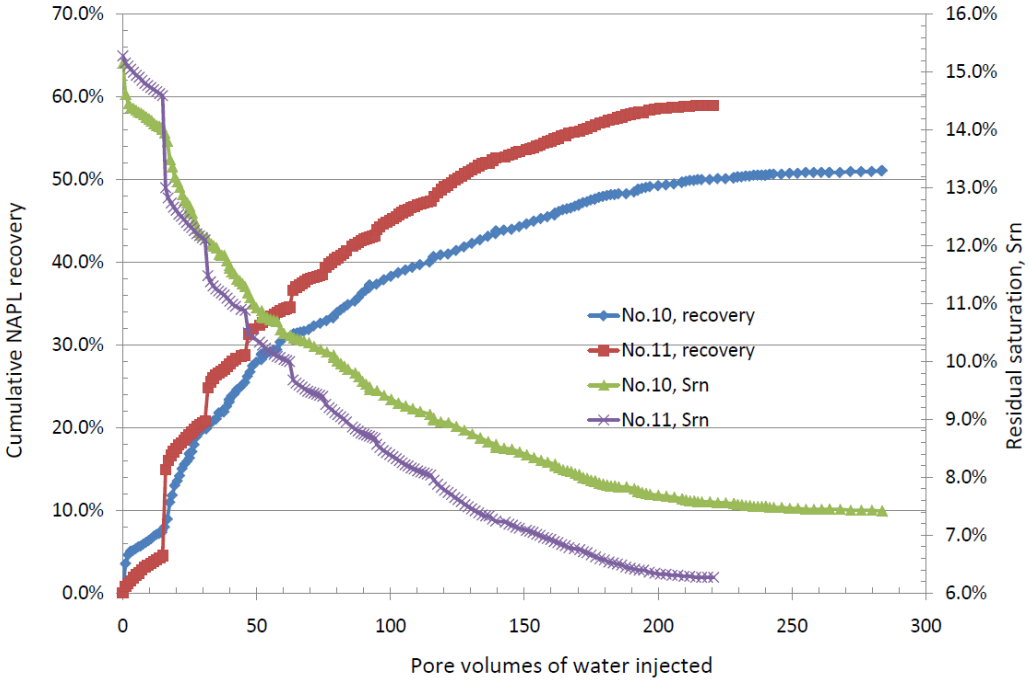

Figure 4. 13 Cumulative NAPL recovery and residual NAPL saturation vs. PV of water injection in higher permeability columns

The adverse influence of hexadecane on the recovery behaviors might be attributed to the following two factors. One is its higher viscosity, which reduces its mobility during the displacement process. The other one is its more negative spreading coefficient by comparison to pure kerosene, which seems to play a rather important, and as of yet difficult to qualify, role in recovery behavior.

The three-phase immiscible displacement process in porous media is controlled by capillarity. Suppose that gas, NAPL, and water exist in a network shown as in Figure 4.14. The capillary pressures for double drainage displacement and single drainage displacement (gas displacing water) can be estimated by Equation 4.4 and Equation 4.5, respectively:

$$p_{C,DD} = \frac{2\sigma_{nw}\cos\theta_w}{r_n} + \frac{2\sigma_{ng}\cos\theta_{ng}}{r_n} \quad \text{----------Equation 4.4}$$

$$p_{C,D} = \frac{2\sigma_{gw}\cos\theta_w}{r_w} \quad \text{----------Equation 4.5}$$

where σ_{nw}, σ_{ng}, and σ_{gw} are the NAPL-water, NAPL-gas, and gas-water interfacial tensions, and θ_w , θ_{ng} are the corresponding contact angles as shown in the figure. The double drainage displacement will happen if $p_{C,DD} < p_{C,D}$, i.e.:

$$\frac{2\sigma_{nw}\cos\theta_w}{r_n} + \frac{2\sigma_{ng}\cos\theta_{ng}}{r_n} < \frac{2\theta_{gw}\cos\theta_w}{r_w} \quad \text{----------Equation 4.6}$$

Rewriting Equation 4.6 yields:

$$\sigma_{nw} + \sigma_{ng}\frac{\cos\theta_{ng}}{\cos\theta_w} < \sigma_{gw}\frac{r_n}{r_w} \quad \text{----------Equation 4.6 a}$$

For a given network configuration, the right-hand side is constant. A less negative spreading coefficient implies a smaller value of the sum $\sigma_{nw} + \sigma_{ng}$, and is thus seen to favor double drainage displacement. Generally speaking, a more negative coefficient tends to suppress the double drainage displacement, resulting in less reconnection of NAPL blobs during SWI. Consequently, the amount of NAPL blobs reconnected during the gas de-saturation process is also diminished as discussed in Chapter 3. This could be the reason why the kerosene-hexadecane mixture columns exhibited lower final recoveries, lower recovery rates, smaller NAPL bank formation during overnight standing, and higher final residual NAPL saturations than of kerosene columns.

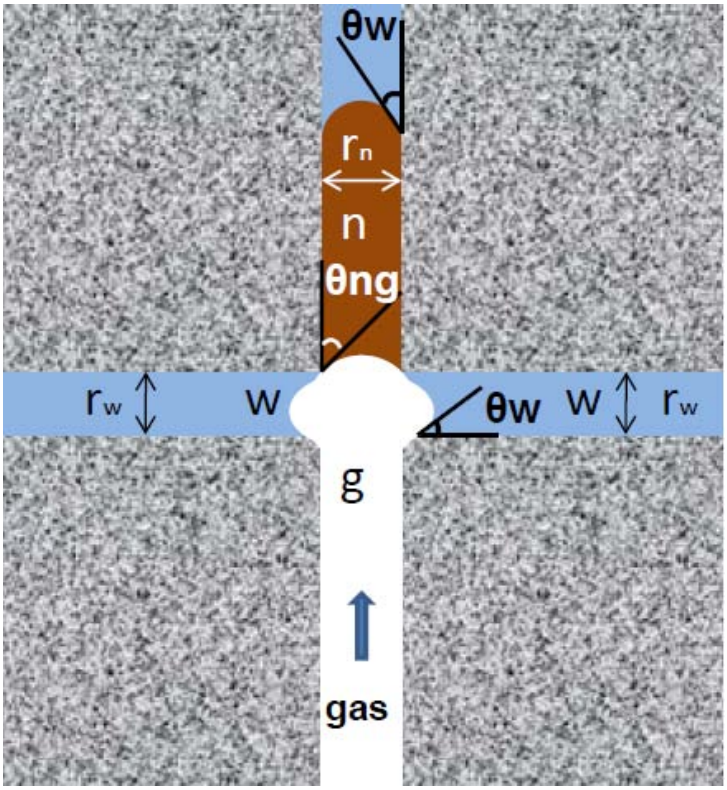

Figure 4. 14 Schematics of double drainage or single drainage taking place in network

4.3.3 Mass Balance Analysis

Table 4.6, Figure 4.15 and Figure 4.16 summarize the results of mass balance and residual distributions for the 5 column experiments. For the kerosene-hexadecane mixture column experiments, No.8 and No.10, the residual saturations calculated from the liquid mass balance and the GC analysis were very close. However, for kerosene column experiments, No 9, No.11, and No.12, the residual saturations calculated from the liquid mass balance were greater than those from GC analysis, indicating that significant volatilization of kerosene took place during the SWI operations, despite the very low vapor pressure of kerosene. By comparing results in Figure 4.15 and Figure 4.16, there were no NAPL saturation gradients within kerosene-hexadecane mixture columns, but obvious NAPL saturation gradients were observed within kerosene columns at the conclusion of the experiment, which is strong indication for the volatilization of kerosene during SWI. At the bottom of the column, the concentration of kerosene in the gas phase would be lower than at the upper part of the column, thus the driving force for mass transfer would be greater at the bottom, causing more kerosene evaporation from the liquid phase into the gas phase and resulting in lower residual saturation at the bottom. The volatilization of NAPL during SWI was confirmed by the GC analysis of kerosene components in the gas phase in experiment No.12.

Table 4. 5 Mass balance for experiments No.8 -12

	No.8	No.10	No.9	No.11	No.12
V_{irn}, initial residual NAPL, ml	88.3	93.2	88.7	86.5	93.8
V_n, liquid NAPL recovered, ml	36.8	47.6	51.5	51	56.3
V_{rn}, residual NAPL by liquid balance, ml	46.5	45.6	37.2	35.5	37.5
V_{rn}, residual NAPL by GC, ml	46.8	44.1	21.9	19.5	25.6
S_{rn}, residual NAPL by liquid balance	7.4%	7.4%	6.2%	6.3%	6.5%
S_{rn}, residual NAPL by GC	7.5%	7.2%	3.7%	3.4%	4.4%
Finnal recovery, votalization not considered			58.1%	59.0%	59.9%
Final recovery, votalization considered			75.3%	77.5%	72.7%
V_n, NAPL in gas phase by liquid balance, ml					11.9
V_n, NAPL in gas phase by GC, ml					14.8

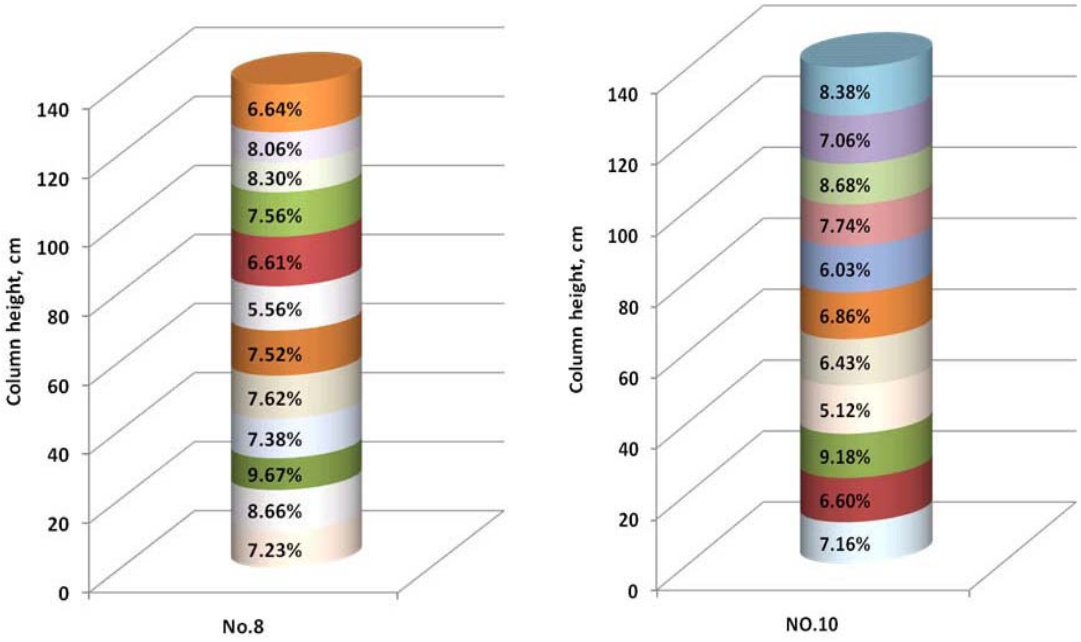

Figure 4. 15 Distribution of residual NAPL in kerosene-hexadecane mixture columns

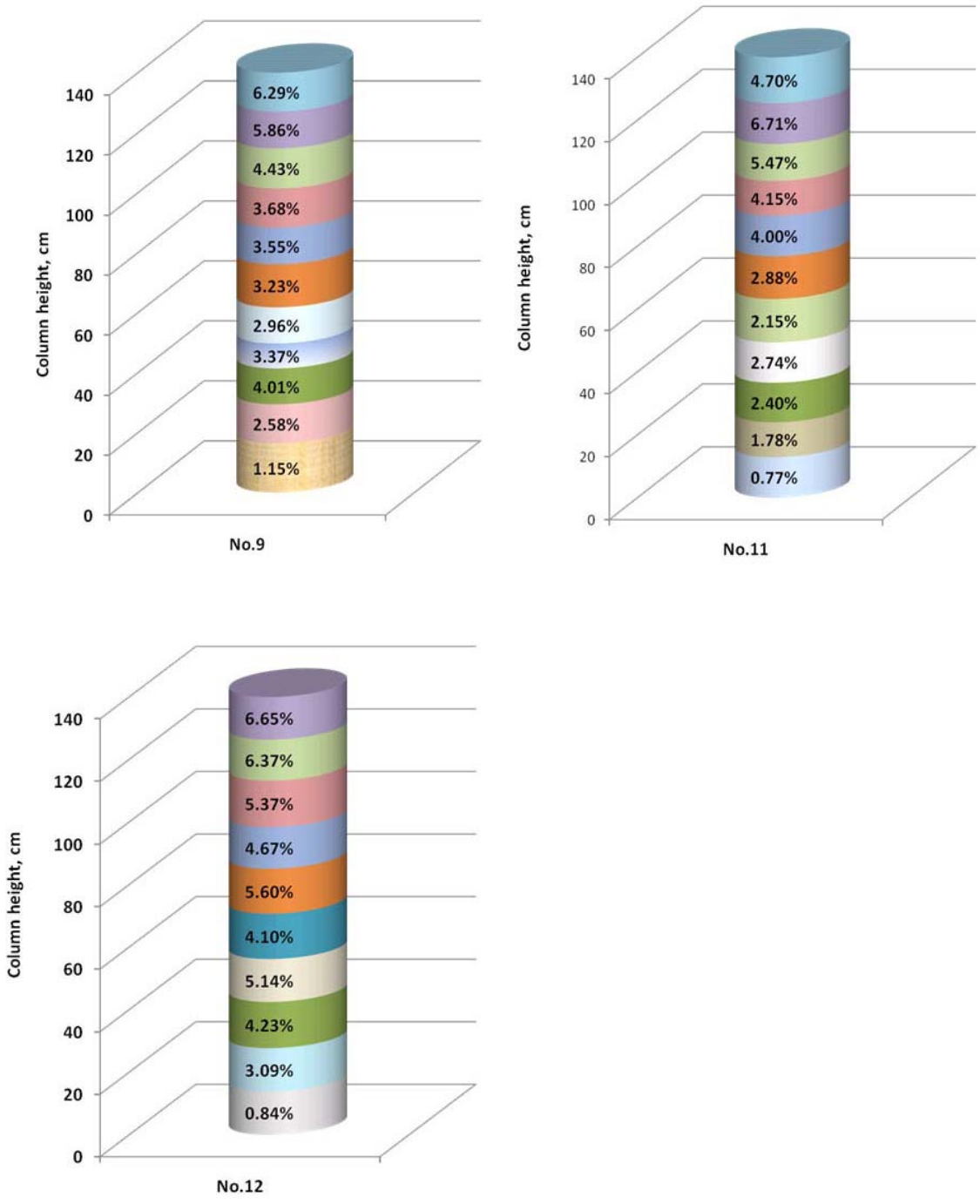

Figure 4. 16 Distribution of residual NAPL in kerosene columns

Chapter 5

Supersaturated Water Injection in the Absence of Residual NAPL Saturation: Gas Evolution Dynamics

5.1 Scope

In situ gas evolution and flow during SWI clearly drives NAPL recovery and must be understood in its own right before predictions of NAPL recovery can be made. Thus, in order to verify appropriate simulation software, supersaturated water injection experiments in the absence of residual NAPL saturation in the column packs were conducted to provide experimental data for model calibration. A test method was developed to determine the concentrations of dissolved carbon dioxide in water to provide reliable simulation input. The dissolved CO_2 concentration tests were carried out based on mass balance.

5.2 Experimental Setup and Procedures

5.2.1 Experiment Setups

The setup for SWI experiments in the absence of NAPL saturation in the column packs was similar to that described in Chapter 4. The setup for the tests of dissolved CO_2 concentration in supersaturated water is shown in Figure 5.1. The exsolution of gas from of the CO_2-supersaturated water took place in an empty rubber tube with inner diameter of about 10 mm, instead of in a sand-packed column.

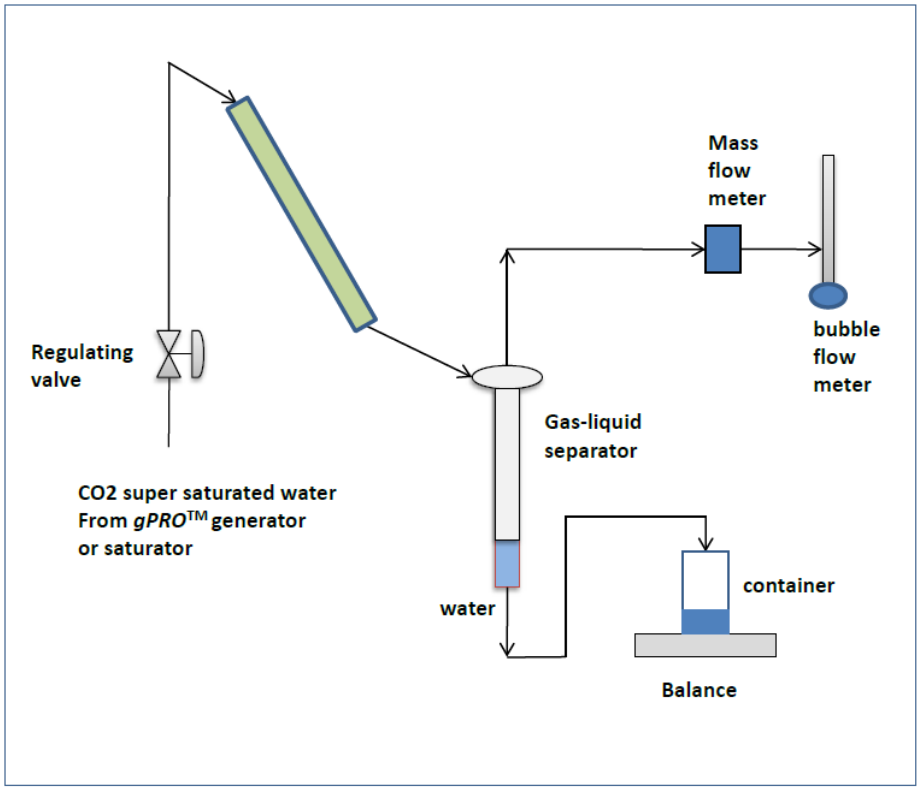

Figure 5. 1 Schematics of experimental setup for saturation efficiency test

5.2.2 SWI Operation Procedures

Column packing, permeability and gas saturation measurement, measurement of gas flow rate and pressure, and SWI operation were as described in Chapters 3 and 4, with the following differences. (a) Before starting SWI, no water was in the connection between the column and separator, no headspace in the column, and the water level in the separator was at the desired location. (b) During SWI operations, the setting of the metering valve was kept unchanged and water flow rate was measured by weight changes only to avoid the disturbance of gas flow rate by the fluctuation of water level in separator. Water flow rates were measure every 50 seconds during the transient stage and after SWI was stopped, over longer intervals during steady state operation. (c) If the same column was going to be run

another time, sufficient water flooding using non-carbonated water was applied to ensure the starting residual gas saturation in the column was as close to zero as possible (typically less than 2%).

5.2.3 Test of CO_2 Concentration in Supersaturated Water

In the tests of dissolved CO_2 concentration in supersaturated water, a gPRO^{TM} generator and a saturator consisting of a glass column filled with glass beads were used to produce CO_2-supersaturated water. To make sure the water was sufficiently saturated with CO_2, the gPRO^{TM} generator was turned on 3 hours before commencing the test. For the glass column saturator, the CO_2 pressure in the saturator was controlled at 55 psig by a regulating valve connected to a CO_2 cylinder, and the tap water was injected into the saturator at a very low flow rate. After the saturator was almost full, water injection was stopped and the CO_2 pressure was kept at 60 psig for 24 hours.

The flow rate of injected CO_2-saturated water was regulated by a metering valve. The saturation pressure was measured by a pressure transducer positioned at the valve entrance metering valve. The CO_2-saturated water out of the metering valve then entered into a rubber tube (inner diameter of 10 mm), where supersaturated water was allowed to degas, the mixture of gas and water was then introduced into the gas-water separator. The gas came out from the top of the separator, and its flow rate was measured by the mass flow meter. The water was collected at the bottom, and its flow rate was measured on a balance to avoid disturbance of gas flow rate due to the fluctuation of water level in the separator. Before taking measurements, the system was run for about one hour to achieve steady state. During the operation, the CO_2 concentration in effluent was measured by titration method, as

explained next.

5.2.4 Measurement of Dissolved CO_2 Concentration in Effluent

A certain volume (around 10 ml) of water out of the separator was added to sufficient amount of known *NaOH* solution (5ml, 0.525mole/L, diluted by 10 ml of water) to absorb all CO_2. The chemical reaction which takes place is:

$2NaOH + CO_2 = Na_2CO_3 + H_2O$ ----------Equation 5.1

The resulting mixture was titrated with a diluted *HCl* solution (0.1115 Mole/L). The following chemical reactions took place during titration:

$NaOH + HCl = NaCl + H_2O$ (at $pH > 12$) ----------Equation 5.2

$Na_2CO_3 + HCl = NaHCO_3 + NaCl$ (at $9 < pH < 12$)----------Equation 5.3

$NaHCO_3 + HCl = NaCl + CO_2 + H_2O$ (at $pH < 9$)----------Equation 5.4

Figure 5.2 is the titration curve of Na_2CO_3 titrated by HCl. The titration endpoint was chosen as the point when the reaction of Equation 5.3 is completed, which is when pH value of the solution is between 9 and 10 and the titration indicator phenolphthalein changes colors.

Suppose that M_{OH}, M_{OH}^1, and M_{OH}^2 are the moles of total –OH groups, excess –OH groups, and the –OH groups reacted with CO_2, respectively. The following relation obviously holds:

$M_{OH} = M_{OH}^1 + M_{OH}^2$ ----------Equation 5.5

Letting M_H, M_H^1, and M_H^2 be the moles of total HCl, and HCl consumed by the chemical reaction in Equation 5.2 and Equation 5.3, respectively. We also have:

$$M_H = M_H^1 + M_H^2$$ ----------Equation 5.6

Based on the reaction stoichiometry, we also get the following relations:

$$M_{OH}^1 = M_H^1$$ ----------Equation 5.7

$$M_{OH}^2 = M_H^2$$ ----------Equation 5.8

The solution of Equations 5.5 - 5.8 is:

$$M_{OH}^2 = M_{OH} - M_H$$ ----------Equation 5.9

From the reaction described by Equation 5.1, the moles of CO_2 absorbed by $NaOH$ (M_{CO2}) should be:

$$M_{CO2} = \frac{M_{OH}^2}{2}$$ ----------Equation 5.10

That way, the CO_2 dissolved in effluent is determined.

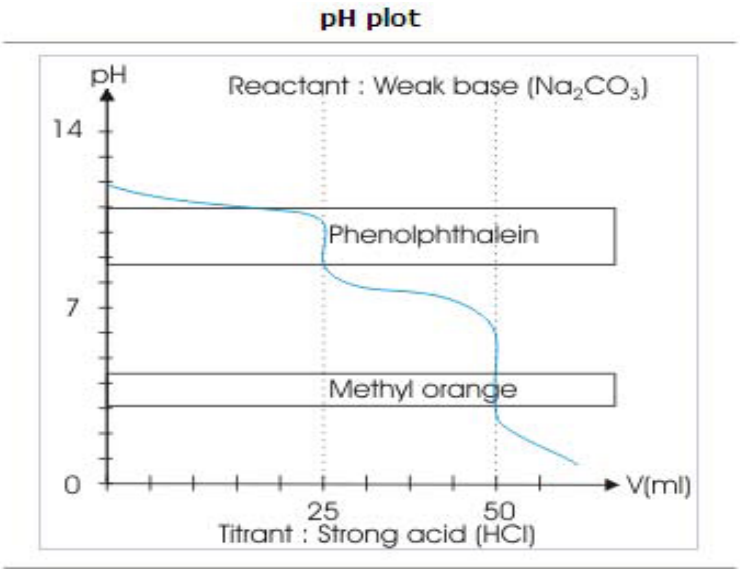

Figure 5. 2 Titration curve of Na_2CO_3, acid is titrant (http://cnx.org/content/m17137/latest/)

5.3 Results and Discussion

5.3.1 Test of CO_2 Concentration in Supersaturated Water

The test results of CO_2 concentration in supersaturated water for glass column saturator are shown in Table 5.1. The dissolved CO_2 in the tube effluent was 0.0405mole/L. The calculated data in the table were based on Henry's law in dissolution equilibrium of pure CO_2 in gas phase at 23 ^oC and 60 psig. After the water was saturated by CO_2 for more than 24 hours, the ratios of tested C_{CO2} to the calculated C_{CO2} were close to 1. The tested and calculated gas flow rates were very close as shown in Figure 5.3.

Table 5. 1 Test data of CO_2 concentration in supersaturated water for glass column saturator

Time, s	Q_w, ml/min	Data tested		Data calculated		Ratio of $C_{CO2,tested}$ to $C_{CO2,calculated}$
		Q_g, ml/min	C_{CO2}, Influent Mole/L	Q_g, ml/min	C_{CO2}, Influent Mole/L	
500	6.6	19.23	0.17054	20.55	0.17952	0.950
800	5	15.06	0.17494	15.57	0.17952	0.974
1100	5.6	17.26	0.17805	17.44	0.17952	0.992
1400	6	17.62	0.17157	18.69	0.17952	0.956
1700	5.8	17.01	0.17140	18.06	0.17952	0.955
2000	5.6	16.79	0.17436	17.44	0.17952	0.971
2300	5.8	17.62	0.17611	18.06	0.17952	0.981
2600	5.8	17.81	0.17755	18.06	0.17952	0.989
2900	6	18.14	0.17545	18.69	0.17952	0.977
3200	6	18.17	0.17569	18.69	0.17952	0.979
3500	6.2	18.84	0.17611	19.31	0.17952	0.981

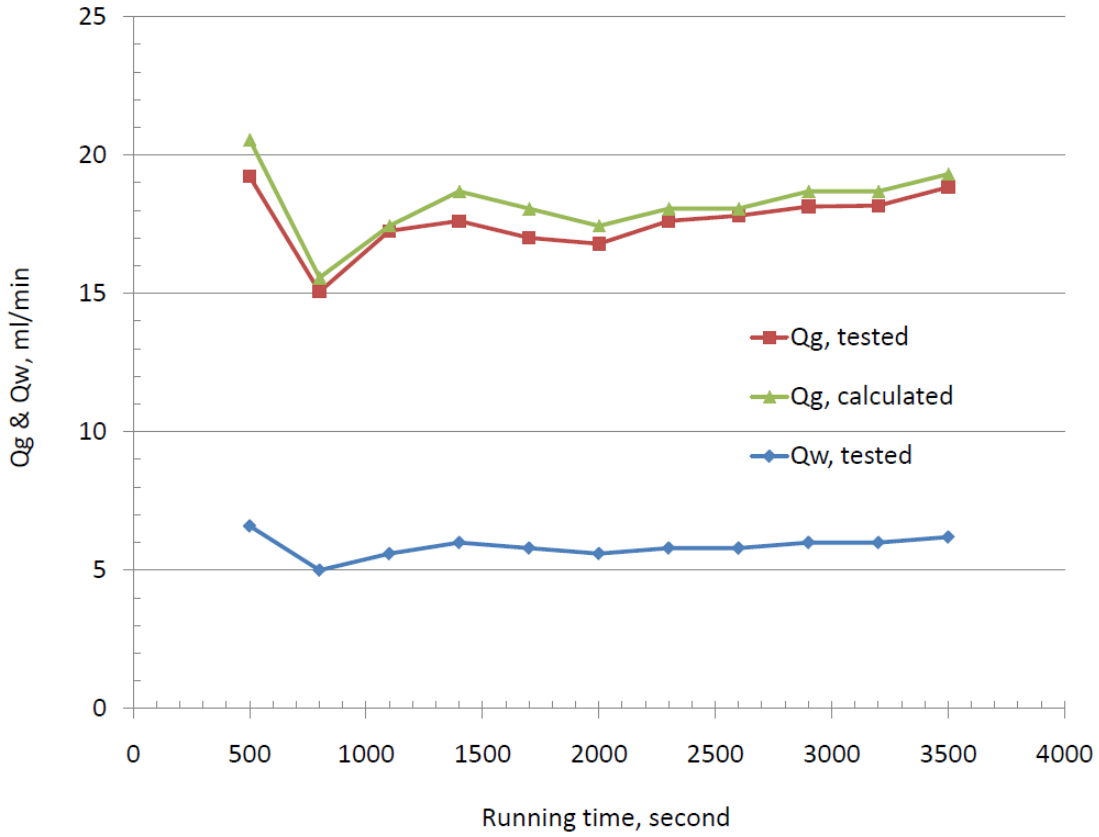

Figure 5. 3 Comparison of the gas flow rates between tested and calculated for glass column saturator

The test results of CO_2 concentration in supersaturated water for gPRO^{TM} at low injection flow rate (around 9 ml/min) and high injection flow rate (around 29 ml/min) are shown in Table 5.2 and 5.3 respectively. The concentrations of dissolved CO_2 in the tube effluent were 0.0397 and 0.0403mole/L for low and high injection flow rates, respectively. The ratios of tested C_{CO2} to the calculated C_{CO2} both at low and high flow rates decreased as the time elapsed. The magnitude of decrease of CO_2 concentration at low flow rate was greater than at high flow rate. The final ratios of tested C_{CO2} to the calculated C_{CO2} were less than 0.7 for both low and high flow rate tests.

Table 5. 2 Test data of CO_2 concentration in supersaturated water of gPRO™ at low injection flow rate

Time, s	Q_w, ml/min	Data tested		Data calculated		Ratio of $C_{CO2,tested}$ to $C_{CO2,calculated}$
		Q_g, ml/min	C_{CO2}, Influent mole/L	Q_g, ml/min	C_{CO2}, Influent mole/L	
850	9.1	20.91	0.14244	28.46	0.17952	0.793
1450	8.8	19.61	0.13917	27.56	0.17952	0.775
2050	8.9	17.89	0.12944	27.87	0.17952	0.721
2650	8.9	17.33	0.12664	27.87	0.17952	0.705
3250	8.9	16.09	0.12043	27.87	0.17952	0.671
5700	Dissolved CO_2 test					
6000	8.8	14.48	0.11313	27.56	0.17952	0.630
6600	8.8	14.15	0.11146	27.56	0.17952	0.621

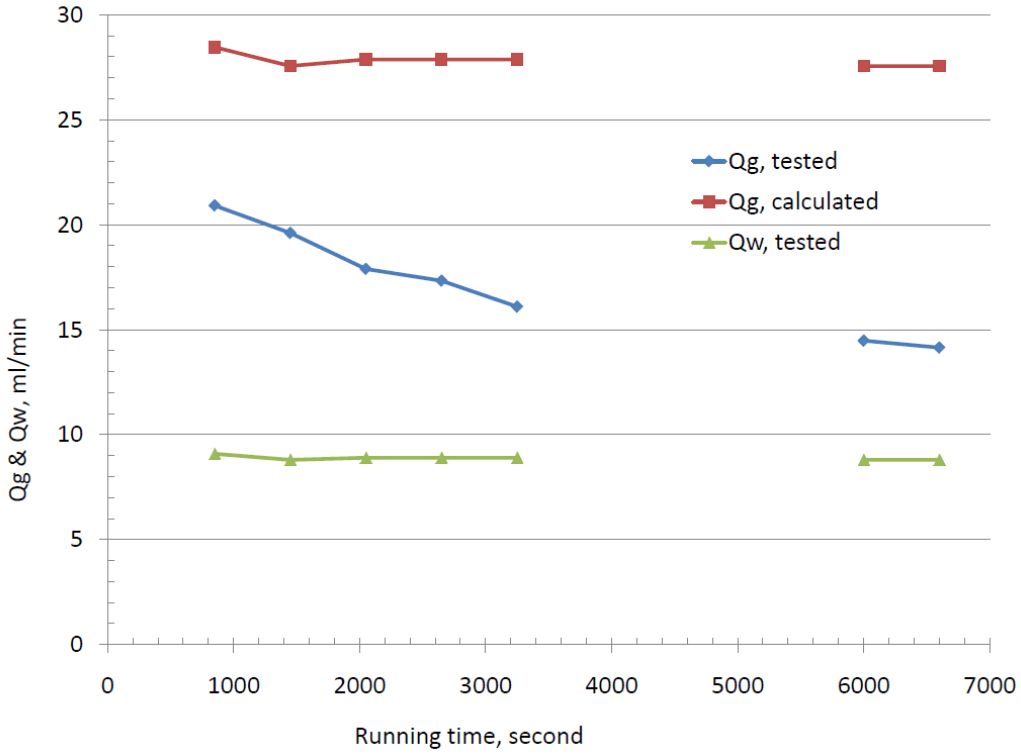

Figure 5. 4 Comparison of the gas flow rate between tested and calculated for gPRO™ at low injection flow rate

Table 5. 3 Test data of CO_2 concentration in supersaturated water for gPRO™ at high injection flow rate

Time, s	Q_w, ml/min	Data tested		Data calculated		Ratio of $C_{CO2,tested}$ to $C_{CO2,calculated}$
		Q_g, ml/min	C_{CO2}, Influent mole/L	Q_g, ml/min	C_{CO2}, Influent mole/L	
700	29.1	55.61	0.12562	90.75	0.17952	0.70.0
1300	29.1	55.14	0.12490	90.75	0.17952	0.696
1900	29.1	54.12	0.12332	90.75	0.17952	0.687
2500	29.1	52.90	0.12145	90.75	0.17952	0.67.7
3100	29	52.90	0.12174	90.44	0.17952	0.67.8
5200	Dissolved CO_2 test					
5800	29.1	52.35	0.12061	90.75	0.17952	0.672
7000	29.15	52.83	0.12121	90.90	0.17952	0.675

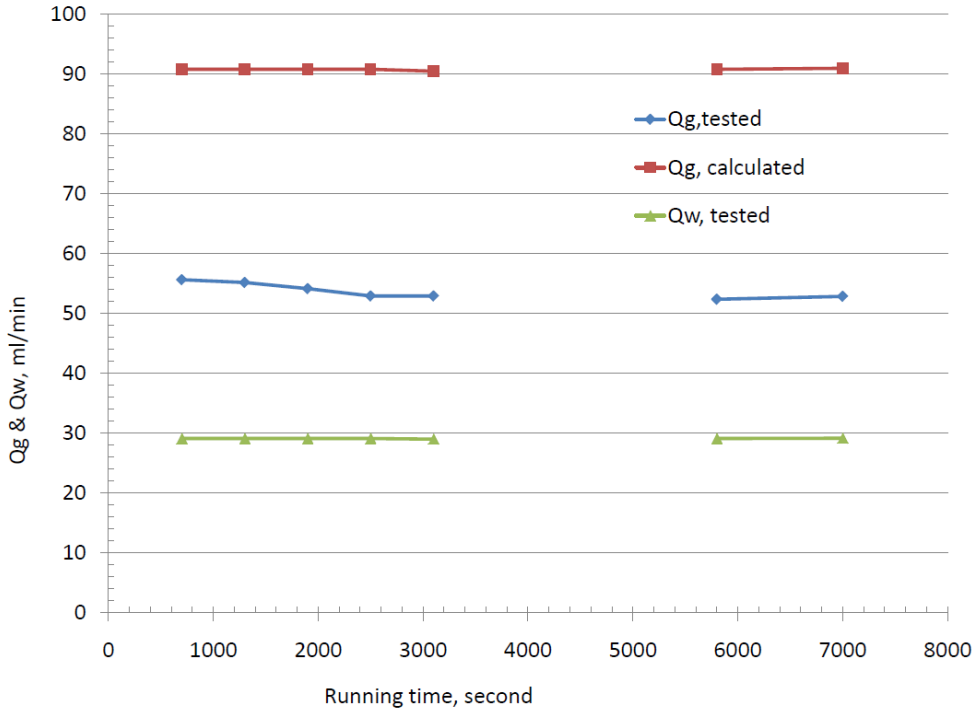

Figure 5. 5 Comparison of the gas flow rate between tested and calculated for gPRO™ at high injection flow rate

5.3.2 Experiments of SWI in the Absence of Residual NAPL

A series of experiments were conducted in columns with different packs. The experiments were run at various injection flow rates. The main parameters are shown in Table 5.4.

Table 5.4 Parameters of column experiment for SWI in the absence of residual NAPL

experiment ID	**Porous media**	**k, Darcy**	**porosity, %**	**SS-Q_w, ml/min**	**SS-Q_g, ml/min**	**SS-Q_g/Q_w**
CE1311	Sand Pack	11.3	36.70	27.60	87.23	3.16
CE1601	Sand Pack	29.5	35.00	13.20	26.20	1.98
CE2202	Sand Pack	41.0	35.10	20.82	44.28	2.13
CE2302	Sand Pack	38.7	35.21	11.49	20.16	1.75
CE2303	Sand Pack	38.7	35.21	17.40	37.76	2.17
CE2402	Glass Beads	57.2	38.43	18.72	37.13	1.98
CE2403	Glass Beads	57.2	38.43	29.66	58.16	1.96
CE2405	Glass Beads	57.2	38.43	11.49	20.02	1.74

The experimental data were simulated by Enouy et al. Some results related to the comparisons of experimental data and the simulations are summarized below. Figure 5.6 is the comparison of operating parameters, pressure at the bottom of the column, gas and water flow rates between the experimental data and simulation results for experiment CE2403. Experimental data (dotted curves) were adequately simulated, indicating that the simulation software is able to accurately reproduce the main physical processes. The discrepancy of gas flow rates between experiment data and simulation results might be caused by the decrease of CO_2 concentration in supersaturated water, which has been proved by the previous experiment in this chapter. The decrease of CO_2 concentration in supersaturated water might come from the fouling of the membrane phase contactor during operations.

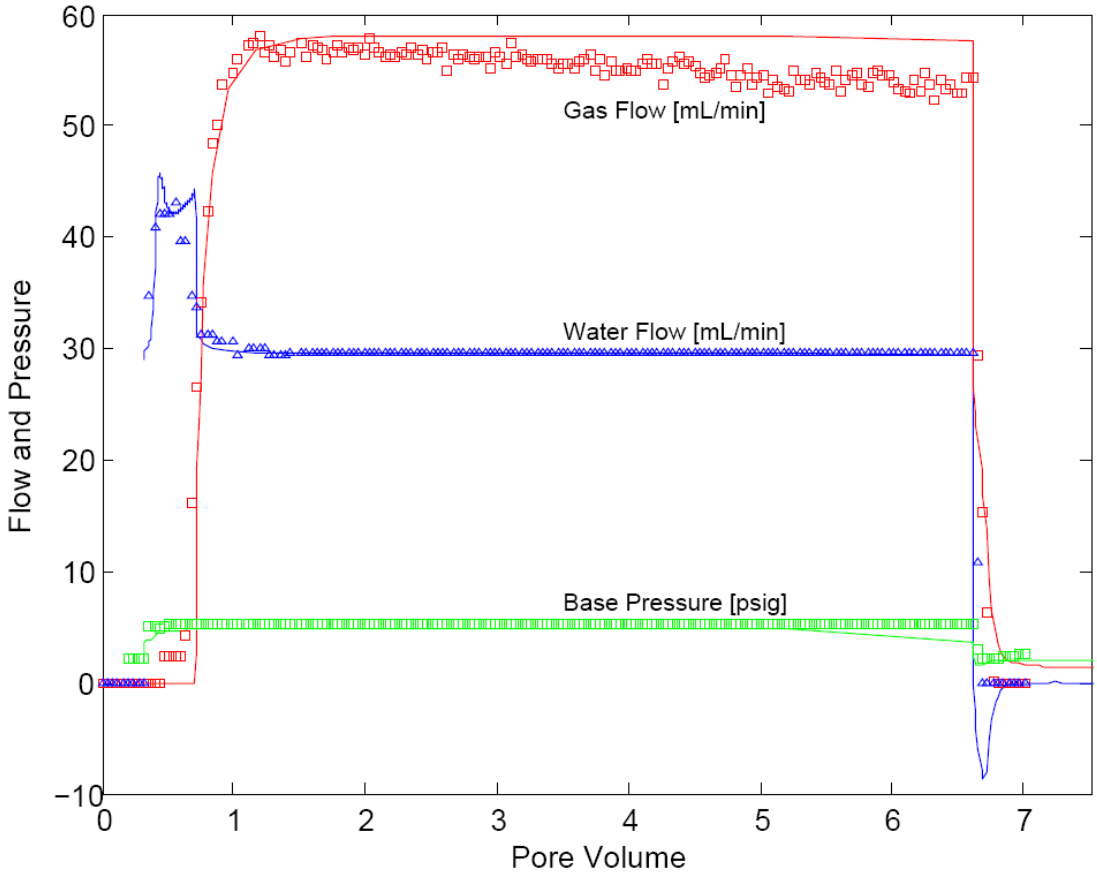

Figure 5. 6 Comparison of operation parameters between experiment and simulation results

Shown in Table 5.5 are the experimental data and simulation results of average gas saturations in the columns during steady state (SS), which form the basis for understanding gas growth, nucleation, and advection mechanisms in the first transient period. Glass bead experiments were more accurately reproduced by simulation than sand pack porous media because the simulation was calibrated by a glass bead system. The main sources for error in this calculation might be tare drift of the balance during experiment and human bias.

Table 5.5 Comparison of gas saturations between experiment and simulation results

Experiment ID	Media	Experimental, Integral, SS-Sg	Simulation, Integral, SS-Sg	Difference
CE1311	Sand	17.32%	16.26%	1.06%
CE1601	Sand	15.16%	14.99%	-0.17%
CE2202	Sand	17.66%	15.36%	2.30%
CE2302	Sand	16.74%	14.43%	2.31%
CE2303	Sand	16.93%	15.16%	1.77%
CE2402	Glass Bead	14.00%	14.63%	-0.63%
CE2403	Glass Bead	14.54%	14.88%	-0.34%
CE2405	Glass Bead	14.82%	14.04%	0.78%

Chapter 6

Conclusions and Recommendations

6.1 Conclusions

- Sand-pack column experiments have demonstrated that otherwise immobile NAPL residuals can be effectively recovered by SWI. For kerosene columns, the residual saturation can be decreased to the order of 4% from an initial value of 16%. The cumulative kerosene recoveries were close to 60% by mobilization only; if volatilization of kerosene was taken into account, the total recoveries exceeded 70%.
- Based on comparison of the experimental results from water-gas co-injection and water flooding, significant NAPL cluster reconnection is reasoned to have happened during SWI and water-gas co-injection, which increased the size of NAPL clusters, decreased the value of critical capillary number and increased the influence of buoyancy on the mobilization of residual NAPL. Under gas-water co-injection conditions, significant mobilization of residual NAPL took place at a very low capillary number, which cannot be understood except in the context of NAPL residual reconnection.
- SWI was more effective at recovering residual NAPL than gas-water co-injection because of gas evolution in-situ, which increases sweep efficiency. Steady gas sparging was completely ineffective at recovering residual NAPL.
- On the basis of the experimental observations, a proposed conceptual model suggests that the reconnection of residual NAPL clusters is due to double drainage displacement during SWI and water-gas co-injection, while during gas de-saturation, the reconnection is a buoyancy-driven, capillarity controlled double imbibition displacement process.

- Kerosene-hexadecane mixture column recovery experiments showed lower NAPL recoveries, leaving higher residual saturations after SWI operations than experiments with pure kerosene. The reason might be the more negative value of spreading coefficient for hexadecane, which suppresses double displacements.
- The recovery and residual saturation were insensitive to changes in grain size in homogeneous sand packs, but were strongly affected by the presence of low permeability layering due to the capillary barrier at the boundary.

6.2 Recommendations

- Two-dimensional experiments are required to study the influence of water flow direction and velocity, and heterogeneity of the porous media on the residual NAPL recovery by mobilization mechanism.
- Pilot field study should be carried out to demonstrate the performance of SWI remediation technology in real contaminated site.
- Micro-model or other visualization experiments should be conducted to confirm the double displacement and the reconnection of residual NAPL clusters during the gas-water co-injection or SWI, and the process of gas de-saturation.
- Some important properties, such as wettability of the porous media, interfacial tensions of the fluids, need to be accurately tested to provide reliable data for simulation, and theoretic displacement mechanism study.
- 2D and 3D simulation methods should be developed to provide a tool for the design and prediction of SWI remediation technology in the future commercialization.

References

Aelion, C.M., Kirtland, B., 2000. Physical versus biological hydrocarbon removal during air sparging and soil vapor extraction. Environ. Sci. Technol., 34 3167-3173.

Adams, J.A., Reddy, K.R., 2000. Removal of dissolved- and free-phase benzene pools from ground water using in situ air sparging. J. Environ. Eng., August 697-707.

Adamski, M., Kremesec, V., Kolhatkar, R., Pearson, C., and Rowan, B., 2005. LNAPL in fine-grained soils: conceptualization of saturation, distribution, recovery, and their modeling. Ground Water Monit. Rem, 25 100–112.

Adamson, A.W., 1997. Physical chemistry of surface. Sixth edition, John Wiley & Sons, Inc.

Ahlfeld, D.P., Dahmani, A., Ji, W., 1994. A conceptual model of field behavior of air sparging and its implication. Ground Water Monit. Rem, Fall 132-139.

Al-Raoush, R.I., 2009. Impact of Wettability on Pore-Scale Characteristics of Residual Nonaqueous Phase Liquids. Environ. Sci. Technol., 43, 4796–4801.

Amili P., and Yotsos, Y.C., 2006. Darcian dynamics: A new approach to the mobilization of a trapped phase in porous media. Transp. Porous Media, 64 25–49.

Balcke, G. U., Paschke, H., Vogt, C., Schirmer, M. 2009. Pulsed gas injection: A minimum effort approach for enhanced natural attenuation of chlorobenzene in contaminated groundwater. Environmental Pollution, 157 2011–2018.

Bass, D.H., Hastings, N.A., Brown R.A., 2000. Performance of Air sparging systems: a review of case studies. J. Hazard. Mater., 72 101–119.

Blunt, M., and King, M.J., 1992. Simulation and theory of two-phase flow in porous media. Phys. Rev. Part A, 46 7680-7699.

Blunt, M., Zhou, D., and Fenwick, D., 1995. Three-phase flow and gravity drainage in porous media. Transp. Porous Media, 20 77-103.

Brooks, M.C., Wise, W.R., and Annable, M.D., 1999. Fundamental changes in in-situ air sparging flow patterns. Ground Water Monit. Rem, Spring 105-113.

Chao, K. P., Ong, S.K., and Huang, M.C., 2008. Mass transfer of VOCs in laboratory-scale air sparging tank. J. Hazard. Mater., 152 1098–1107.

Chatzis, I., Morrow, N.R., and Lim, H.T., 1983. Magnitude and detailed structure of residual oil saturation. SPEJ Soc. Pet. Eng. J. 23 311–326.

Chevalier, L.R., and Fonte, J.M., 2000. Correlation model to predict residual immiscible organic contaminants in sandy soils. J. Hazard. Mater., B72 39–52.

Chevalier, L.R., 2003. Surfactant dissolution and mobilization of LNAPL contaminants in aquifers. Environ. Monit. Assess., 84: 19–33.

Chevalier, L.R., Masten, S.J., Wallace, R.B., and Wiggert. D.C., 1997. Experimental investigation of surfactant-enhanced dissolution of residual NAPL in saturated soil. Ground Water Monit. Rem, 174 89-98.

Childs, J.et al., 2006. Field demonstration of surfactant-enhanced solubilization of DNAPL at Dover Air Force Base, Delaware. J. Contam. Hydrol., 82 1– 22.

Cho, J., Micheal, D., Annable, M.D., 2005. Characterization of pore scale NAPL morphology in homogeneous sands as a function of grain size and NAPL dissolution. Chemosphere, 61 899–908.

Clayton, W.S., 1998. A field and laboratory investigation of air fingers in air sparging. Ground Water Monit. Rem, Summer 134-145.

Dawson, H.E., and Robert, P.V., 1997. Influence of viscous, gravitational, and capillary forces on DNAPL saturation. Ground Water, 35 261-269.

Dernond, A.H., and Roberts, P.V., 1987. An examination of relative permeability relation for two-phase flow in porous media. Water Resource Bulletin, American Water Resource Association, 23 (4) 617-628.

Dong, M., Dullien, F.A.L., and Chatzis, I., 1994. Imbibition of oil in film form over water present in edges of capillaries with an angular cross section. J. Colloid Interface Sci., 172 21-36.

Dong, M., Dullien, F.A.L., and Zhou, J., 1998. Characterization of water flood saturation profile histories by the "complete" capillary number. Transp. Porous Media, 31 213-237.

Doughty, C., 2006. NAPL recovery using CO_2-supersaturated water injection: Distribution of the CO_2 gas phase. M.Sc. thesis, University of Waterloo, On., Canada.

Dror, I., and Berkowitz, B., 2004. Effects of air injection on flow through porous media: Observations and analyses of laboratory-scale processes. Water Resour. Res., 40 W09203.

Dullien, F.A.L. 1992. Porous Media, Fluid Transport and Pore Stricture. Academic Press, Inc.

Dwarakanath, V., Jackson, R., Pope, G., 2002. Influence of wettability on the recovery of NAPLs from alluvium. Environ. Sci. Technol. 36 227-231.

Environment Canada, 1996. http://www.ec.gc.ca/water/en/nature/grdwtr/e_sixmil.htm

Fagerlund, F., Illangasekare, T.H., and Niemi, A., 2007. Non-aqueous-phase liquid infiltration and immobilization in heterogeneous media: 2. Application to Stochastically Heterogeneous Formations. Vadose Zone J., 6 483–495.

Fenwick, D.H. and Blunt, M.J., 1998. Three-dimensional modeling of three phase imbibition and drainage. Adv. Water Res., 21 (2) 121-143.

Gary, G.F, 2008. Essentials of multiphase flow and transport in porous media. Wiley.

Gioia, F., and Urciuolo, M., 2006. Combined effect of Bond and capillary numbers on hydrocarbon mobility in water saturated porous media. J. Hazard. Mater., B133 218–225.

Glassford, G. L., 2001. US Patent No. 6,209,855

Gordon, M. J., 1998. Case history of a large-scale air sparging/soil vapor extraction system for remediation of chlorinated volatile organic compounds in groundwater. Ground Water Monit. Rem., 18 (2) 137–149.

Grattoni, C.A., Jing, X.D., and Dawe, R.A., 2001. Dimensionless groups for three-phase gravity drainage flow in porous media. J. Pet. Sci. Technol., 29 53–65.

Haley, J.L., Hanson, B., Enfield, C., Glass, J., 1991. Evaluating the effectiveness of ground water extraction systems. Ground Water Monit. Rev., 12 119–124.

Harrold, G., Gooddy, D. C., Lerner, D. N., Leharne, S. A.2001. Wettability changes in trichloroethylene-contaminated sandstone. Environ. Sci. Technol. 35 1504–1510.

Held, R.J., Celia, M.A., 2001. Pore-scale modeling and up-scaling of non-aqueous phase liquid mass transfer. Water Resour. Res. 37 (3) 539–549.

Heron, G., Gierk, J. S., Faulkner, B., Mravik, S., Wood, L., and Enfiel, C., 2002. Pulsed air sparging in aquifers contaminated with dense non-aqueous phase liquids. Ground Water Monit. Rem., 22 (4) 73-82.

Heymann, E. and Yoffe, A.1942. The stability of multi-molecular films of hydrocarbon oils, containing spreaders, on water surfaces. Faraday Society, London. Transactions. 38 408-417.

Huling, S.G., and Weaver, J.W., 1991. Dense non-aqueous phase liquid. EPA/540/4-91-002.

Jackson, M.D., Valvatne, P.H., and Blunt, M.J., 2003. Prediction of wettability variation and its impact on flow using pore- to reservoir-scale simulations. J. Pet. Sci. Technol., 39 231–246.

Jang, W., and Aral, M.M., 2009. Multiphase Flow fields in in-situ air sparging and its effect on remediation. Transp. Porous Media, 76 99–119.

Jeong, S.W., and Corapcioglu, M.Y., 2005. Force analysis and visualization of NAPL removal during surfactant-related floods in a porous medium. J. Hazard. Mater., A126 8–13.

Jerauld, G.R., and Salter, S.J., 1990. The effect of pore-structure on hysteresis in relative permeability and capillary pressure: pore-level modeling. Transp. Porous Media, 5 103-151.

Ji, W., Dahmani, A., Ahlfeld, D.P., Lin, J.D., and Hill III, E., 1993. Laboratory study of air sparging: airflow visualization. Ground Water Monit. Rem., 13 (3) 115–126.

Johnson, P.C., 1998. Assessment of the contributions of volatilization and biodegradation to in situ air sparging performance. Environ. Sci. Technol. 32 (2), 276–281.

Johnson, R.J., Pankow, J.F., 1992. Dissolution of dense chlorinated solvents into groundwater: 2. Source functions for pools of solvents. Environ. Sci. Technol. 26 896–901.

Johnson, R.L., Johnson, P.C., McWhorter, D.B., Hinchee, R.E., and Goodman, I., 1993. An overview of in situ air sparging. Ground Water Monit. Rem., Fall 127-135.

Johnston, C.D., Rayner, J.L., Patterson, B.M., Davis, G.B., 1998. Volatilisation and biodegradation during air sparging of dissolved BTEX-contaminated groundwater. J. Contam. Hydrol. 33 377–404.

Joos, P., and Hunsel, J.V., 1985. Spreading of aqueous surfactant solutions on organic liquids. J. Colloid Interface Sci., 106 (1) 161-167.

Keller, A.A., and Chen, M., 2003. Effect of spreading coefficient on three-phase relative permeability of nonaqueous phase liquids. Water Resour. Res., 39 (10) 1288.

Keller, A.A., Blunt, M.J., and Roberts, P.V., 1997. Micromodel observation of the role of oil layers in three-phase flow. Transp. Porous Media, 26 277–297.

Kent, B., and Mosquera, G.C.B., 2001. Remediation of NAPL contaminated aquifers: Is the cure worth the cost? J. Environ. Sci. Health, A36 (8), 1559–1569.

Kim, H., Annable, M. D., Rao, P.S.C., and Cho, J., 2009. Laboratory evaluation of surfactant-enhanced air sparging for perchloroethene source mass depletion from sand. J. Environ. Sci. Health. Part A, 44 406–413.

Kim, J., and Corapcioglu, M.Y., 2003. Modeling dissolution and volatilization of LNAPL sources migrating on the groundwater table. J. Contam. Hydrol., 65 137– 158.

Konečný F., Boháček, Z., Müller, P., Kovářová, M., Sedláčková, I., 2003. Contamination of soils and groundwater by petroleum hydrocarbons and volatile organic compounds – Case study: Elslav Brno. Bulletin of Geosciences, 78 (3) 225–239.

Lai, K.C.K., Surampalli, R.Y., Tyagi R. D., Lo I.M.C., and Yan, S., 2007. Performance monitoring of remediation technologies for soil and groundwater contamination: review. Practice Periodical of Hazardous, Toxic, and Radioactive Waste Management © ASCE / July 132-157.

Leverett, M.C. 1940. Capillary behavior in porous solids. Tulsa Meeting.

Li, D. 2008. Encyclopedia of micro-fluidics and nano-fluidics. Springer.

Li, T., Ioannidis, M., Chatzis, I., 2005. US Patent No. 7,300,227

Li, T., 2004. Recovery of source non-aqueous phase liquids from ground water using supersaturated water injection. M.A.Sc. Thesis, University of Waterloo, On., Canada.

Li, Y., Abriola, L., Phelan, T.J., Andrewramsburg, C., and Pennell, K., 2007. Experimental and numerical validation of the total trapping number for prediction of DNAPL mobilization. Environ. Sci. Technol. 41, 8135-8141.

Li, Y., Wardlaw, N.C., 1986 a. The influence of wettability and critical pore-throat size ratio on snap-off. J. Colloid Interface Sci. 109 (2), 461–472.

Li, Y., Wardlaw, N.C., 1986 b. Mechanisms of non-wetting phase trapping during imbibition at slow rates. J. Colloid Interface Sci. 109 (2), 473– 486.

Library of Parliament, 2006. Freshwater Management in Canada. PRB 05-54E.

Longino, B.L., and Kueper, B. H., 1999. Nonwetting phase retention and mobilization in rock fractures. Water Resour. Res., 35 (7) 2085-2093.

Mackay, D.M., Cherry, J.A., 1989. Groundwater contamination: pump-and-treat remediation. Environ. Sci. Technol. 23 (6) 630–636.

Mahmud, W.M., and Nguyen, V.H., 2006. Effects of snap-off in imbibition in porous media with different spatial correlations. Transp. Porous Media, 64 279–300.

Mani, V., and Mohanty, K.K., 1997. Effect of the spreading coefficient on three-phase flow in porous media. J. Colloid Interface Sci., 187 45–56.

Marley, M. C., Hazebrouck, D.J., and Walsh, M.T., 1992. The application of in situ air sparging as an innovative soils and groundwater remediation technology. Ground Water Monit. Rem., 12 (2) 137–144.

Mayer, A.S., and Miller, C., 1993. An experimental investigation of pore-scale distributions of nonaqueous phase liquids at residual saturation. Transp. Porous Media, 10 57-80.

Mayer, A.S., Miller, C.T., 1992. The influence of porous medium characteristics and measurement scale on pore-scale distributions of residual nonaqueous-phase liquids. J. Contam. Hydrol. 11 189–213.

McCary, J.E., Falta, R.W., 1996. Definition of the air sparging radius of influence for groundwater remediation. J. Contam. Hydrol., 24 25-52.

Mercer, J.W., and Cohen, R.M., 1990. A review of immiscible fluids in the subsurface: properties, models, characterization and remediation. J. Contam. Hydrol., 6 107-163.

Mogensen, K., Stenby, E.H., Zhou, D., 2001. Studies of water flooding in low-permeable chalk by use of X-ray CT scanning. J. Pet. Sci. Technol., 32 1-10.

Mohamed, A.M.I., El-Menshawy, N., Saif, A.M., 2007. Remediation of saturated soil contaminated with petroleum products using air sparging with thermal enhancement. J. Environ. Manage., 83 339–350.

Morrow, N.R., Chatzis, I., 1982. Measurement and correlation of conditions for entrapment and mobilization of residual oil. United States Department of Energy.

Murray, W.A., Lunardini Jr. R.C., Ullo Jr. F.J., Davidson, M.E., 2000. Site 5 air sparging pilot test, Naval Air Station Cecil Field, Jacksonville, Florida. J. Hazard. Mater., 72 121–145.

Nelson, L.C., 2007. Field Trial of Residual LNAPL recovery using CO_2-supersaturated water injection in the Borden Aquifer. M.Sc. thesis, University of Waterloo, On., Canada.

Newell, C.J, Acree, S. D., Ross, R.R., 1995. Light nonaqueous phase liquids, EPA/540/500.

Ng, K.M., Davis, H.T., and Scriven, L.E., 1978. Visualization of blob mechanics in flow through porous media. Chem. Eng. Sci. 33 1009-1017.

Oliveira, L.I., Demond, A.H., 2003. Estimation of primary drainage three-phase relative permeability for organic liquid transport in the vadose zone. J. Contam. Hydrol., 66 261– 285.

Øren, P.E., and Pinczewski, W.V., 1995. Fluid distribution and pore-scale displacement mechanisms in drainage dominated three-phase flow. Transp. Porous Media, 20 105-133.

Palomino, A.M., and Grubb, D.G., 2004. Recovery of dodecane, octane and toluene spills in sand packs using ethanol. J. Hazard. Mater., 110 39–51.

Pennell, K. D.; Pope, G. A., Abriola, L. M., 1996. Influence of viscous and buoyancy forces on the mobilization of residual tetrachloroethylene during surfactant flushing. Environ. Sci. Technol., 30, 1328–1335.

Piri, M. and Karpyn, Z.T., 2007. Prediction of fluid occupancy in fractures using network modeling and x-ray microtomography. II: Results. Phys. Rev. E, 76 016316.

Reddi, L.N., Menon, S., Pant, A., 1998. Pore-scale investigations on vibratory mobilization of LNAPL ganglia. J. Hazard. Mater., 62 211–230

Reeves, P.C., Celia, M.A., 1996. A functional relationship between capillary pressure, saturation, and interfacial area as revealed by a pore-scale model. Water Resour. Res. 32 (8) 2345– 2358.

Sahloul, N.A., Ioannidis, M. A., Chatzis, I., 2002. Schematic description of residual NAPL distribution in (a) a water-wet porous medium and (b) a NAPL-wet porous medium. Adv. Water Res., 25 33–49.

Semer, R., Reddy, K.R., 1998. Mechanisms controlling toluene removal from saturated soils during in situ air sparging. J. Hazard. Mater., 57 209-230.

Soga, K., Pag, J.W.E., Illangasekare, T.H., 2004. A review of NAPL source zone remediation efficiency and the mass flux approach. J. Hazard. Mater., 110 13–27.

Suchumel, E.J., and Pennell, K.D., 2006. Reductions in contaminant mass discharge following partial mass removal from DNAPL source zones. Environ. Sci. Technol., 40 6110-6116.

Suicmez, V.S., Piri M., and Blunt, M.J., 2008. Effects of wettability and pore-level displacement on hydrocarbon trapping. Adv. Water Res., 31 503–512.

Suicmez, V.S., Piri M., Blunt, M.J., 2006. Pore scale modeling of three-phase WAG injection: Prediction of relative permeabilities and trapping for different displacement cycles. SPE 95594.

Suthan, Ed., Suthersan, S., 1999. Remediation engineering: design concepts. Boca Raton: CRC Press.

Taylor, T.P., Rathfelder, K.M., Pennell, K.D., and Abriola, L.M., 2004. Effects of ethanol addition on micellar solubilization and plume migration during surfactant enhanced recovery of tetrachloroethene. J. Contam. Hydrol. 69 73–99.

Valkenburg, M.E.V., Annableb, M.D., 2002. Mobilization and entry of DNAPL pools into finer sand media by cosolvents: two-dimensional chamber studies. J. Contam. Hydrol., 59 211– 230.

Vedvik, A., Wagner, G., Oxaal, U., Feder, J., Meakin, P., and Jøssang, T., 1998. Fragmentation transition for invasion percolation in hydraulic gradients. Phys. Rev. Lett., 80 3065-3068.

Vizika, O., Rosenberg, E., Kalaydjian, F., 1998. Study of wettability and spreading impact in three-phase gas injection by cryo-scanning electron microscopy. J. Pet. Sci. Technol., 20 189–202.

Waduge, W.A.P., Soga, K., Kawabata, J., 2004. Effect of NAPL entrapment conditions on air sparging remediation efficiency. J. Hazard. Mater., 110 173–183.

Wardlaw N.C., Yu, L., 1988. Fluid topology, pore size and aspect ratio during imbibition. Transp. Porous Media, 3 17-34.

Wardlaw, N.C., and McKellar, M., 1985. Oil blob populations and mobilization of trapped oil in unconsolidated. Can. J. Chem. Eng., 63 525-531.

Yang, X., Beckmann, D., Fiorena, S., and Niedermeier, C., 2005. Field study of pulsed air sparging for remediation of petroleum hydrocarbon contaminated soil and groundwater. Environ. Sci. Technol. 39 7279-7286.

Zhao W., 2006. Mass transfer to/from distributed sinks/sources in porous media. PhD thesis, University of Waterloo, On., Canada.

Zhou, D., and Stenby, E., 1991. Displacement of trapped oil from water-wet reservoir rock. Transp. Porous Media, 11 1-16.

Zhou, D., and Blunt, M. 1996. Effect of spreading coefficient on distribution of light non-aqueous phase liquid in subsurface. J. Contam. Hydrol., 25 1-19.